



**ScuDo**  
Scuola di Dottorato – Doctoral School  
WHAT YOU ARE. TAKES YOU FAR



ISTITUTO ITALIANO  
DI TECNOLOGIA  
CENTER FOR SUSTAINABLE  
FUTURE TECHNOLOGIES

Doctoral Dissertation  
Doctoral Program in Physics (32<sup>th</sup> Cycle)

# Physical properties of metal-oxide surfaces for CO<sub>2</sub> valorisation

**Umberto Savino**  
\*\*\*\*\*

## Supervisors

Prof. Elena Maria Tresso, Supervisor

----

Prof. Candido Fabrizio Pirri, IIT-Local Supervisor (P.I.)

Dr. Francesca Maria Toma, LBNL-Local Supervisor

Dr. Angelica Chiodoni, IIT-Local Supervisor

## Doctoral Examination Committee:

Prof. Ettore Vittone , Referee, Università degli Studi di Torino

Dr. Denis Perrone , Referee, Istituto Italiano di Tecnologia

Politecnico di Torino  
October 31, 2019

This thesis is licensed under a Creative Commons License, Attribution - Noncommercial - NoDerivative Works 4.0 International: see [www.creativecommons.org](http://www.creativecommons.org). The text may be reproduced for non-commercial purposes, provided that credit is given to the original author.

I hereby declare that, the contents and organisation of this dissertation constitute my own original work and does not compromise in any way the rights of third parties, including those relating to the security of personal data.

A handwritten signature in blue ink, reading "Umberto Savino", is positioned above a horizontal dotted line.

Umberto Savino  
Turin, October 31, 2019

# Summary

The PhD work here presented is focused on the characterization of the physical surface properties of defective and doped metal oxides for CO<sub>2</sub> valorisation.

Titanium dioxide (TiO<sub>2</sub>) and tin dioxide (SnO<sub>2</sub>) have been selected for this study because they are cheap, easily scalable by following sustainable synthetic pathways, and environmental friendly.

The dissertation focuses in achieving four main goals:

- the study of the physical properties of both the surface and bulk of the selected semiconductor materials;
- the modification of the optical properties of these wide-band gap semiconductors through the introduction of surface defects (such as oxygen vacancies and surface hydroxyl groups);
- the valorisation of CO<sub>2</sub> through its reduction to added-value chemicals (such as CO, CH<sub>4</sub> and HCOOH), in agreement with the hosting research-centre scientific line (IIT-CSFT@PoliTO – Advanced Materials scientific line);
- the study and modelling of the semiconductor/electrolyte interface by using two approaches: 1) the reconstruction of the equivalent circuit model based on the analysis of the impedance measurements; 2) the representation of the band structure of the previously cited interface by following the Schottky junction model.

In line with the presented objectives, different techniques have been adopted to characterize these metal-oxide materials.

The morphology have been investigated by using electron microscopy techniques (FESEM and TEM), followed by X-ray diffraction measurements (XRD and EDX), in order to obtain a complete identikit of the analysed materials.

As previously mentioned, in agreement with the IIT scientific research line, the electrochemical tests have been carried on to evaluate the efficiency of the samples for CO<sub>2</sub> valorisation.

XPS, EPR and impedance spectroscopies have been employed to give a comprehensive interpretation of the CO<sub>2</sub> valorisation results. The evaluation of the flat band potential of the sample/electrolyte interface, together with an in deep analysis of the charge transfer kinetics (occurring in the bulk as well as on the surface) allowed to describe the physical surface properties affecting the catalytic properties of the investigated materials. This approach gave the fundamental knowledge to properly engineer semiconductor metal-oxides to achieve a target tuning of the surface properties.

With a major detail, the research-work on SnO<sub>2</sub> has been based on the analysis of the doping effect. Titanium and iron have been chosen as dopants, looking at density functional theory (DFT) results for CO<sub>2</sub> valorisation presented in literature. The Schottky junction model and the impedance measurements helped the results interpretation, demonstrating that through Fe (III) doping it is possible to enhance both the conductivity, as well as the charge transfer kinetics of SnO<sub>2</sub> for CO<sub>2</sub> valorisation.

Concerning titanium dioxide, the material was modified via hydrogen peroxide surface treatment. The synthesis of the semiconductor itself has been optimized and merged to the hydrogen peroxide treatment aiming to obtain a super-oxidized material (with a band gap reduction from 3.2 eV to 2.5 eV) through a one-step sustainable process. The effect of super-oxidized surface states has been studied with EPR and XPS spectroscopies – in collaboration with the Lawrence Berkeley National Lab –, and resulted in the modification of the valence band density of state, as observed in the HR-XPS of O 2p peak. As said before, the metal-oxide/electrolyte interface was investigated through impedentiometric measurements, using the equivalent circuit and Schottky junction models.



# Acknowledgment

I am facing this section at the end of the whole dissertation as a final step right before closing my work. I wish a “thank you all” would be fine to express my gratitude to all the people I worked with, but they deserve more. At first, I want to thank my beloved wife Sara, for her unshakeable trust on me, my newborn son Leonardo, I hope this work would help science in doing a small step forward to the realization of a brighter future for him. A special thank to my parents, Enrico and Nadia, for carrying me till the beginning of this beautiful adventure, for the support and the trust. At this point, let me change for a while the focus, I will come back later on my fantastic friends.

I sincerely thank prof.ssa Elena Tresso for supervising me and my work from the very first day till the end with patience and determination, to prof. Fabrizio Pirri and IIT foundation for hosting me during this PhD, giving the resources and the knowledge to face this research. A great thank also to dr. Angelica Chiodoni for closely following my work in IIT and to dr. Francesca Toma for hosting me in Berkeley, at the LBNL, allowing me to realize my dream: facing the mysteries of artificial photosynthesis with the JCAP project team.

Hoping not to forget anyone, I want to thank the whole IIT group, from the one who started this adventure with me: Denis, Adriano, Juqin, Kasia, Alberto, Luisa, Trevi, Cat, Miki, Peppe, Simone, Beatrice, Valeria, mastro Giulio, Marco, Valentina, Giulia, Alen, Paolo, Alessandro, Erik, Marzia, Nicolò, Micaela, Annalisa, Ignazio, Nadia, Max, Marco, Sergio, GPS, Lidia, Sara and Annarita. But also the one I found along the way, on top of them Stefania and my PhD-friend Francesca, together with: Amin, Alessandro, Elisa, Giulia, Mirtha, Pravin, Daniele, Luca, Giulia, Eve, Pascal, Cristina, Beatrice, Mara and Ivan. I want to thank here the LBNL colleague too, for their precious friendship and the knowledge they passed me: Guiji, Michelle, Aya, Johanna, Guonsong, David, Erin, Gideon, Elizabeth, Chansol, Ruchira, Jinkiu, Kevin and Rey. A special thank

to Matteo who started and finished the PhD with me, sharing the same supervisor and the same bureaucratic issues.

Thanks to all of them for supporting me in my research, for sharing their knowledge and for helping me in the experiments.

But then back to my friends and parents: my brother Andrea, messer Federico and my wife's parents and relatives: Beatrice, Vincenzo, Stefania, Giulia, Salvatore and Marlene. And all the friends who helped me with their smiles and a good pint of beer. They know quite well what means this work to me, the effort and joy it gave and still gives.

The good of this work comes from the cited people, from the beautiful discussions I had with them and from the relaxing pauses between two experiments. They increased my love in science and guided my attention on the final goal of every art and philosophy: people.



## *To my son Leonardo*

*The only battle I lost was the one I did not fight.  
(E. Che Guevara)*

*Rule n. 6: Do not take yourself that terribly  
serious.*

# Contents

1. Introduction.....	1
1.1 General Introduction.....	1
1.2 Aim of the thesis.....	9
2. Characterization methods .....	11
2.1 Microscopy and morphological characterization .....	11
2.1.1 Field emission scanning electron microscopy .....	11
2.1.2 Transmission electron microscopy .....	12
2.2 Structure and optical properties.....	12
2.2.1 X-ray diffraction .....	12
2.2.2 UV-visible spectroscopy.....	13
2.3 Surface properties.....	14
2.3.1 Electron paramagnetic resonance spectroscopy.....	14
2.3.2 X-ray photoelectron spectroscopy .....	15
2.4 Catalysis.....	16
2.4.1 CO <sub>2</sub> valorisation tests.....	16
2.5 Electronic and electrical properties .....	20
2.5.1 Mott-Schottky technique.....	20
2.5.2 Electrochemical impedance spectroscopy .....	22
3. Tin oxide (SnO <sub>2</sub> ).....	25
3.1 Introduction .....	25
3.1.1 State of the art.....	25
3.1.2 Synthetic approaches .....	26
3.2 SnO <sub>2</sub> synthesis and doping.....	27

3.2.1	Material synthesis .....	27
3.2.2	Electrode preparation .....	27
3.3	Morphology, structure and surface chemistry characterizations .....	28
3.4	CO <sub>2</sub> valorisation and stability tests.....	33
3.4.1	CO <sub>2</sub> valorisation tests.....	34
3.4.2	Stability tests .....	36
3.5	Charge carriers kinetics .....	38
3.6	Band model reconstruction and interpretation.....	42
3.6.1	Band gap calculation.....	43
3.6.2	Valence band top definition .....	44
3.6.3	Semiconductor/electrolyte built-in potential.....	44
4.	Self-doped titanium dioxide.....	46
4.1	Introduction .....	46
4.2	Material synthesis .....	49
4.3	Morphological characterization.....	50
4.4	Structure and surface chemistry .....	52
4.5	CO <sub>2</sub> valorisation tests.....	59
4.6	Charge carriers kinetics .....	62
4.7	Band model and interpretation .....	66
4.7.1	Band gap calculation.....	67
4.7.2	Valence band shape characterization .....	67
4.7.3	Built in potential evaluation.....	68
5.	Conclusions.....	70
5.1	Tin Oxide .....	70
5.2	Self-doped titanium dioxide.....	71
5.3	Future perspectives .....	71
6.	References.....	73
7.	Appendix A.....	81
Nyquist plots fitting .....		81



# List of Tables

Table 1. Area ratio among peak doublets generated by the spin-orbit interaction. ....	16
Table 2. Photo-electrochemical results of CO <sub>2</sub> valorisation tests on Ar-TiO <sub>2</sub> and a-TiO <sub>2</sub> .....	61

# List of Figures

Figure 1. The seventeen goals established by the United Nations (General Assembly resolution A/RES/70/1 of 25 September 2015). .....	2
Figure 2. Representation of the Blue Economy principle. The wastes of manufacturing can be turned into raw materials for other applications. E.g., the waste of vegetable farms can feed animals, whose excrements can be turned into bio-fuels. Then, the bio-fuel can be used in the tractors for vegetable plantation, thus closing the cycle. ....	3
Figure 3. Oxygen Evolving Complex. Water ( $H_2O$ , here in red) oxidation is mediated by four Mg-based and one Ca-based molecules in a five stages (represented by S#) reaction activated by photons ( $h\nu$ ). ....	4
Figure 4. Z-scheme (read the image from left to right). The electrons (at the bottom-left, blue squared), coming from the Oxygen Evolving Complex, are transported from the Photosystems II to the Photosystem I through the Electron transport chain. The final product is NADPH, then consumed in the Calvin cycle. ....	5
Figure 5. Calvin cycle. Carbon dioxide (labeled in red) and NADPH (labeled in blue), produced in the Z-scheme, enter the Calvin cycle. Adenosine tri-phosphate (ATP, in green) is consumed and adenosine di-phosphate (ADP, in cyan) is released. The final balance of the multistep reaction here summarized leads to the production of glucose. ....	6
Figure 6. Schematic of the band alignment inside a reactor. The anode and the cathode are here defined as n and p-type semiconductors, respectively. The alignment with the reduction and oxidation potentials of the solution leads to the formation of a built-in potential, as a consequence, the band bending improves charge separation and allows the charge transfer to the solution. The electrodes (cathode and anode) are electrically connected by the electrolyte; the charge transfer among them occurs through ion diffusion. When needed, the membrane is	

placed inside the electrolyte, separating the anode from the cathode, thus driving selectively the ion-diffusion process.....	7
Figure 7. The XRD setup configurations used for the characterization are the Bragg-Brentano (on the left), in which the detector is moving together with the X-ray gun, and the grazing incident one (on the right), in which the X-ray gun is fixed at a low angle to sample only the surface of the material.....	13
Figure 8. Zeeman effect. When a magnetic field B is applied, its interaction with magnetic number of the electron results in the splitting of the states. The difference in energy between them is defined by $\Delta E$ and a transition among the states may occur.....	15
Figure 9. Sample-spectrometer band alignment. The binding energy of the extracted electron (BE) is expressed as function of the incident X-ray energy ( $h\nu$ ), the kinetic energy (KE) of the electron entering the spectrometer and the work function of the spectrometer itself ( $\Phi_{\text{spectrometer}}$ ). The relation is valid only if the Fermi level of the sample is aligned with the one of spectrometer, e.g. for metals. ....	16
Figure 10. Schematic of a PEC cell (on the left) and an EC cell (on the right). The peculiarity of the PEC cell is that the working electrode (W.E., the cathode in our setup) does not face the counter electrode (C.E., the anode in our setup) in order to allow a direct illumination of the sample. ....	17
Figure 11. The material/electrolyte system can be divided into three main parts. The material itself is a metal oxide whose capacity is described by $C_{\text{mat}}$ ; the layer of oriented charge located inside the electrolyte, in contact with the material, is called Helmholtz layer (H.L.) and represent one of the two plates of the condenser labeled $C_{\text{H.L.}}$ . Lastly, the ion-diffusion that occurs inside the electrolyte is described by the capacitor $C_{\text{dif}}$ . ....	21
Figure 12. Semiconductor/electrolyte interface for p (left) and n-type (right) semiconductors. ....	21
Figure 13. Three-dimensional plot, simulated with ZSimpWin software, showing the real and imaginary part of the impedance as a function of the frequency (red dots). It represents the response of a sinusoidal signal of the circuit (inset on the right). The projection of $\text{Re}Z$ respect to $-\text{Im}Z$ (black curve) is called Nyquist plot.....	23
Figure 14. FESEM imaging of (a-d) $\text{SnO}_2$ , (b-e) $\text{Fe-SnO}_2$ and (c-f) $\text{Ti-SnO}_2$ samples.....	28
Figure 15. XRD patterns of $\text{SnO}_2$ samples compared with $\text{SnO}_2$ reference oxide (JCPDS 00-040-1445). The peaks labeled with the star (*) have been chosen to calculate the crystals mean dimension.....	29

Figure 16. XPS survey spectra of SnO <sub>2</sub> samples. The labels indicate the elements and the orbitals related to the most intense peaks. While Fe 2p and Ti 2p are present only in doped-SnO <sub>2</sub> , Sn 3p, Sn 3d, O 1s and C 1s have been found in all the samples.....	30
Figure 17. HR-XPS of SnO <sub>2</sub> related to (a) O 1s and (b) Sn 3d peak components.....	31
Figure 18. HR-XPS of doped-SnO <sub>2</sub> O 1s components of (a) Fe-SnO <sub>2</sub> and (b)Ti-SnO <sub>2</sub> . .....	31
Figure 19. HR-XPS of doped-SnO <sub>2</sub> Sn 3d components of (a) Fe-SnO <sub>2</sub> and (b) Ti-SnO <sub>2</sub> . .....	32
Figure 20. HR-XPS of doped-SnO <sub>2</sub> components related to (a) Fe2p and (b) Ti2p orbitals.....	32
Figure 21. Bar chart showing the Faradaic efficiencies of SnO <sub>2</sub> at different applied potentials. In red, the current density recorded. ....	34
Figure 22. Bar chart showing the Faradaic efficiencies of Fe-SnO <sub>2</sub> at different applied potentials. In red, the current density recorded. ....	35
Figure 23. Bar chart showing the Faradaic efficiencies of Ti-SnO <sub>2</sub> at different applied potentials. In red, the current density recorded. ....	35
Figure 24. Stability tests carried on for four run in order to record the changes occurring over time in selectivity (Faradaic efficiency) and current density. The samples are labeled as (a) SnO <sub>2</sub> , (b) Fe-SnO <sub>2</sub> and (c) Ti-SnO <sub>2</sub> . .....	36
Figure 25. FESEM imaging of (a) SnO <sub>2</sub> , (b) Fe-SnO <sub>2</sub> and (c) Ti-SnO <sub>2</sub> electrodes after the electrochemical tests.....	37
Figure 26. XRD patterns of SnO <sub>2</sub> samples after the electrochemical tests. The label Cu indicates the peaks related to copper nanoparticles coming from the conductive tape. The peaks labeled with the star (*) have been chosen to calculate the crystals mean dimension. ....	37
Figure 27. Equivalent circuit chosen to simulate the impedance measurements carried on SnO <sub>2</sub> samples. ....	38
Figure 28. Series resistance (R <sub>s</sub> ) plotted as function of the applied voltage...39	39
Figure 29. Transport resistance (R <sub>tr</sub> ) plotted as function of the applied voltage. ....	39
Figure 30. Quasi-capacity of the catalyst (Q <sub>cat</sub> ) plotted as function of the applied voltage. ....	40
Figure 31. Catalyst resistance (R <sub>ct</sub> ) plotted as function of the applied voltage. ....	40
Figure 32. Quasi-capacity of the double layer (Q <sub>dl</sub> ) plotted as function of the applied voltage.....	41

Figure 33. Transfer time (t) plotted as function of the applied voltage. ....	41
Figure 34. Mott-Schottky plots related to SnO <sub>2</sub> samples. The fitting range is underlined with the continuous line. ....	42
Figure 35. (a) Diffuse reflectance spectra of SnO <sub>2</sub> samples and (b) the function derived from the modified Kubelka-Munk relation. ....	43
Figure 36. HR-XPS spectra of O 2p orbitals representative of the valence band of SnO <sub>2</sub> samples. ....	44
Figure 37. Band scheme of SnO <sub>2</sub> samples showing the semiconductor/electrolyte interface in equilibrium condition ( $E_F = E_{RedOx}$ ). In orange the built-in potential values. ....	45
Figure 38. Schematic of the thermal oxidation of Ti foils (on the left) in hydrogen peroxide and their subsequent treatments. ....	49
Figure 39. FESEM imaging summarizing the results of the synthesis optimization. The synthesis parameters here adopted are (a) 65 °C for 48 h, (b) 50 °C for 48 h, (c) 80 °C for 72 h and (d) 80 °C for 48 h. ....	50
Figure 40. FESEM imaging of the top surface of (a) sd-TiO <sub>2</sub> , (c) Ar-TiO <sub>2</sub> , (d) a-TiO <sub>2</sub> and (b) cross-section of Ar-TiO <sub>2</sub> . ....	51
Figure 41. (a, b) TEM imaging of sd-TiO <sub>2</sub> , with FFT in the inset, (c, d) STEM and TEM imaging of Ar-TiO <sub>2</sub> , (e) TEM imaging of Ar-TiO <sub>2</sub> with FFT (bottom-right) and inverse FFT (top-right) associated to the white-squared region. ....	54
Figure 42. GI-XRD carried on (a) sd-TiO <sub>2</sub> , (b) Ar-TiO <sub>2</sub> and (c) a-TiO <sub>2</sub> . ....	55
Figure 43. XPS survey spectra of (a) self-doped TiO <sub>2</sub> samples and (b) pristine Ti foil. The peaks are labeled with the corresponding orbital name. ....	56
Figure 44. HR-XPS of (a) O 1s and (b) Ti 2p peaks of sd-TiO <sub>2</sub> . ....	56
Figure 45. EPR spectrum of sd-TiO <sub>2</sub> . ....	57
Figure 46. HR-XPS of (a) O 1s and (b) Ti 2p peaks of Ar-TiO <sub>2</sub> . ....	58
Figure 47. HR-XPS of (a) O 1s and (b) Ti 2p peaks of a-TiO <sub>2</sub> . ....	58
Figure 48. EPR spectrum of a-TiO <sub>2</sub> . ....	59
Figure 49. Emission spectrum of the solar-simulator lamp with TiO <sub>2</sub> samples absorption position indicated with colored vertical lines. ....	61
Figure 50. Equivalent circuit chosen to simulate the impedance measurements carried on TiO <sub>2</sub> samples. ....	62
Figure 51. Mott-Schottky plots related to TiO <sub>2</sub> samples. The fitting range is underlined with the continuous line. ....	63
Figure 52. Series resistance ( $R_s$ ) plotted as function of the applied voltage. ...	64
Figure 53. Transport resistance ( $R_{tr}$ ) plotted as function of the applied voltage. ....	64

Figure 54. Quasi-capacity of the catalyst ( $Q_{cat}$ ) plotted as function of the applied voltage.....	65
Figure 55. Catalyst resistance ( $R_{ct}$ ) plotted as function of the applied voltage. ....	65
Figure 56. Quasi-capacity of the double layer ( $Q_{dl}$ ) plotted as function of the applied voltage.....	66
Figure 57. Transfer time ( $t$ ) plotted as function of the applied voltage. ....	66
Figure 58. (a) Diffuse reflectance spectra of $TiO_2$ samples and (b) the function derived from the modified Kubelka-Munk relation.....	67
Figure 59. HR-XPS spectra of O 2p orbitals representative of the valence band of $TiO_2$ samples. The black arrows indicate the VB-top value without tailing, while the orange ones indicate the shift occurred with the band-tailing. The lines represent the curves used for the fitting.....	68
Figure 60. Band scheme of $TiO_2$ samples showing the semiconductor/electrolyte interface in equilibrium condition ( $E_F=E_{RedOx}$ ). In orange the built-in potential values.....	69
Figure 61. $SnO_2$ Nyquist plot datas (dots) with fitting (straight line). The labels are linked to the applied potentials (vs RHE): (a) 0.61 V, (b) 0.41 V, (c) 0.21 V, (d) 0.01 V, (e) -0.19 V, (f) -0.39 V, (g) -0.59 V, (h) -0.79 V, (i) -0.99 V and (l) -1.19 V.....	82
Figure 62. Fe- $SnO_2$ Nyquist plot datas (dots) with fitting (straight line). The labels are linked to the applied potentials (vs RHE): (a) 0.61 V, (b) 0.41 V, (c) 0.21 V, (d) 0.01 V, (e) -0.19 V, (f) -0.39 V, (g) -0.59 V, (h) -0.79 V, (i) -0.99 V and (l) -1.19 V.....	83
Figure 63. Ti- $SnO_2$ Nyquist plot datas (dots) with fitting (straight line). The labels are linked to the applied potentials (vs RHE): (a) 0.61 V, (b) 0.41 V, (c) 0.21 V, (d) 0.01 V, (e) -0.19 V, (f) -0.39 V, (g) -0.59 V, (h) -0.79 V, (i) -0.99 V and (l) -1.19 V.....	84
Figure 64. sd- $TiO_2$ Nyquist plot datas (dots) with fitting (straight line). The labels are linked to the applied potentials (vs RHE): (a) 0.61 V, (b) 0.41 V, (c) 0.21 V, (d) 0.01 V, (e) -0.19 V, (f) -0.39 V and (g) -0.59 V.....	85
Figure 65. Ar- $TiO_2$ Nyquist plot datas (dots) with fitting (straight line). The labels are linked to the applied potentials (vs RHE): (a) 0.61 V, (b) 0.41 V, (c) 0.21 V, (d) 0.01 V, (e) -0.19 V, (f) -0.39 V and (g) -0.59 V.....	86
Figure 66. a- $TiO_2$ Nyquist plot datas (dots) with fitting (straight line). The labels are linked to the applied potentials (vs RHE): (a) 0.61 V, (b) 0.41 V, (c) 0.21 V, (d) 0.01 V, (e) -0.19 V, (f) -0.39 V, (g) -0.59 V, (h) -0.79 V, (i) -0.99 V, (l) -1.19 V. ....	87



# Chapter 1

## Introduction

### 1.1 General Introduction

The 17<sup>th</sup> sustainable development goals (shown in Figure 1), identified by the United Nations (United Nations Headquarters in New York, 25 to 27 September 2015), established a vision of the future that yearn for a radical change of the world by 2030.[1] The vision of our future society lays on five pillars:

- I. the end of poverty and hunger, to establish a social well-fare worldwide in which anyone can fulfil its potential in dignity, equality and in a healthy environment;
- II. the defence of the planet from degradation, achieved through sustainable behaviours in consumption and production of goods as well as of energy, sustainably managing all the natural resources. Moreover, it claims to an urgent action to mitigate climate changes, with the purpose to satisfy the needs of the present and future generations;
- III. the guarantee that economic, social and technological progress will occur in harmony with nature;
- IV. the creation and advancement of peaceful, just and inclusive societies, free from fear and violence, in agreement with the motto: “There can be no sustainable development without peace and no peace without sustainable development”;
- V. the implementation of Global Partnership for Sustainable Development, based on global solidarity, focusing on the needs of the poorest and most vulnerable and with the participation of all countries, all stakeholders and all people.



**SUSTAINABLE DEVELOPMENT GOALS**



**Figure 1. The seventeen goals established by the United Nations (General Assembly resolution A/RES/70/1 of 25 September 2015).**

UN presented a picture of the World with dramatic but clear tones: billions of citizens live in poverty, without a life of dignity. Rising inequalities, enormous disparities of opportunity, wealth and power. Gender inequality, unemployment, global health threats. Intense natural disasters, spiralling conflict, violent extremism, terrorism and related humanitarian crises and forced displacement of people. Moreover, natural resource depletion and adverse impacts of environmental degradation, including desertification, drought, land degradation, freshwater scarcity and loss of biodiversity.

These are some of the challenges that have to be faced to achieve a sustainable development. On top of them, climate change (including the increase in global temperature, sea level rise and ocean acidification) is the one affecting the more the ability of all countries to achieve the goals of sustainable development.

On the other hand, this crisis makes our times also an era of immense opportunity. Significant progress has been made in these years, in particular about the diffusion of information and communications technology and global interconnectedness, which are pushing human progress, as well as scientific and technological innovation in various fields like medicine and energy.

As previously mentioned, Climate Change mitigation is the primary goal to be achieved in the short time with an international choral action. The objective will be reached, according to UN, by reducing global greenhouse gas emissions aiming to keep the global average temperature below 1.5–2 °C above pre industrial levels.

In addition to this, UN found out that social and economic development depends on the sustainable management of our planet's natural resources. Because of this, further efforts have to be devoted to safeguard and sustainably use oceans and seas, freshwater resources, as well as forests, mountains and drylands and to protect biodiversity, ecosystems and wildlife.

The claim for a sustainable development, in a similar vein, here discussed through the words of the UN committee, passes through the current perception of development aiming to change the past paradigm. The golden rule has to be: satisfying the energy demand by using wastes as raw materials, thus softening the anthropic impact on Earth.

Gunter Pauli first comprehensively discussed the bases of the circular economy (Figure 2) in a Report to the Club of Rome at its General Assembly in 2009. In his vision, the wastes of industrial production became raw materials for new processes. *The Blue Economy* is the result of this vision, a book that collects 340 innovations based on nature-inspired technologies that could beneficially affect the economies of the world, while sustainably providing basic human needs – potable water, food, jobs, and habitable shelter.[2]

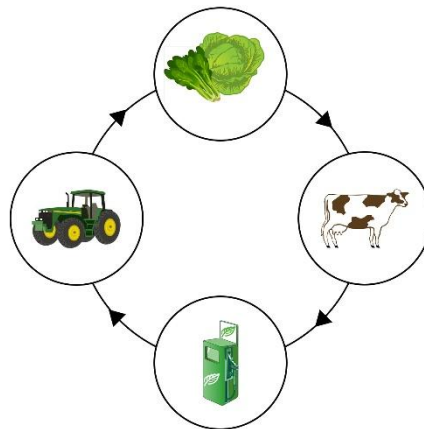


**Figure 2. Representation of the Blue Economy principle. The wastes of manufacturing can be turned into raw materials for other applications. E.g., the waste of vegetable farms can feed animals, whose excrements can be turned into bio-fuels. Then, the bio-fuel can be used in the tractors for vegetable plantation, thus closing the cycle.**

In line with the statement on Pauli's circular economy stands the idea of an Italian photochemist: Giacomo Luigi Ciamician. He first imagined the possibility to convert carbon dioxide (CO<sub>2</sub>) into a solar fuel by taking inspiration from nature. The words he used in 1912 to describe the future of sustainable technologies are the archetype of the so-called Artificial Photosynthesis.[3]

*“Where vegetation is rich, photochemistry may be left to the plants and by rational cultivation, as I have already explained, solar radiation may be used for industrial purposes. In the desert regions, un-adapted to any kind of cultivation, photochemistry will artificially put their solar energy to practical uses. On the arid lands there will spring up industrial colonies without smoke and without smokestacks; forests of glass tubes will extend over the plants and glass buildings will rise everywhere. Inside of these will take place the photochemical processes that hitherto have been the guarded secret of the plants, but that will have been*

*mastered by human industry, which will know how to make them bear even more abundant fruit than nature, for nature is not in a hurry and mankind is. And, if in a distant future the supply of coal becomes completely exhausted, civilization will not be checked by that, for life and civilization will continue as long as the sun shines! If our black and nervous civilization, based on coal, shall be followed by a quieter civilization based on the utilization of solar energy that will not be harmful to progress and to human happiness”.*

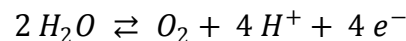
This perspective turns CO<sub>2</sub> from the guilty part of global warming to the solution to energy and resources demand, which is currently overwhelming Earth availability. CO<sub>2</sub> still stands as a proof of human responsibility in global warming, as demonstrated by IPCC reports,[4] but it can also become a free, widespread raw material for solar fuels production, such as methane, methanol or formic acid.[5]

Since UN impose a short-term project and an immediate action to face global warming, scientists started studying and developing new technologies to reduce CO<sub>2</sub>. For this purpose, catalysts have been massively employed. [6]

The common aim is to realize a highly technological leaf, which can run the photosynthetic processes by taking inspiration from nature.

The reactions occurring in the chloroplast, the cell-organ responsible to run the photosynthetic processes, are here briefly described:[7]

- **Water photo-oxidation.**



The presented mechanism occurs in a five steps cycle called oxygen evolving complex (Figure 3). The reaction is mediated by four manganese ions and a calcium ion that mediates the electronic transfer from water catalysing the formation of the O–O bond;

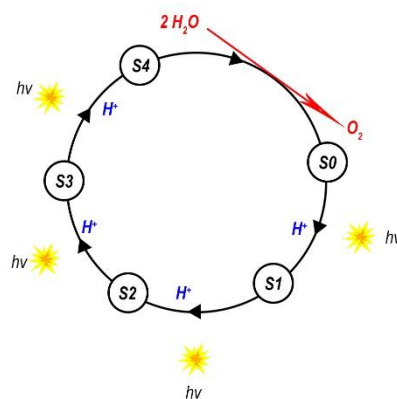


Figure 3. Oxygen Evolving Complex. Water (H<sub>2</sub>O, here in red) oxidation is mediated by four Mg-based and one Ca-based molecules in a five stages (represented by S#) reaction activated by photons (hν).

- **Z scheme.** It involves the RedOx processes occurring through light excitation. In the so-called photosystem I (PSI) the photons around 700 nm are absorbed by chlorophylls and a strong reducing agent is produced to

reduce the molecules of  $\text{NADP}^+$ . At the same time, photons around 680 nm are absorbed in the photosystem II (PSII) and a strong oxidative agent is produced to oxidize water. An electron chain connects PSI and PSII allowing the transfer of the excited electrons. As a result of this,  $\text{NADP}^+$  is reduced to NADPH (Figure 4).

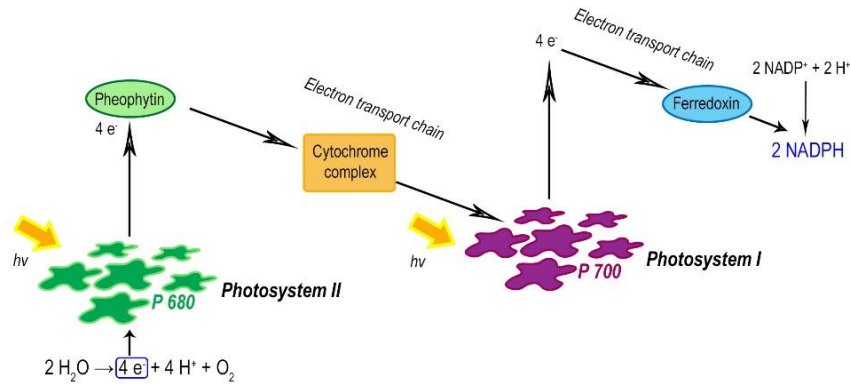
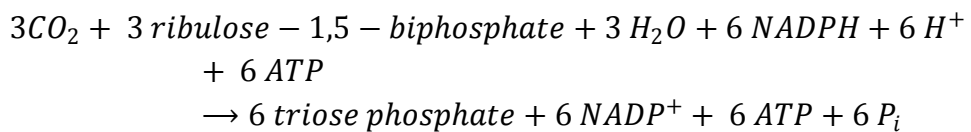
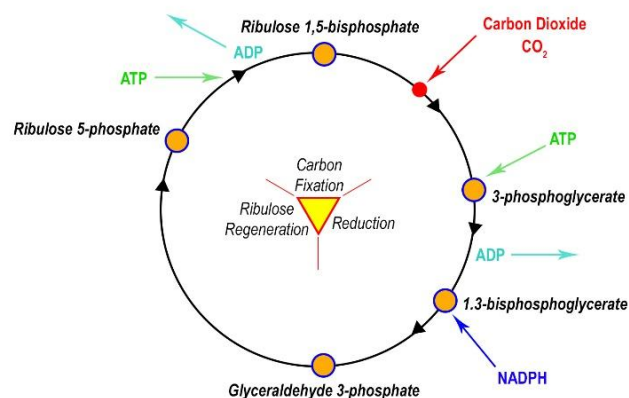


Figure 4. Z-scheme (read the image from left to right).The electrons (at the bottom-left, blue squared), coming from the Oxygen Evolving Complex, are transported from the Photosystems II to the Photosystem I through the Electron transport chain. The final product is NADPH, then consumed in the Calvin cycle.

- **Calvin cycle.** This is the core of the photosynthetic process in which  $\text{CO}_2$  is chemically fixed into a glucose molecule (Figure 5). The process is sketched by the following equation:





**Figure 5. Calvin cycle.** Carbon dioxide (labeled in red) and NADPH (labeled in blue), produced in the Z-scheme, enter the Calvin cycle. Adenosine tri-phosphate (ATP, in green) is consumed and adenosine di-phosphate (ADP, in cyan) is released. The final balance of the multistep reaction here summarized leads to the production of glucose.

The thermodynamic efficiency of Calvin cycle has been estimated to be 90%, while the efficiency of the overall process 33%. The measured efficiencies are around 0.1 – 0.4 % with a maximum of 4% for sugarcane farmed in Texas and Hawaii. The drastic reduction is mainly influenced by: water availability, mineral presence, surrounding temperature and the growth stage of the plant.

The complex multi-step natural mechanism is technologically translated into a device in which catalysts have the role to reduce the activation energy of the chemical processes involved, providing the electrons and protons needed to transform CO<sub>2</sub> into solar fuels.

The device, also called reactor (Figure 6), is a multilayer system made of catalysts and membranes in which CO<sub>2</sub> flows and reacts to be reduced to added value chemicals, such as carbon monoxide (CO), methane (CH<sub>4</sub>), methanol (H<sub>3</sub>COH), formic acid (HCOOH) etc. The technological quests are: selectivity through products, their easy separation and extraction, and, in case of gas products, the pressure control. The latter parameter has to be considered to guarantee CO<sub>2</sub> reduction products injection directly into the pipes of the cities gas lines. Since the target is atmospherical CO<sub>2</sub> reduction (not pressurized), the dissertation will be focused on a reactor working in ambient condition, both for pressure and temperature. The reaction, commonly, is run in a water medium, called electrolyte, which acts as source of protons and closes the electrical contact between cathode and anode, thanks to the presence of a small concentration of carbonate ions.

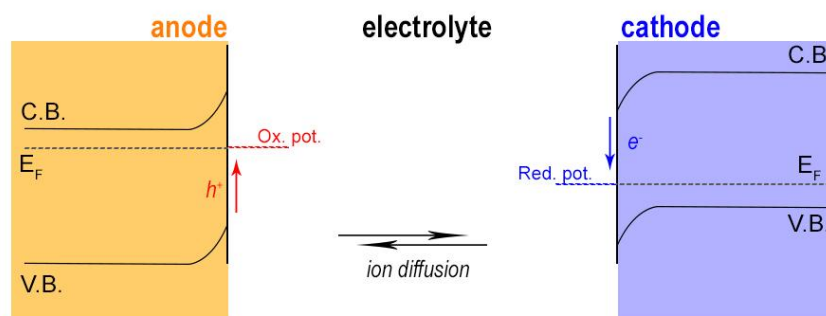


Figure 6. Schematic of the band alignment inside a reactor. The anode and the cathode are here defined as n and p-type semiconductors, respectively. The alignment with the reduction and oxidation potentials of the solution leads to the formation of a built-in potential, as a consequence, the band bending improves charge separation and allows the charge transfer to the solution. The electrodes (cathode and anode) are electrically connected by the electrolyte; the charge transfer among them occurs through ion diffusion. When needed, the membrane is placed inside the electrolyte, separating the anode from the cathode, thus driving selectively the ion-diffusion process.

The main, fundamentals components of the reactor are:

- the **cathode**. A catalyst that adsorbs and reduces  $\text{CO}_2$  using electrons and protons coming from the anode. This mechanism passes through five steps:
  1. the diffusion of  $\text{CO}_2$ , dissolved in the liquid medium, to the surface of the catalyst;
  2. the adsorption on the reaction centres of the catalyst;
  3. the reaction of the adsorbed phase. In case of photo-catalysis, it passes through the absorption of a photon, which is followed by the creation of an electron-hole pair and their migration, the electron to the surface and the hole to the back. Finally, the reduction of the adsorbed compound;
  4. the hole recovery by an electron coming from the anode, and desorption of the product(s) of  $\text{CO}_2$  reduction reaction from the surface of the catalyst;
  5. in the end, the diffusion of the products from the surface to the electrolyte.

In the case of electro-catalysis, a bias forces the electron diffusion from the bulk material to its surface and reduces the  $\text{CO}_2$  activation energy of the reduction reaction by rising the potential of surface electrons above the RedOx potential of the reaction (see Figure 6). The RedOx potential defines the capability of a molecule to accept electrons. In other words, the more positive the RedOx potential, the more readily a molecule is reduced.

- the **membranes** selectively control the ion migration inside the electrolyte. They are responsible of resistive effects related to the charge flow, since are limiting the ion diffusion from the cathode to the anode and vice-versa. The membranes can be also used to separate the products

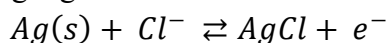
from the reagents at the exit of the reactor. The diffusion law that regulates the ion migration through the membrane is the Fick's law. It describes the transfer of a solute over time between two half-cells of a reactor, separated by a thin membrane:

$$\frac{dq}{dt} = -DA \frac{dc}{dx}$$

where  $q$  is the quantity of solute,  $A$  is membrane surface area,  $c$  is the concentration,  $D$  is the diffusion coefficient,  $dx$  is the membrane thickness, and  $dc/dx$  is concentration gradient.[8]

- the **anode**. A catalyst that produces protons from water oxidation, and electrons which are transferred to the cathode, as previously described.

Another important element, present in the reactor, is the **reference electrode**. It provides a standard for the electrochemical measurements. The three main requirements are reversibility (non-polarizability), reproducibility, and stability. Hydrogen electrodes (also known as Standard Hydrogen Electrode - SHE) were chosen as the primary reference electrode due to their excellent reproducibility. The electrode consisted of a platinum foil with electroplated Pt black to catalyse the hydrogen electron transfer reaction. The standard potential of the hydrogen electrode is conventionally set to zero at all temperatures, thus establishing a hydrogen scale of standard potential. However, this electrode is impractical in routine usages, thus secondary reference electrodes, such as calomel, sulphate, and silver/silver chloride (Ag/AgCl) are used. As a secondary reference electrode, the Ag/AgCl electrode is the most common due to its simplicity, stability, and capability of miniaturization. A conventional Ag/AgCl reference electrode is a silver wire that is coated with a thin layer of silver chloride either by electroplating or by dipping the wire in molten silver chloride. [9] The RedOx reaction occurring at the Ag/AgCl electrode is:



The potential developed is determined by the chloride concentration of the inner solution, by using the Nernst equation:

$$E = E_0 - \frac{RT}{zF} \ln \frac{a_{red}}{a_{ox}}$$

where  $E_0$  is the standard reduction potential of the half-cell under investigation,  $R$  is the universal gas constant,  $T$  is the absolute temperature,  $z$  is the number of electrons exchanged,  $F$  is the Faraday constant and  $a_{red}$  and  $a_{ox}$  are the activity coefficients related to the reduced and oxidized species. They are commonly substituted with the concentrations of RedOx species.

The equation is derived from the standard changes in the Gibbs free energy associated with an electrochemical transformation and it relates the reduction potential of an electrochemical reaction to the standard electrode potential,

temperature, and activities of the chemical species undergoing reduction and oxidation.

Several materials have been employed as catalysts for CO<sub>2</sub> reduction reaction: organometallic complexes, [10,11] carbon based materials, [12–14] noble metals [15] and metal oxides. [16,17] The latter are the most interesting because they are cheap, abundant on Earth, it is possible to synthesize them with green and sustainable processes. Since they exhibit a semiconductive behaviour, their use in photocatalysis is favoured by the possibility of tuning the energy gap through defect engineering, thus moving the absorption to the visible range.

For this reason, we considered a physical approach is needed to deeply understand the behaviour of semiconductor surfaces in catalysis in order to tune their physical and chemical properties.

## 1.2 Aim of the thesis

The present work is focused on the *Physics and technology of nanostructures for solar to fuel conversion*. The activity has been proposed by Department of Physics (DISAT) of the Politecnico of Torino, and is funded by the Italian Institute of Technology - IIT CSFT@PoliTO. An important part of the research has been carried on at the Lawrence Berkeley National Laboratory in California (Joint Center for Artificial Photosynthesis) in collaboration with the Chemical Division.

The PhD program focuses on the physical properties of nanomaterials capable to exploit solar to fuel conversion. In particular the main objectives are the design and the development of nano-architectures for: light absorption, photogenerated charge transfer, photocatalytic activity for both CO<sub>2</sub> reduction and H<sub>2</sub> evolution, CO<sub>2</sub> capture and storage.

For this purpose, two cases of study have been considered: doped tin oxide and self-doped titanium dioxide:

- doped tin oxide. The un-doped material is known in literature to reduce CO<sub>2</sub> to formic acid, however its efficiency and selectivity through products can be enhanced by doping or substitution. A feasibility study have been carried on titanium (IV) substitution and iron (III) doping, grounding the investigation on theoretical calculations presented in literature;[18]
- self-doped titanium dioxide. It raises the possibility to tune the light absorption range by managing surface defects, such as oxygen vacancies, super-oxidized states and hydroxyl groups. The cross-link of bulk and surface properties is particularly interesting both for the physical and chemical aspects. In fact, the self-doping affects both selectivity through CO<sub>2</sub> reduction, and so on catalysis, and light absorption, thus allowing a band gap engineering.

A particular attention is devoted to the synthesis too. It is stressed in order to optimize the time and energy consumption to allow the scale up of the material at the lowest cost. The alternative synthesis of this sustainable

material (cheap and earth abundant) can open the way to future catalysts for photo-driven reactions.

The choice of these catalysts has been staked off looking for sustainable, earth abundant materials. Moreover, the sustainability of synthetic processes has been highlighted, as required by the guidelines of the hosting research centres.

The catalytic properties of these materials are investigated in electrochemical environment rich in CO<sub>2</sub>, employing the reactor model previously described.

The electrolyte/catalyst interface is studied using a Schottky-junction model, in order to gain information on:

- the band alignment, and so on the density of states;
- on the charge transfer kinetics for CO<sub>2</sub> reduction reaction, by analysing the junction using an equivalent circuit model.

For sake of clarity and simplicity, the present dissertation will be divided in two main parts, describing the two presented materials. In each, the morphological and structural characterization will be presented, with a particular attention on the analysis of the surface properties. CO<sub>2</sub> reduction reaction results will be then presented and discussed using the models mentioned above.

# Chapter 2

## Characterization methods

Several techniques have been adopted to gain a comprehensive picture of the physical and chemical properties of the investigated materials. The instruments employed for the characterizations are located in the facilities of PoliTO (Torino), IIT CSFT@PoliTO (Torino), LBNL (Berkeley) and UniTO (Torino).

### 2.1 Microscopy and morphological characterization

#### 2.1.1 Field emission scanning electron microscopy

A field emission scanning electron microscope (FESEM) is constituted by an electron gun in which a field-emission cathode provides narrow probing beams at low as well as high electron energy, resulting in both improved spatial resolution and minimized sample charging and damage.

The ability to examine small-area spots at different electron accelerating voltages allows to gain information both on the morphology of the scanned sample, and on its composition by employing the energy dispersive spectroscopy (EDS). As the electron beam of the FESEM is scanned across the sample surface, it generates X-ray photons from the atoms in its path. The energy of each X-ray photon is characteristic of the element that produced it. The EDS microanalysis system collects the X-rays, sorts and plots them by energy, and automatically identifies and labels the elements responsible for the peaks in this energy distribution. Typically EDS data are compared with standards to produce a full quantitative analysis showing the sample composition. Data output includes plots of the original spectrum, showing the X-ray photon count rate for each energy. Maps of element distributions over areas of interest and quantitative composition tables can also be produced.

FESEM (FEI Quanta FEG250, ZEISS Auriga and ZEISS Supra 40) were used to characterize the material morphology, with a beam accelerating voltage of 5 kV. In this work, the Energy-Dispersive X-ray analysis (EDS or EDX) was

performed to verify the presence of dopants and contaminants by using a beam energy of 20 keV.

### 2.1.2 Transmission electron microscopy

A transmission electron microscope (TEM) produces a high-resolution, grey-scale image from the interaction between the analysed samples and the energetic electrons in a vacuum chamber. The electrons, generated by the gun, pass through multiple electromagnetic lenses. During transmission, the speed of electrons directly correlates to electron wavelength; the faster electrons move, the shorter wavelength and the greater the quality and detail of the image. The lighter areas of the image represent the places where a greater number of electrons were able to pass through the sample, and the darker areas reflect the denser areas of the object. These differences provide information on the structure, texture, shape and size of the sample.

Further information can be extracted from a high resolution TEM image through the Fast Fourier Transformation (FFT), an algorithm for calculation of discrete Fourier transformation (the sum of the intensities up in discrete points). It is the representation of the crystal in the reciprocal space. Thus, it can be used to identify the crystal phase as well as the orientation of the exposed facets.

Scanning transmission electron microscopy (STEM) combines the principles of transmission electron microscopy and scanning electron microscopy and can be performed on either type of instrument. The STEM technique scans a very finely focused beam of electrons across the sample in a raster pattern. Interactions between the beam electrons and sample atoms generate a serial signal stream, which is correlated with beam position to build a virtual image in which the signal level at any location in the sample is represented by the grey level at the corresponding location in the image.

TEM (FEI monochromated F20UT and F20ST Tecnai) was performed to identify the crystalline structure at the nano-scale using 200 kV as accelerating voltage. For TEM measurements, a dispersion of particles was prepared by sonication in methanol. The dispersion was then drop-casted on standard copper grid with ultra-thin carbon layer (C type-A, Ted Pella, Inc).

## 2.2 Structure and optical properties

### 2.2.1 X-ray diffraction

The technique is based on the diffraction process described by Bragg equation:

$$n\lambda = 2d \sin(\theta)$$

In this equation,  $n$  is an integer,  $\lambda$  is the characteristic wavelength of the X-rays impinging on the crystalline sample,  $d$  is the interplanar spacing between rows of atoms, and  $\theta$  is the angle of the X-ray beam with respect to these planes. When this equation is satisfied, X-rays scattered by the atoms in the plane of a

periodic structure are in phase and diffraction occurs in the direction defined by the angle  $\theta$  (Figure 7). X-ray diffraction technique is used for the identification of crystalline phases of various materials and the quantitative phase analysis subsequent to the identification.

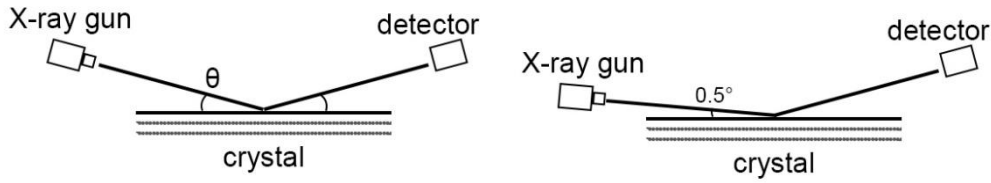


**Figure 7.** The XRD setup configurations used for the characterization are the Bragg-Brentano (on the left), in which the detector is moving together with the X-ray gun, and the grazing incident one (on the right), in which the X-ray gun is fixed at a low angle to sample only the surface of the material.

The crystal dimension is estimated using the Scherrer equation:

$$\tau = \frac{K\lambda}{\beta \cos(\theta)}$$

where  $\tau$  is the mean size of the ordered crystalline domains,  $K$  is a dimensionless number called “shape factor” and depends on the shape of the crystallite,  $\lambda$  is the X-ray wavelength,  $\beta$  is the value of the FWHM of the peak considered for the analysis, and  $\theta$  is the Bragg angle.

XRD (Rigaku-SmartLab and PANalyticalX’Pert Pro) was used to verify the crystallographic phase of the samples using the Cu K $\alpha$  ( $\lambda = 0.15406$  nm) radiation source. The diffraction patterns were collected in Bragg-Brentano and thin-film configuration (also called grazing-incident XRD, GI-XRD), depending on the sample thickness, with a  $2\theta$  range from  $20^\circ$  to  $70^\circ$ .

### 2.2.2 UV-visible spectroscopy

UV-visible spectroscopy studies the interaction of the light with matter by varying the energy of the incident probing photons. The response is collected to gain information on the optical properties (transmission, reflection or absorption), at any wavelength from the near-UV (about 200 nm) to the visible range until the near-IR (about 900 nm).

Since the materials under investigation are highly rough and not transparent, diffuse reflectance spectra have been collected. For this purpose, the UV–visible spectrometer (SolidSpec 3700 SHIMADZU and Lambda 650S PerkinElmer) was equipped with an integrated sphere.

The diffuse reflectance spectroscopy is frequently employed for the determination of the electronic transitions in solid materials, since the optical methods used for measuring forbidden energy band gaps do not depend on temperature variations or uncertainties due to surface states (electrical conductivity, Hall constant and photoconductivity techniques). The optical excitation of the electrons from the valence band (VB) to the conduction band (CB) is evidenced by an increase in the absorbance at a given wavelength (band gap energy). The study of the tail of the absorption curve of semiconductors

shows that it has a simple exponential drop. This drop has been suggested as the most appropriated method to determine the position of the absorption edge.[19,20] The linear section in the diffuse reflectance spectra is taken for measuring the band gap energy ( $E_{\text{gap}}$ ). The given value of  $E_{\text{gap}}$  for a given semiconductor could vary depending on the extrapolation method and optical electronic transition (direct allowed, direct forbidden or indirect allowed, indirect forbidden).

For highly light scattering materials and absorbing particles in a matrix, the Kubelka-Munk relation is applied:

$$F(R) = \frac{(1 - R)^2}{2R}$$

where  $R$  is the diffuse reflectance. This equation links the optical information to the absorption properties of the material since the given  $F(R)$  is proportional to the extinction coefficient.

A modified Kubelka–Munk function can be obtained by multiplying the  $F(R)$  function by  $h\nu$ , using a coefficient ( $n$ ) associated with a corresponding electronic transition:[21]

$$(F(R) \cdot h\nu)^n$$

where  $n$  is equal to  $\frac{1}{2}$  for indirect energy gap and 2 for the direct one.

By plotting this equation (Tauc plot) as a function of the photon energy, the band gap of semiconductor particles can be extrapolated by fitting of the linear part of the curve and looking at the intercept.

## 2.3 Surface properties

### 2.3.1 Electron paramagnetic resonance spectroscopy

Electron paramagnetic resonance (EPR), also known as electron spin resonance, is a spectroscopic technique used to investigate paramagnetic compounds with unpaired electron. EPR measures the energy of spin transitions when unpaired electrons are immersed in a magnetic field. The energy will lead to the characteristic g-factor for the molecule being analysed. Free electrons possess an intrinsic angular momentum called spin that generates a magnetic field through the charge of the electron. From a classical understanding the free electron has a magnetic dipole with a magnetic moment ( $\mu$ ). Without the presence of an external magnetic field, the directions of the magnetic moment are degenerate in energy. The introduction of the magnetic field  $B_0$  breaks the degeneracy of the magnetic moment, which is observed through the Zeeman Effect (Figure 8).

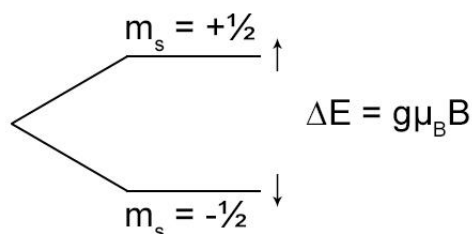


**Figure 8. Zeeman effect. When a magnetic field  $B$  is applied, its interaction with magnetic number of the electron results in the splitting of the states. The difference in energy between them is defined by  $\Delta E$  and a transition among the states may occur.**

EPR spectroscopy at room temperature was used to investigate the oxidation state of the defective surfaces. The EPR spectra were collected using a Bruker ELEXSYS 580 spectrometer equipped with a single microwave cavity. The following spectrometer conditions were used: microwave frequency, 9.228 GHz; field modulation amplitude, 32G at 100 kHz; microwave power, 5 mW.

### 2.3.2 X-ray photoelectron spectroscopy

X-ray photoelectron spectroscopy (XPS) is the technique employed to analyse the surface chemistry of a material. XPS can measure the elemental composition, empirical formula, chemical state and electronic state of the elements within a material. XPS spectra are obtained by irradiating a solid surface with an X-rays beam while simultaneously measuring the kinetic energy and electrons that are emitted from the top 1–10 nm of the material being analysed. A photoelectron spectrum is recorded by counting ejected electrons over a range of electron kinetic energies. Peaks appear in the spectrum from atoms emitting electrons of a particular characteristic energy. The energies and intensities of the photoelectron peaks enable identification and quantification of all surface elements (except hydrogen).

For these reasons, the surface composition of the synthesized materials was determined by X-ray photoelectron spectroscopy (XPS, Kratos Axis Ultra DLD and PHI 5000 VersaProbe) using monochromatic Al-K $\alpha$  (1486.69 eV).

Data manipulation has been run on with the software CasaXPS. In the high resolution spectra (HR-XPS), the backscattering component, which contributes to the background, is treated with the Shirley model and subtracted to the signal. The peaks components are fitted with a Gauss-Lorentz distribution (30% weight) apart for the asymmetric ones, for which literature guidelines have been followed.

Theoretical-based relations have been followed for the fitting, in particular the areal ratio among doublets, formed by spin-orbit interaction (Table 1). In presence of regions with multiple-components (due to the overlap of different coexisting oxidation states), they have been used as constrains for the fitting.



Two different setups have been used to test the photo-electro catalytic properties (in light and dark conditions) and electro catalytic ones (only in dark) (Figure 10).

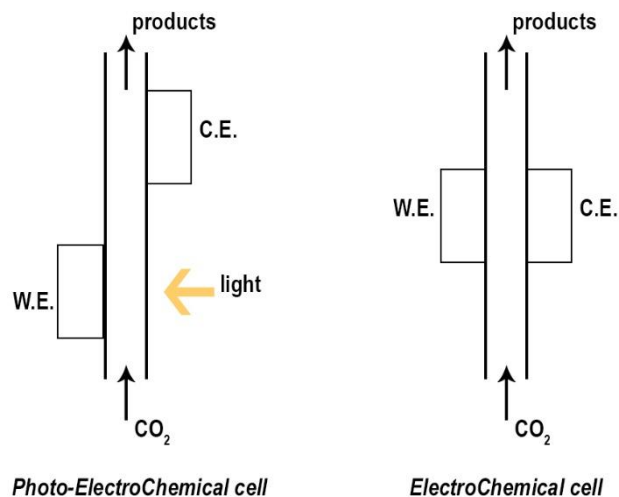


**Figure 10.** Schematic of a PEC cell (on the left) and an EC cell (on the right). The peculiarity of the PEC cell is that the working electrode (W.E., the cathode in our setup) does not face the counter electrode (C.E., the anode in our setup) in order to allow a direct illumination of the sample.

- The electrochemical (EC) tests have been carried on in a three electrode configuration using a miniaturized Ag/AgCl reference electrode (ET072-1, eDAQ), a Pt foil as anode and the catalyst as cathode. The current flow is measured with a potentiostat (CHI760D, CH Instruments, Inc.) using the ohmic potential drops (IR-compensation) to have a more accurate potential control. The EC measurements are carried in a two facing-chamber cell consisting of a working (cathode) and a counter (anode) chamber, separated by a proton exchange membrane (PEM, Nafion™ Membrane N117, Sigma-Aldrich).

The cathode chamber is filled with 11 ml of potassium bicarbonate 0.1 M (KHCO<sub>3</sub> – Sigma Aldrich, 99.5%) and maintained under continuous CO<sub>2</sub> flow (20 sccm) controlled with a mass-flow controller (EL-Flow Select, Bronkhorst) during the EC tests. The samples are contacted with conductive tape at the conductive side and isolated with kapton tape. The anode chamber is filled with 11 ml of potassium bicarbonate 0.1 M and maintained under continuous CO<sub>2</sub> flow (10 sccm) with a second mass-flow controller.

A gas chromatograph (microGC Fusion, Inficon) was employed to determine the concentration of gaseous products. It was equipped with two types of capillary columns for gas separation: a Porous Layer Open Tubular column (PLOT, whose gas separation is grounded on gas-solid partitioning, based on compound polarity), and Wall Coated Open Tubular column (WCOT, whose separation is grounded on gas-liquid partitioning, based on compounds boiling point).

The liquid products have been analysed using a High Performance Liquid Chromatograph (HPLC UltiMate 3000, Thermo Scientific).

- The photo-electrochemical (PEC) tests have been carried on in a three electrodes configuration using an Ag/AgCl reference electrode (Innovative Instruments, LF-1, 3.4M KCl), a Pt foil as anode and the catalyst as cathode. The current flow is measured with a potentiostat (Bio-Logic SP-300). The PEC measurements are carried out in a two chamber PEC cell consisting of a working (cathode) and a counter (anode) chamber, which are separated by an anion-exchange membrane (AGC Engineering, Selemion AMV). The PEC cell is equipped with continuous temperature control and a quartz window in the working chamber enabling photoelectrochemical measurements; for a detailed description see Corson et al. [22]

The cathode chamber is filled with 2.5 ml of potassium carbonate 0.05M ( $K_2CO_3$  - Alfa Aesar, 99.997% metals basis, pH 7.75) and maintained under continuous  $CO_2$  flow (5 sccm) during the PEC tests. The samples are contacted with conductive tape at the backside. A thermistor (Microlab, Model 103) covered with a heat-shrink fluorinated ethylene propylene (FEP) probe cover (Tef-Cap Industries) monitors the temperature of half-cell and kept it at 22°C with a planar Peltier element (Ferro Tec, 72008/131/150B). The anode chamber is filled with 0.8 ml of potassium carbonate 0.05M.

An AM 1.5 solar simulator at 100 mW/cm<sup>2</sup> intensity (16S-300-002, Solar Light) is used for front-side illumination.

A gas chromatograph (GC, SRI Instruments, Multiple Gas Analyzer 5) with a 120 HayeSep D column, argon carrier gas, and a gas-switching valve with a 1 ml sample loop is used for gaseous product analysis. The products are separated by the column flow through a Thermal Conductivity Detector (TCD) that detects  $H_2$  followed by a methanizer that converts CO and  $CO_2$  to  $CH_4$  and a Flame Ionization Detector (FID) that detects  $CH_4$ , ethylene ( $C_2H_4$ ), and ethane ( $C_2H_6$ ).

The performance of the samples are calculated by looking at:

- the **total current density**. The given information is related to the capability of the sample to extract electrons from the surface and transfer them to the adsorbed species. The higher the current density the more products are expected. However, some losses have to be taken into account like: capacitive currents due to the charging-discharging effect that can occur in presence of dielectric materials, and the RedOx processes which are modifying or degrading the catalysts themselves. If the bias-potential is high enough, the reduction of the material can occur with a change in the oxidation state of the constituting elements, thus a modification of the surface properties would be expected. For this reason,

the total charge is weighted considering the product concentration and type;

- the **Faradaic efficiency** (F.E.) is defined as the ratio between the charges exchanged to reduce the adsorbed molecules to a specific product ( $Q_{prod}$ ), over the total charges transferred ( $Q_{tot}$ ):

$$F.E. = \frac{Q_{prod}}{Q_{tot}}$$

Since the quantities measured in our system are the total current ( $I$ ) and the product concentration (ppm), the expression for the F.E. can be written as:

$$F.E. = \frac{n \cdot F \cdot mol}{I}$$

where  $n$  is the number of electrons involved in the reaction,  $F$  is Faraday constant and  $mol$  is the molar concentration of products. The latter can be also written as:

$$mol = \frac{\phi \cdot ppm}{V_{mol}}$$

where  $\phi$  is the flux of  $CO_2$  in the reactor and  $V_{mol}$  is the molar volume calculated from the gas equation  $pV = nRT$ , and whose value for  $CO_2$  at 25 °C at 1 atm is 24.47 L/mol.

Thus, the final equation is:

$$F.E. = \frac{n \cdot F \cdot \phi \cdot ppm}{V_{mol} \cdot I} \times 100$$

In case of liquid products the equation is modified as follows:

$$F.E. = \frac{n \cdot F \cdot ppm \cdot Vol \cdot \rho}{Q_{tot} \cdot MM} \times 100$$

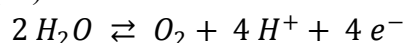
where  $Vol$  is the volume of the electrolyte present in the cathodic half-cell,  $\rho$  is the density of the product under investigation,  $MM$  is its molar mass, and  $Q_{tot}$  is the total charge transferred from the catalyst to the solution.

It is important to underline that the availability of  $CO_2$  molecules, dissolved in the electrolyte, close to the surface of the catalyst can drastically influence products selectivity. In fact, in proximity of the surface the concentration of  $CO_2$  is limited by its solubility and diffusivity. In addition, the release of OH ions from fast reduction reactions results in rising of pH values near the surface (called local pH), compared to the one in the bulk electrolyte. This high local pH can shift the equilibrium of the  $CO_2$  reduction reactions, resulting in the lowering of the selectivity toward certain target products. The main competitive reaction occurring is  $H_2$  evolution, run by the catalyst through protons reduction. The higher the applied potential, the more the diffusion limits shift the selectivity of the reduction processes to  $H_2$  evolution. On the other hand, high local pH values can lead to a mass transport limitation for protons, thus suppressing hydrogen evolution reaction. These results suggest that the roles of local pH and mass transport in  $CO_2$  electroreduction can be ambivalent and have to be taken into account to properly discuss products selectivity.[23]

The overall Faradaic efficiency can be lower than 100 % because of the so-called Faradaic losses. They occur when electrons or ions participate in unwanted side reactions. These losses generate heat and/or chemical by-products. Even when the desired products are produced, losses can still occur if they recombine. At last, the material reduction (or oxidation) mediated by the injected electrons (or holes) can participate to the losses too.

## 2.5 Electronic and electrical properties

CO<sub>2</sub> reduction is run in a liquid medium, the electrolyte, based of water and salt. It is the source of protons, used to reduce CO<sub>2</sub> to hydrogenated compounds (like CH<sub>4</sub>, H<sub>3</sub>COH and HCOOH) and of electrons too. The anode, which oxidizes water, extracts them following a path similar to the one carried on by the Oxygen Evolving Complex (see Chap.1):



The salt, commonly a carbonate, is used to enhance the conductivity of water thus properly closing the circuit linking the cathode to the anode.

A deeper understanding of the phenomena occurring at the catalyst surface comes from the study of the catalyst/electrolyte interface. Several information on the behaviour of the material and on the charge transfer kinetics, both at the surface as well as in the bulk, can be extrapolated using the electrochemical approach.

### 2.5.1 Mott-Schottky technique

The Mott-Schottky technique is a powerful tool for the study of the band alignment at the surface of the catalyst. It is used to measure the changes that occur in an electrochemical interface as its DC voltage is changed. A fixed-frequency, small-signal AC potential excitation is applied to the electrochemical cell. The impedance of the working-electrode interface is measured as a function of DC voltage, thus producing the so-called Mott-Schottky plot in which the variation of the surface/electrolyte ideal capacitor (expressed as  $1/C^2$ ) is shown respect to the applied potential.

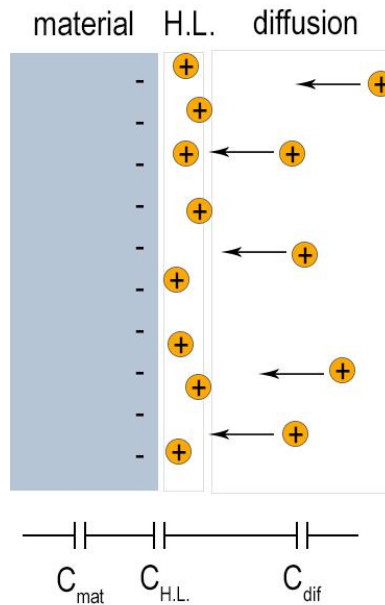


Figure 11. The material/electrolyte system can be divided into three main parts. The material itself is a metal oxide whose capacity is described by  $C_{mat}$ ; the layer of oriented charge located inside the electrolyte, in contact with the material, is called Helmholtz layer (H.L.) and represent one of the two plates of the condenser labeled  $C_{H.L.}$ . Lastly, the ion-diffusion that occurs inside the electrolyte is described by the capacitor  $C_{dif}$ .

The catalyst-electrolyte system is a complex series of capacitances (Figure 11). The main contributions come from:

- the Helmholtz layer ( $C_{HL}$ ), a layer of oriented charge present in the solvent close to the catalyst interface;
- the diffusion layer ( $C_{Dif}$ ), represented by the ions dissolved in the electrolyte which are approaching the electrode;
- the material itself ( $C_{cat}$ ), which is a dielectric.

If we consider them ideal capacitors (with flat and parallel plates), since they are put in series, the equivalent capacity ( $C_{eq}$ ) is dominated by the lowest contribution, which comes from the material.

$$\frac{1}{C_{eq}} = \frac{1}{C_{HL}} + \frac{1}{C_{Dif}} + \frac{1}{C_{cat}}$$

A Schottky-diode is used to simulate the interface: the catalyst is represented by the semiconductor and the electrolyte by its RedOx potential (Figure 12).

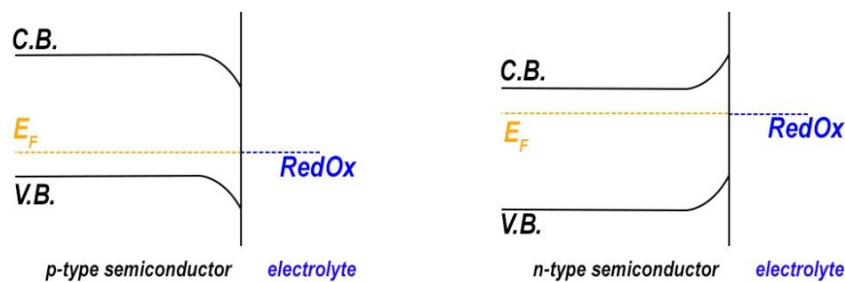


Figure 12. Semiconductor/electrolyte interface for p (left) and n-type (right) semiconductors.

The band alignment is measured by applying an oscillating potential and collecting the output current at a specific frequency of 10 kHz. At this frequency only fast processes are taken into account, therefore it is possible to neglect the contribution of ion diffusion and the charge transfer mechanism occurring in the bulk of the catalyst. The Mott-Schottky relation has been used to calculate the flat band potential:

$$\frac{1}{C^2} = \frac{2}{\varepsilon \cdot A^2 \cdot q \cdot N_D} \left( V_{bi} - V - \frac{k_B T}{q} \right)$$

where  $C$  is the capacitance of the material,  $q$  is the elementary charge,  $V$  is the applied voltage vs RHE,  $k_B$  is the Boltzmann constant,  $T$  is the absolute temperature,  $V_{bi}$  is the built-in potential of the material/electrolyte interface,  $\varepsilon$  is the dielectric constant,  $N_D$  is the density of dopants and  $A$  is the surface area.

It is possible to gain information on the built-in potential between surface and electrolyte, together with a quantitative information on the major charge carriers of the catalyst. In fact, by fitting the linear part of the capacitance plot, where  $1/C^2$  is plot vs the applied potential variation, with the Mott-Schottky relation it is possible to:

- calculate the built in potential via the following formula:

$$V_{bi} = - \left( \frac{\text{intercept}}{\text{slope}} k_B T \right)$$

where  $k_B T$  is equal to 26 mV, since we are operating at room temperature;

- gain, with good approximation, information on the charge-carrier density:

$$N_D = \frac{2}{\varepsilon A^2 q \text{ slope}}$$

While for the semiconductor, the energy levels are defined with respect to the vacuum level, the RedOx potential of the electrolyte is defined with respect to a reference electrode, commonly SHE. The correlation among the SHE and vacuum level, is expressed by:

$$SHE = -4.44 \text{ eV vs vacuum level at } 25 \text{ }^\circ\text{C}$$

In this way, it is possible to calculate the RedOx potential using the Nernst equation and relate it to the vacuum level.

Mott-Schottky measurements have been conducted by scanning the potential between -0.44 V and 0.76 V vs RHE with a 0.1 V step voltage. A sinusoidal signal with 10 kHz frequency, as previously discussed, and 25 mV amplitude was superimposed to the constant bias to obtain the capacitance of the material/electrolyte capacitor.

## 2.5.2 Electrochemical impedance spectroscopy

Electrochemical impedance spectroscopy (EIS) is a technique used to study the harmonic response of an electrochemical system. A small, sinusoidal variation

is applied to the potential at the working electrode, and the resulting current is analyzed in the frequency domain.

The real and imaginary components of the impedance, represented in the Nyquist plot, give information about the kinetic and mass transport properties of the cell, as well as the surface properties through the double layer capacitance.

By probing the system with different frequencies, it is possible to separate the contribution of the slowest process from the fastest one at each applied voltage. This approach allows to gain a complete information on the impedance ( $Z$ ) of the material itself and the junction formed with electrolyte (Figure 13).

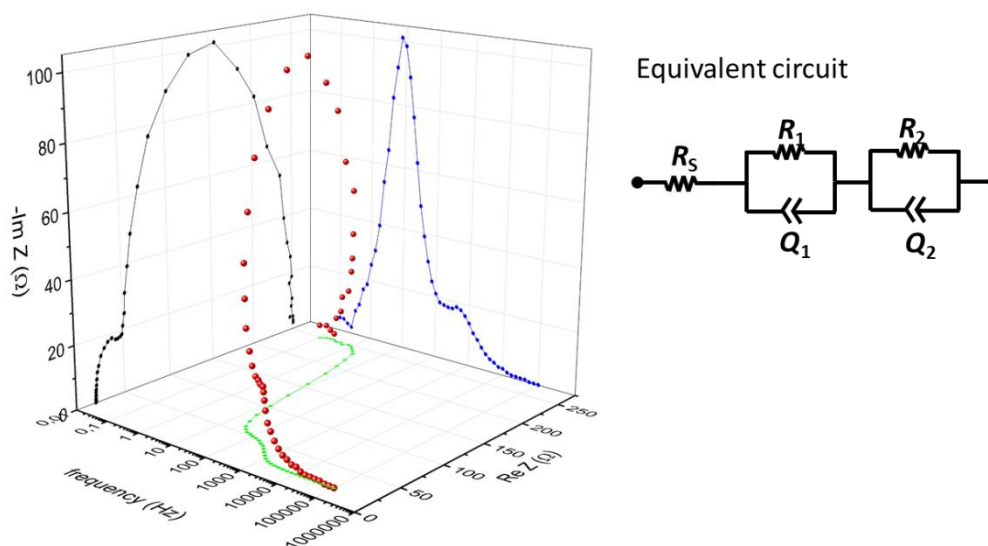


**Figure 13.** Three-dimensional plot, simulated with ZSimpWin software, showing the real and imaginary part of the impedance as a function of the frequency (red dots). It represents the response of a sinusoidal signal of the circuit (inset on the right). The projection of  $\text{Re}Z$  respect to  $-\text{Im}Z$  (black curve) is called Nyquist plot.

The fitting of the Nyquist plot helps to reconstruct an equivalent circuit, representative of the resistive and capacitive processes occurring during the electron transport.

Commonly, the interfaces are modelled as a parallel  $RC$  circuit, while the dissipation due to the back contact, the resistivity of the electrolyte, the clamps, wiring, etc. with a series resistance, and the diffusion of reagents and products from and to the surface using specific elements called Warburg impedances.

The electrical elements used are physically correlated with:

- $R_s$ : series resistance related to the electrolyte and the contact resistances of the electrodes;
- $R_{tr}$ : resistance to the electrons transfer inside the material;
- $Q_{cat}$ : constant phase element related to the capacitance of the electrons inside the material;
- $R_{ct}$ : charge transfer resistance related to the surface/electrolyte interface;
- $Q_{dl}$ : constant phase element related to the double layer capacitance at the surface/electrolyte interface;

- $Z_O$ : Warburg impedance related to the diffusing ion species in the electrolyte.

In most cases, since the capacitive behaviour is not ideal, a constant phase element ( $Z_{cfe}$ ) is used. Its impedance is defined as:

$$Z_{cfe} = \frac{1}{(j\omega)^a Q}$$

In the limit of  $a$  that tends to 1, the  $Z_{cfe}$  is equal to the impedance of the capacitor. However, when this approximation is not valid, the equivalent-capacity ( $C_{eq}$ ) can be calculated by looking at the parallel RC-circuit. The resulting calculation for  $C_{eq}$  is:

$$C_{eq} = \frac{(RC)^{\frac{1}{n}}}{R}$$

The EIS measurements were carried out in the frequency range between 1 MHz and 1 Hz with an AC signal amplitude of 10 mV. The potential range was varied depending to the sample working-potential. By fitting the Nyquist plots, we obtained information on the characteristic transfer time of charges from the surface to the electrolyte.

# Chapter 3

## Tin oxide (SnO<sub>2</sub>)

### 3.1 Introduction

#### 3.1.1 State of the art

Tin oxide (SnO<sub>2</sub>) is a wide band gap semiconductor (3.6 eV) usually considered as an oxygen deficient n-type semiconductor. It has been employed in different fields such as solar cells, catalysis, in solid-state chemical sensors, CO<sub>2</sub> valorisation, etc.[24,25]

SnO<sub>2</sub> is an attractive material because of its catalytic power, selectivity to formate, and non-noble, eco-friendly, and low-cost characteristics.[26] The surface properties of SnO<sub>2</sub> are the responsible of its widespread application. By managing the dual valence of Sn it is possible to tune its properties. In fact, depending on the oxygen chemical potential of the system, the valence of Sn at the surface can be changed from 4+, characteristic of stoichiometric surfaces, to 2+.[27]

Several factors can influence the catalytic properties, among them: the crystal size, the material morphology, and the surface modification. For this reason, a great number of methods have been developed to prepare nanostructured SnO<sub>2</sub> catalysts. Among them: hydro-thermal synthesis, [28,29] aerogel, [30] solvo-plasma technique, [31] electrodeposition, [32] and electrostatic spinning.[33]

However, in order to guarantee the reproducibility and scalability, anodic-oxidation (AO) of tin foils has been employed to realize SnO<sub>2</sub>. It is a simple, high yield, low-cost, scalable, and effective strategy to prepare nanostructured porous materials.[34] Moreover, this technique allows to prepare high surface area sponge-like structures, with pore walls made of small interconnected nanoparticles.

A drawback of SnO<sub>2</sub> is that it can be reduced to metallic Sn at high negative potentials, thus causing a significant decrease of the efficiency through formate production. Broekmann and co-workers [35] observed this phenomenon by

monitoring Sn oxidation state changes during the CO<sub>2</sub> electrochemical reduction by using in operando Raman spectroscopy. This result gives the evidence that the oxide forms have improved catalytic performances, and that the surface analysis of the oxidation state is required to better understand the outcomes coming from CO<sub>2</sub>-valorization tests.

Bejtka et al.[36] demonstrated that SnO<sub>2</sub>, realized via AO, is capable to reduce CO<sub>2</sub> to formic acid.

The mesoporous structures, created during the synthetic process, allow the easy access of the electrolyte to the catalytic sites and efficient mass diffusion.[37] Moreover, the nanostructuration with tailored surface configuration proved to be an effective strategy to enhance the catalytic activity.[38,39]

The collaboration with Bejtka's group aimed to optimize the synthesis of porous SnO<sub>2</sub> and to establish the protocols for the characterization of the material structure and morphology as well as of its catalytic activity toward CO<sub>2</sub> reduction. A great effort has been also devoted in the study of the stability of the material during the tests.

Since some studies demonstrated that, in systems containing precious metals, like Au and Cu, the broken spatial symmetry near grain boundaries changes the binding energy of the reaction intermediate facilitating the CO<sub>2</sub> reduction to CO [38] and its reduction to C<sup>2+</sup> products, [39] the interest was aroused in the study of modified-SnO<sub>2</sub>.

Therefore, doping and substitution have been investigated as possible ways to induce nanostructure modification, together with the density of states engineering to push the catalytic properties of SnO<sub>2</sub> through CO<sub>2</sub> valorisation.

### 3.1.2 Synthetic approaches

The catalytic properties of SnO<sub>2</sub> can be tuned by doping or substitution. From DFT calculations, Ti, V, Nb, Ta and Zr dopants were found to be most stable.[18] The effect of doping resulted in an upward shift in the Pourbaix diagram boundary separating the [3H/1CO<sub>2</sub>] and [4H/1CO<sub>2</sub>] states. This means these dopants should result in a lower over-potential, than un-doped tin oxide, for CO<sub>2</sub> reduction. For this reason, these dopants have been suggested by Saravanan et al.[18] as good candidates for future experimental investigations on energetically efficient CO<sub>2</sub> reduction.

Since the present work aim to look preferentially to sustainable processes and Earth abundant elements for the catalyst preparation, Ti and Fe have been selected for substitution (Ti<sup>4+</sup>) and p-doping (Fe<sup>3+</sup>).

While the intercalation of Ti (IV) has been already discussed by other authors, [18] Fe(III) p-doping is expected to cause a downward band bending at the catalyst/electrolyte interface. This would improve electrons migration to the surface, and so, to CO<sub>2</sub> adsorbed at the surface.

## 3.2 SnO<sub>2</sub> synthesis and doping

### 3.2.1 Material synthesis

SnO<sub>2</sub> was synthesized via AO, following the procedure presented by Bejtka et al.[36] As previously stated, anodic oxidation is a simple, scalable and easily reproducible technique that allows the realization of nanostructured porous oxides with high surface area. The precursors, in particular the dopants, have been chosen not to leave poisoning elements in the oxide structure after the annealing, thus avoiding purification cycles.

A one-step anodic oxidation method was employed in a homemade two-electrode cell, using Sn foil (0.15 mm thick, purity 99.7%, Goodfellow) as the anode and a Pt foil as the cathode. Prior to anodization, the tin foils were ultrasonically cleaned in acetone (99% purity, Sigma-Aldrich) and ethanol (99% purity, Sigma-Aldrich) and then dried in a N<sub>2</sub> stream.

The electrolyte used was a solution 0.3 M of water and sodium hydroxide (NaOH, ≥98.0 wt %, Sigma-Aldrich). The applied anodization voltage was 10 V, under continuous stirring in an ambient environment. The as-anodized samples were carefully rinsed with deionized water and dried with N<sub>2</sub>.

It is interesting to notice that the NaOH solution can be neutralized using hydrochloric acid (HCl), thus forming water and sodium chloride (NaCl), a non-toxic salt, which does not have any impact on the environment after the disposal.

A simple doping procedure have been developed following Jain et al. [40] paper on Ni-doped SnO<sub>2</sub>. Briefly, a 600 °C annealing has been used to intercalate the dopants in the oxide structure.

A SnO<sub>2</sub> powder was produced by sonicating the as-anodized samples in isopropanol (99% purity, Sigma-Aldrich) until the Sn substrate was completely uncovered. The powder was then precipitated using a centrifuge at 2400 rpm for 15 minutes. The wet powder was then mixed with the precursors for the doping.

Since the desired ratio was 1.5 %mol for both the Ti-SnO<sub>2</sub> and Fe-SnO<sub>2</sub>, a concentration of Ti(IV)-isopropoxide (97 % purity, Sigma-Aldrich) of 2.83 % wt and Fe(III)-nitrate nonahydrate (98 % purity, Sigma-Aldrich) of 4.02 % wt, was calculated. These precursors have been chosen because the anions leave the doped-SnO<sub>2</sub> without any trace. Few millilitres of ethanol were add to the mixture and sonicated in order to well disperse the precursor.

The powder mixture was then put in an oven (Nabertherm GmbH) and heated in air at 600 °C for 4 h.

### 3.2.2 Electrode preparation

To prepare the SnO<sub>2</sub>-based gas-diffusion electrode (GDE), 10 mg of synthesized doped-SnO<sub>2</sub>, 1.5 mg of acetylene carbon black (CB, Shawinigan Black AB50), 90µLofNafion 117 solution (5 wt %, Aldrich), and 320µL of isopropanol were well mixed and sonicated for 30 min until a uniform slurry was

obtained. The slurry was then coated onto a carbon paper gas diffusion layer (GDL; SIGRACET 28BC, SGLTechnologies). The GDE was dried at 60°C overnight to evaporate the solvents.

For sake of comparison, a powder of SnO<sub>2</sub> annealed at 600 °C for 4 h was prepared following the same procedure presented above, keeping the same loading of catalyst.

### 3.3 Morphology, structure and surface chemistry characterizations

The morphology of the samples was studied with FESEM, using the EDX to gain information on the elements present in the material. In this way, a direct confirmation of Fe and Ti presence was obtained. XRD was then performed in Bragg-Brentano configuration on powder samples, in order to determine the phase of the doped and un-doped SnO<sub>2</sub> crystals. Their dimension has been estimated using the Scherrer equation.

XPS was then performed to study the surface chemistry. HR-XPS spectra were analysed to gain several information, such as:

- Sn oxidation state, by looking at Sn 3d peak as well as to the valence band shape;
- Ti and Fe presence at the surface and their valence number, to unravel the induced-doping type;
- Valence band relative position among the doped and un-doped samples.

The SnO<sub>2</sub> samples annealed at 600°C display a structure similar to the one described by Bejtka et al. [36]The structure is irregular and porous (Figure 14 a-d), composed by nanochannels, with a 50 nm mean diameter, oriented along the growth direction, with wall thickness of about 15 nm.

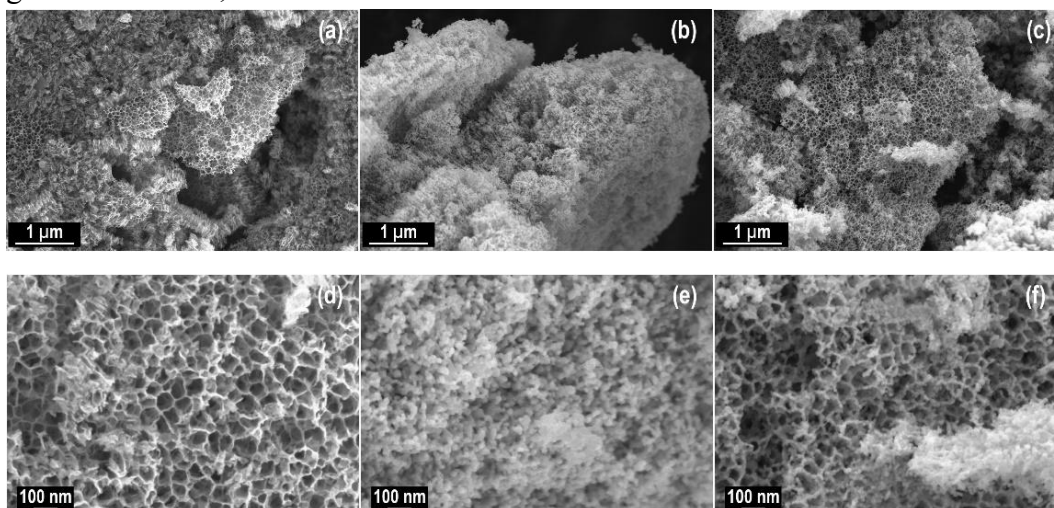


Figure 14. FESEM imaging of (a-d) SnO<sub>2</sub>, (b-e) Fe-SnO<sub>2</sub> and (c-f) Ti-SnO<sub>2</sub> samples.

A similar result has been obtained also by the groups of Palacios-Padròs and Jeun,[41] whose SnO<sub>2</sub> realized by anodic oxidation exhibited straight and vertically aligned nanochannels, with fully open pores, whose diameter is compatible with the one we measured.

As regard the doped-SnO<sub>2</sub> samples, Ti substitution leads to the formation of bigger crystals, clearly discernible in the high magnification image (Figure 14 e). In fact, the border of the pores looks less smooth, due to the emerging crystal grains. The process is even more emphasized in the Fe-SnO<sub>2</sub>, for which the channels disappear, leaving a highly rough and disordered surface structure (Figure 14 f).

The EDX analysis confirms the presence of Fe and Ti in the doped-SnO<sub>2</sub> powder samples (data not shown). The lack of metal clusters suggests the dopants are well spread and completely inserted in the SnO<sub>2</sub> lattice.

XRD was used in Bragg-Brentano configuration to study the crystalline phase of the SnO<sub>2</sub> samples. The patterns correspond to SnO<sub>2</sub> (JCPDS 00-040-1445) with no significant variations among the doped and un-doped samples (Figure 15).

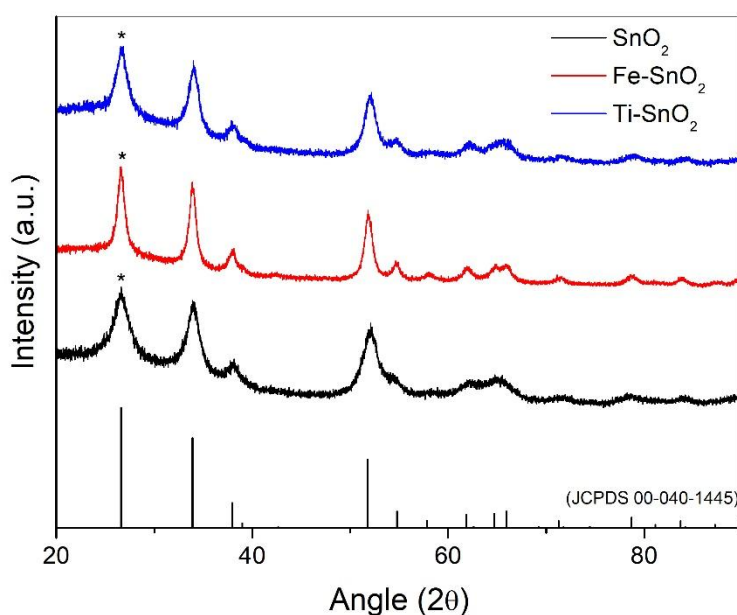


**Figure 15.** XRD patterns of SnO<sub>2</sub> samples compared with SnO<sub>2</sub> reference oxide (JCPDS 00-040-1445). The peaks labeled with the star (\*) have been chosen to calculate the crystals mean dimension.

The most intense peak, corresponding to the 110 plane, has been used to observe the lattice modification induced by ion insertion. A slight 2θ shift has been observed, thus suggesting the ion intercalation caused a strain in SnO<sub>2</sub> lattice.

The information coming from the FWHM values variation has been treated using the Scherrer relation to calculate the mean dimension of the crystalline domains. The fixed parameter used for the computation are the shape factor of 0.9 [42] and 0.1541 nm of X-ray wavelength, corresponding to the Cu K-alpha. It

turned out a mean dimension of  $(5.5 \pm 0.1)$  nm,  $(12.3 \pm 0.1)$  nm,  $(8.0 \pm 0.2)$  nm for SnO<sub>2</sub>, Fe-SnO<sub>2</sub> and Ti-SnO<sub>2</sub> respectively.

The trend in the crystal dimension reflect the observations pointed out in the discussion of FESEM top-surface imaging. The variation in crystal dimensions is the main responsible of surface modification and pores closure.

Concerning the surface chemical composition, SnO<sub>2</sub> samples were characterized with XPS, using C 1s peak (284.5 eV) to calibrate the spectra.

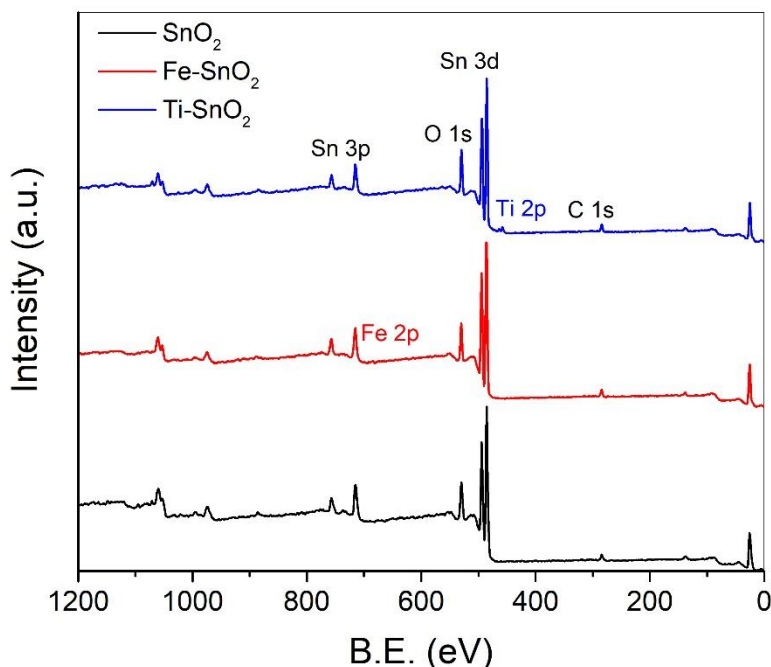


**Figure 16.** XPS survey spectra of SnO<sub>2</sub> samples. The labels indicate the elements and the orbitals related to the most intense peaks. While Fe 2p and Ti 2p are present only in doped-SnO<sub>2</sub>, Sn 3p, Sn 3d, O 1s and C 1s have been found in all the samples.

The survey spectra are reported in Figure 16, where only Sn and O, with a small traces of adventitious carbon were observed in all samples. In doped-SnO<sub>2</sub> samples, also Fe (more evident in the HR-XPS spectra, Figure 20 a) and Ti have been observed, in good agreement with EDX results.

The Sn 3d doublet of SnO<sub>2</sub> is located at 485.9 eV (Sn 3d 5/2) and 494.3 eV (Sn 3d 3/2). Since the peaks of Sn (II) and Sn (IV) are close to each other, is not trivial to distinguish the oxidation state of the compound by just looking at the Sn 3d peak position. For this reason, the valence band shape has been used for the identification. The oxidation state results to be Sn (IV), as also suggested by the 8.4 eV peaks distance related to the spin-orbit split. As regard the ratio among the areas, the value of 3:2 is obtained, in good agreement with the theoretical calculations summarized in the second chapter.

It is interesting to notice the presence of a shoulder at low binding energy, found in all HR-XPS spectra of un-doped SnO<sub>2</sub> (Figure 17). It is associated to the poor conductivity of the un-doped samples that led to surface charging.

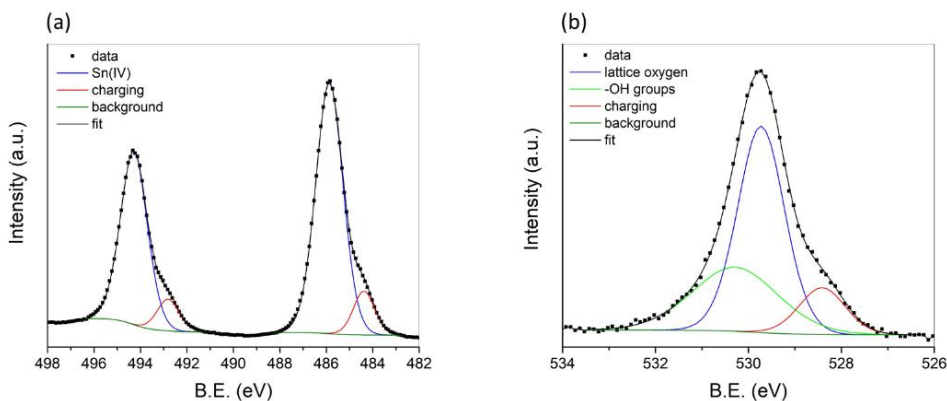


**Figure 17. HR-XPS of SnO<sub>2</sub> related to (a) O 1s and (b) Sn 3d peak components.**

The O 1s spectrum confirms the presence of lattice oxide, displaying a strong component located at 529.7 eV, with a small contribution coming from the –OH species, as defined by the component at 530.3 eV.

As regard the doped-SnO<sub>2</sub>, no significant differences have been found in the O 1s spectra (Figure 18).

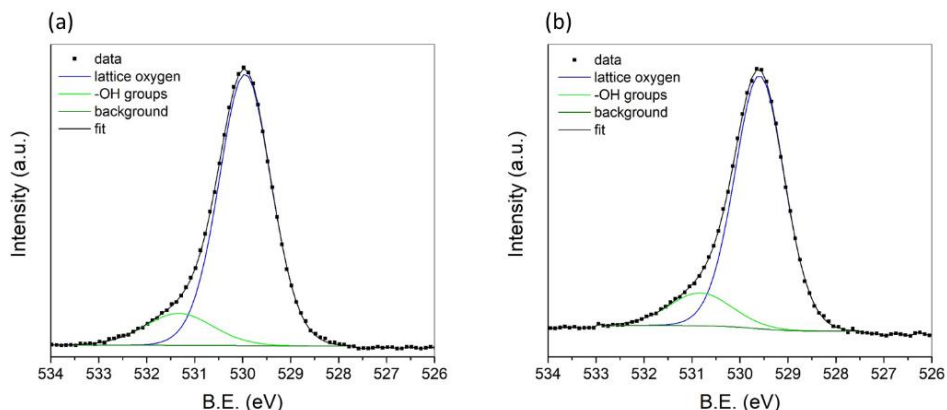


**Figure 18. HR-XPS of doped-SnO<sub>2</sub> O 1s components of (a) Fe-SnO<sub>2</sub> and (b) Ti-SnO<sub>2</sub>.**

In fact, the peak is dominated by a stronger component related to lattice oxide, set around 529.7 eV, and a smaller related to –OH groups at higher binding energies. A slight variation in the areal ratio of the presented components has been found only in Ti-SnO<sub>2</sub>, for which the component at 529.7 eV exhibits a larger area. Since the component comprised between 530.3–530.8 eV depends on physisorbed water, as well as on C–O bonds present in adventitious carbon, we consider this difference among the samples can be ascribed to a different amount of contaminants.

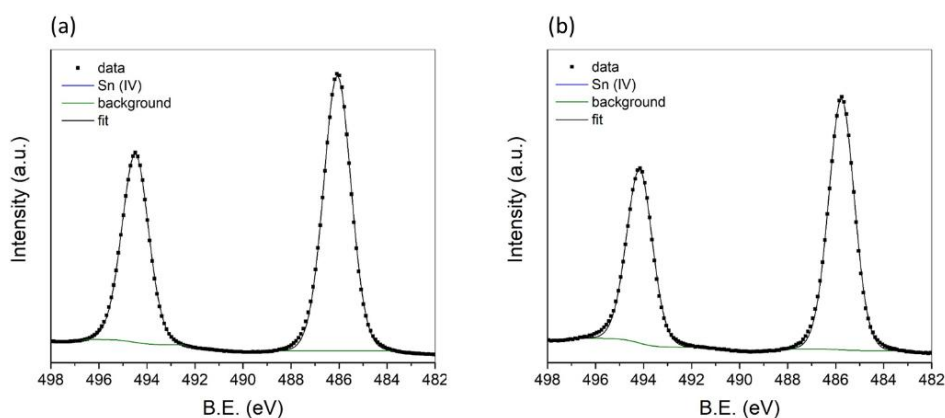


**Figure 19.** HR-XPS of doped-SnO<sub>2</sub> Sn 3d components of (a) Fe-SnO<sub>2</sub> and (b) Ti-SnO<sub>2</sub>.

By looking at the Sn 3d components (Figure 19), it has been found that while the Ti-SnO<sub>2</sub> matches the peak position of un-doped SnO<sub>2</sub>, a 0.2 eV shift at higher binding energies has been found for Fe-SnO<sub>2</sub>. According to Thirumala Rao et al.,[43] two satellite peaks would be expected at around 488 and 493 eV since the addition of Fe would lead to the formation of vacancies, thus changing the oxidation state of Sn (IV). This result would be promising for Fe-SnO<sub>2</sub> application in CO<sub>2</sub> valorisation, since oxygen vacancies are believed to participate in the catalysis by enhancing CO<sub>2</sub> adsorption and, as a consequence, its reduction.[44] Even if these satellite peaks cannot be easily deconvoluted from the Sn (IV) component, the 0.2 eV shift can be ascribed to the presence of Sn (II) states (NIST Standard Reference Database 20) anyhow.

As regard the dopants (Figure 20), Ti 2p doublet is located at 458.0 eV and 463.7 eV, with a 5.7 eV distance and an areal ratio of 1:2. The peak distance and position is ascribable to Ti (IV), therefore Ti-intercalation is not expected to change the doping of SnO<sub>2</sub>. Moreover, the results are in good agreement with the one obtained by Ran et al. [45] for their Ti-doped SnO<sub>2</sub> hollow structures.

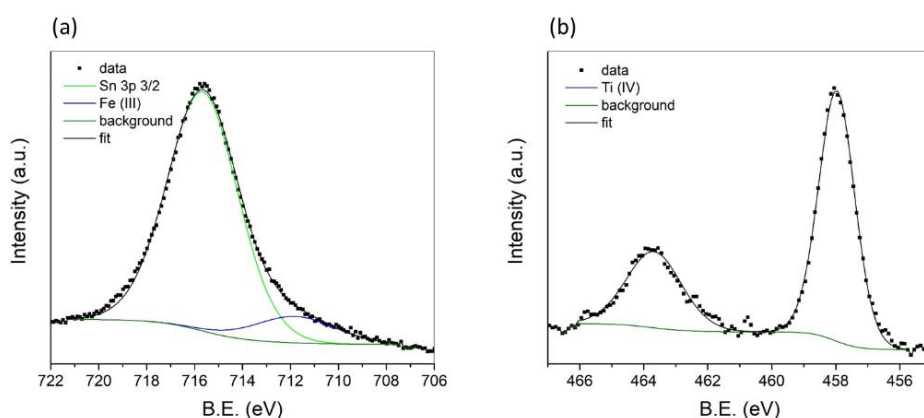


**Figure 20.** HR-XPS of doped-SnO<sub>2</sub> components related to (a) Fe2p and (b) Ti2p orbitals.

On the other hand, the peak of Fe 2p 3/2 stands at 711.8 eV. The position is connected to the oxidation state of Fe (III). Since no information on metallic Fe has been found, we can conclude SnO<sub>2</sub> has been successfully doped with Fe (III). The close peak, located at 715.7 eV is referred to Sn 3p 3/2, which is partially

overlapping the Fe 2p doublet. Xing et al.[46] observed the same superposition of Sn 3p and Fe 2p orbitals in Fe ion-doped SnO<sub>2</sub>/multi-walled carbon nanotube composites.

### 3.4 CO<sub>2</sub> valorisation and stability tests

Formate or formic acid are valuable products because of their versatility. In fact, they are currently employed in different fields, such as direct formic acid fuel cells, and the industries of leather, textile, and food.[47] These results raise the interest on crystalline SnO<sub>2</sub>.

The formation of formate and CO follows three possible pathways:[26]

*Pathway 1:* a one-electron transfer to CO<sub>2</sub> forms a CO<sub>2</sub>•<sup>-</sup> radical anion, leaving it bonded at the surface of the catalyst through the oxygen atoms. The protonation takes place on the exposed carbon atom and forms an HCOO• intermediate. Then, a second electron transfer and protonation step result in the HCOOH product.

*Pathway 2:* theoretical calculations propose the formation of •OCHO intermediates after the HCOO•, via an electron transfer. After that, HCOOH production occurs via the •OCHO protonation step.

*Pathway 3:* when the carbon in CO<sub>2</sub>•<sup>-</sup> is bonded to the electrode surface, the CO<sub>2</sub>•<sup>-</sup> may also be reduced via the protonation of its oxygen atom, resulting in the formation of •COOH. This intermediate is then either reduced to HCOOH or loses H<sub>2</sub>O to form CO.

Anodic oxidized SnO<sub>2</sub> was already characterized by Bejtka et al. [36] for CO<sub>2</sub> reduction to HCOOH and CO. The results of this collaboration, as previously mentioned, allowed to establish the protocols for:

- electrode preparation, by optimizing the catalyst loading to reach a uniform coverage;
- cell configuration and analysis procedures;
- stability studies based on the study of morphological changes and variation in crystals dimensions due to the reduction of the catalyst itself occurring at high applied potentials.

In order to analyse the catalytic properties of the materials, they have been tested in the same potential range (from -0.69 to -0.99 V vs RHE), by looking at the maximum of formic acid production. CO and H<sub>2</sub> are commonly detected as secondary products. It is possible to take advantage of them for syngas production.

Stability test have been performed, laying at the potential of -0.98 V vs RHE, corresponding to the maximum HCOOH production, looking for variations in the conductivity and selectivity of the samples.

Moreover, since a high negative potential can modify the samples chemical structure, FESEM and XRD characterization have been performed on doped-SnO<sub>2</sub> electrodes after the catalytic tests.

### 3.4.1 CO<sub>2</sub> valorisation tests

From the CO<sub>2</sub> valorisation tests, HCOOH, CO and H<sub>2</sub> have been found as the major products.

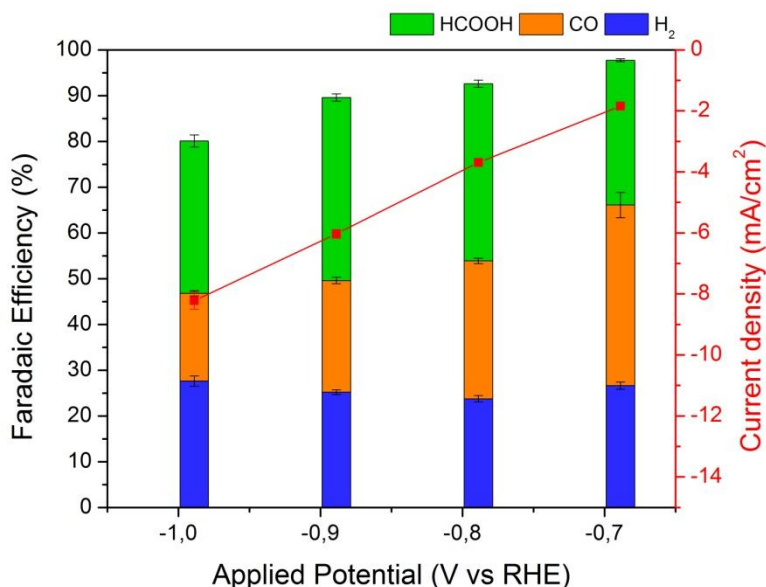
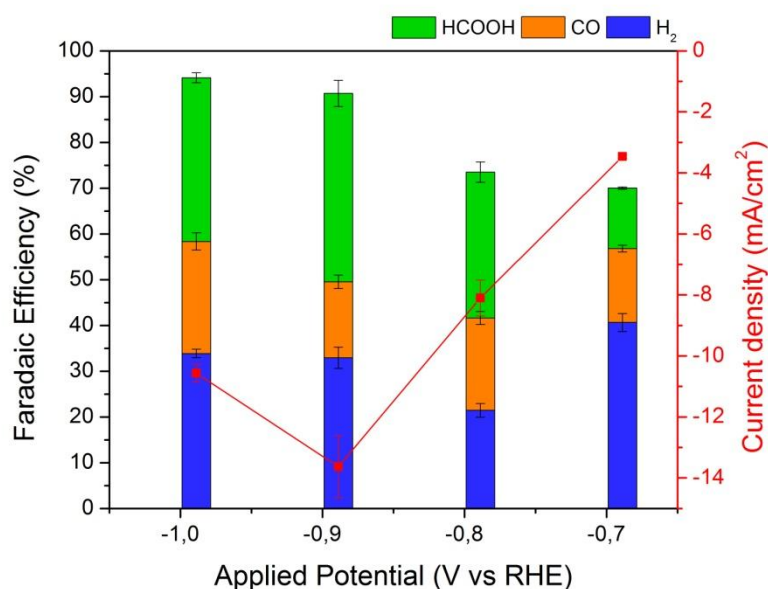


Figure 21. Bar chart showing the Faradaic efficiencies of SnO<sub>2</sub> at different applied potentials. In red, the current density recorded.

Un-doped SnO<sub>2</sub> exhibits a maximum of HCOOH production at -0.89 V vs RHE with (40.0 ± 0.8) % of FE (Figure 21). The secondary products are H<sub>2</sub> ((25.2 ± 0.5) %) and CO ((24.4 ± 0.7) %). As expected, while the applied potential negatively increases, the equilibrium of the reaction moves from CO<sub>2</sub> valorisation to H<sub>2</sub> evolution, in fact a lower amount of CO is measured. The sample performed CO<sub>2</sub> reduction for 1 h with a current density set to (-6.0 ± 0.2) mA/cm<sup>2</sup> at the equilibrium, kept stable over time.



**Figure 22.** Bar chart showing the Faradaic efficiencies of Fe-SnO<sub>2</sub> at different applied potentials. In red, the current density recorded.

Fe-SnO<sub>2</sub> exhibits the maximum of HCOOH production at the same potential of SnO<sub>2</sub> (-0.89 V vs RHE) also preserving the selectivity, with a FE of (41 ± 3) % (Figure 22). At this potential, CO<sub>2</sub> is reduced mainly to HCOOH, with just (17 ± 1) % of FE related to CO. The second main product is H<sub>2</sub> ((33 ± 2) %). Interestingly, the current density of Fe-SnO<sub>2</sub> is more than two times higher than SnO<sub>2</sub>, with a value at the equilibrium of (-14 ± 1) mA/cm<sup>2</sup>.

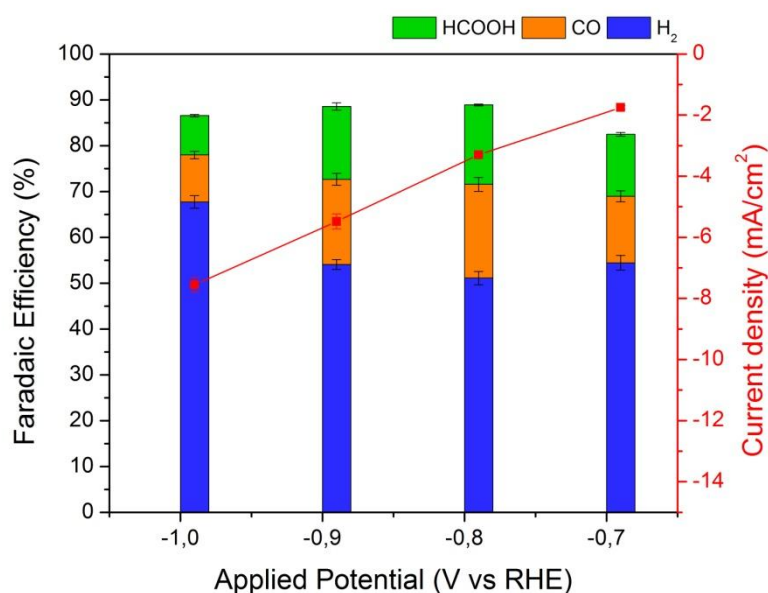


**Figure 23.** Bar chart showing the Faradaic efficiencies of Ti-SnO<sub>2</sub> at different applied potentials. In red, the current density recorded.

Contrary to the DFT results presented in the previous section, [18] Ti-SnO<sub>2</sub> shows a higher selectivity for hydrogen production than for CO<sub>2</sub> valorisation, resulting in a selectivity of (54 ± 3) % for H<sub>2</sub>, (19 ± 1) % for CO and (15.9 ± 0.8)

% for HCOOH (Figure 23). Even if the potential required to reach the maximum HCOOH production is 0.1 V lower (-0.79 eV vs RHE) than the sample previously presented, the current density are  $(-3.30 \pm 0.04)$  mA/cm<sup>2</sup> at -0.79 eV vs RHE, and  $(-5.5 \pm 0.2)$  mA/cm<sup>2</sup> at -0.89 V vs RHE.

As a final result, Fe-SnO<sub>2</sub> proves to be the best candidate for CO<sub>2</sub> valorisation, with the highest HCOOH production and selectivity, and the highest current densities. A good reproducibility of the results has been evaluated within a tolerance of 10 %.

### 3.4.2 Stability tests

The samples have been tested for three more hours at a fixed potential, looking at the stability of the material. The product sampling has been carried on each hour and the electrolyte changed after sampling.

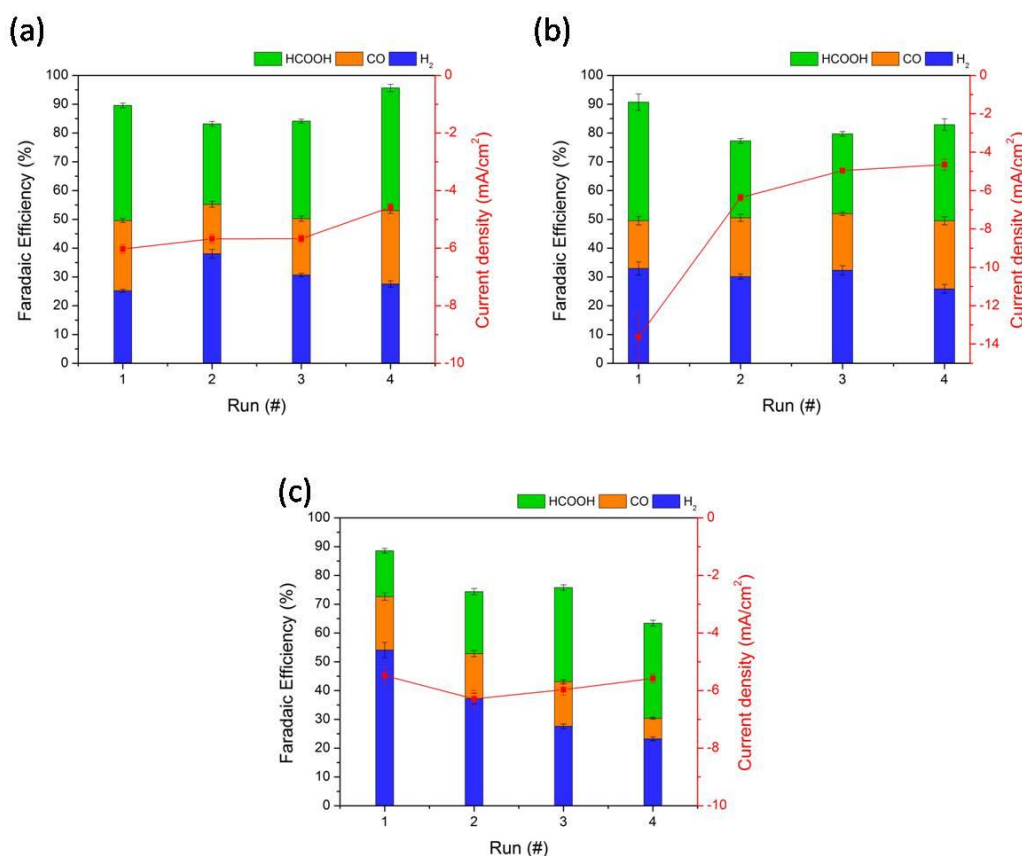


**Figure 24.** Stability tests carried on for four run in order to record the changes occurring over time in selectivity (Faradaic efficiency) and current density. The samples are labeled as (a) SnO<sub>2</sub>, (b) Fe-SnO<sub>2</sub> and (c) Ti-SnO<sub>2</sub>.

It turned out that the selectivity decreases along with the current density (Figure 24). Moreover, no significant differences have been found anymore among the doped and un-doped samples, thus suggesting the SnO<sub>2</sub> has been modified during the long-time electrochemical test.

These outcomes are in good agreement with the results of Bejtka's group. [36] They found both the morphology, the crystallinity and the chemical nature of the material were modified during the EC test.

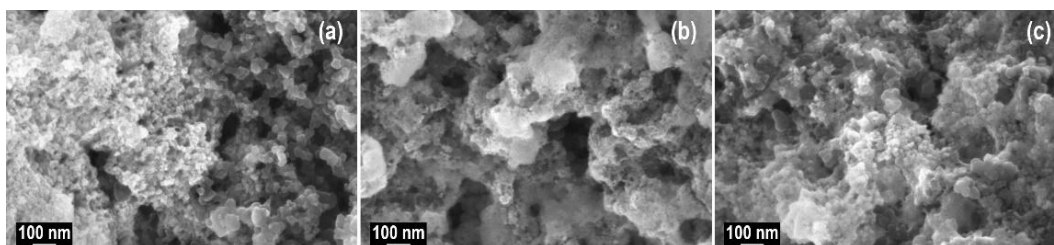


Figure 25. FESEM imaging of (a) SnO<sub>2</sub>, (b) Fe-SnO<sub>2</sub> and (c) Ti-SnO<sub>2</sub> electrodes after the electrochemical tests.

The top surface of the tested SnO<sub>2</sub> electrodes exhibits a disordered nanostructure formed by larger nanoparticles (Figure 25). The morphological change has been described by the tendency of SnO<sub>2</sub> to recrystallize or aggregate. In agreement with Bejtka et al. observations, the electrochemical test is the primary cause, because of the succession of reduction and oxidation processes. In fact, operando measurement demonstrated that the Sn (II) is formed at the potential corresponding to the maximum FE for HCOOH. [48,49] This result has been also confirmed by the presence of the RedOx peaks in the cyclic voltammeteries, which are related to the described change in the oxidation state of tin. The reduction peak from 0.0 to -0.4 V is attributed to the reduction of Sn species and it couples to the re-oxidation peak from 0.05 to 0.5V.[50]

As a result of the XRD analysis on the electrodes (Figure 26), the mean dimension of crystals was found to be enhanced.

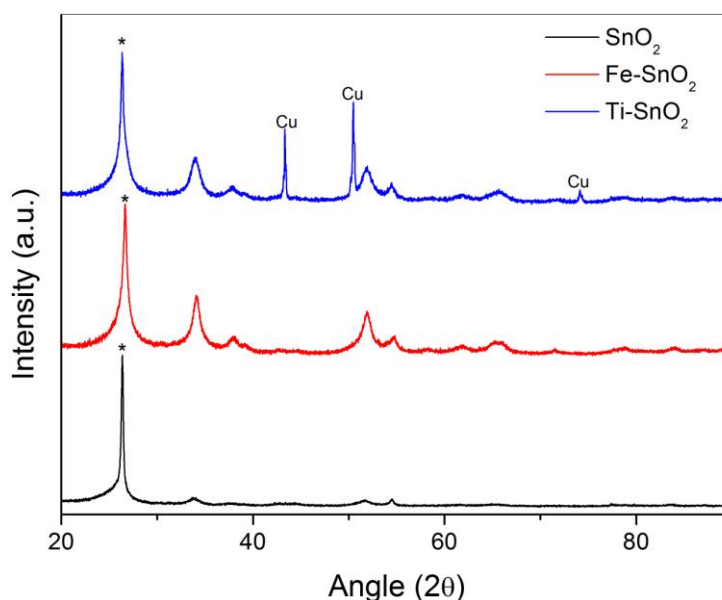


Figure 26. XRD patterns of SnO<sub>2</sub> samples after the electrochemical tests. The label Cu indicates the peaks related to copper nanoparticles coming from the conductive tape. The peaks labeled with the star (\*) have been chosen to calculate the crystals mean dimension.

The dimension variation is particularly evident for SnO<sub>2</sub> (from 5.5 to 39.6 nm) and lighter, but still undeniable, for the doped samples: from 12.3 to 21.3 for Fe-SnO<sub>2</sub> and from 8.0 to 18.6 nm for Ti-SnO<sub>2</sub>. The three peaks present in Ti-SnO<sub>2</sub>

samples post-test are related to copper particles.[51,52] The contribution is due to the exposure of the copper tape, used to contact the sample in the electrochemical cell, to X-rays. It was not possible to remove it without dismembering the samples, thus we decided to limit its contribution by orienting at the best the sample for the measurement.

XRD result are confirmed by the FESEM observation. The porous structure is no more evident, thus confirming the reconstruction of the metal oxide. This would explain the significant change in the selectivity through CO<sub>2</sub> valorisation.

### 3.5 Charge carriers kinetics

In order to better understand the behaviour of doped and un-doped SnO<sub>2</sub> as catalysts, Mott-Schottky and EIS characterization have been performed on the pristine samples. No normalization of the results was needed since the sample loading and the electrodes dimension was kept the same.

EC characterizations are a powerful tool to gain information on charge kinetics, both inside the material as well as at the surface. The major advantage comes from the possibility to study the behaviour of the catalyst in the same environment in which it is tested for CO<sub>2</sub> valorisation.

A particular effort has been devoted in giving a comprehensive description of the electrical behaviour of the samples by separating the capacitive and resistive contribution of both surface and bulk.

EIS measurements help to shed light on the kinetics of electrons diffusion and charge exchange with the adsorbed species. As explained in the Chapter 2, the contributions of bulk and surface can be separated and their resistive and capacitive behaviours modelled using simple circuit elements (Figure 27).

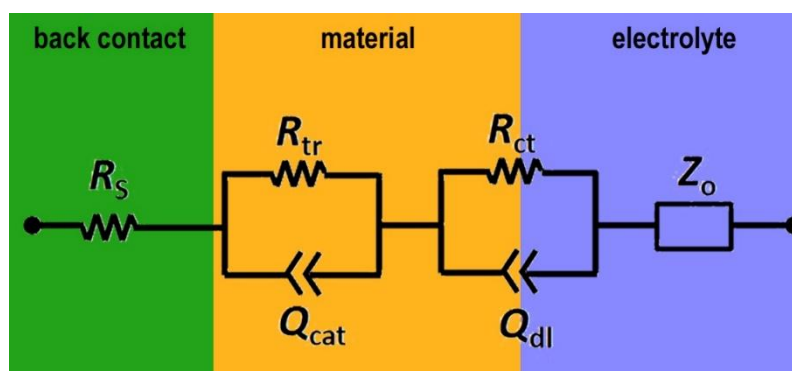


Figure 27. Equivalent circuit chosen to simulate the impedance measurements carried on SnO<sub>2</sub> samples.

The fitting of the Nyquist plot (Figure 61, 62 and 63 in Appendix A) gave as a result the following information on the electrical elements, with an estimated tolerance of 2 %:

- $R_s$ : series resistance lays between 60 and 110 ohm. Since this value does not influence the charge transport at the surface of the catalyst, but it is related to the ohmic phenomena occurring far from the

electrodes, its variability has not been considered in the following discussion. Moreover, the applied potential was found not to influence the value of  $R_s$ , thus demonstrating it depends just on the conductive properties of the electrolyte and the wiring.

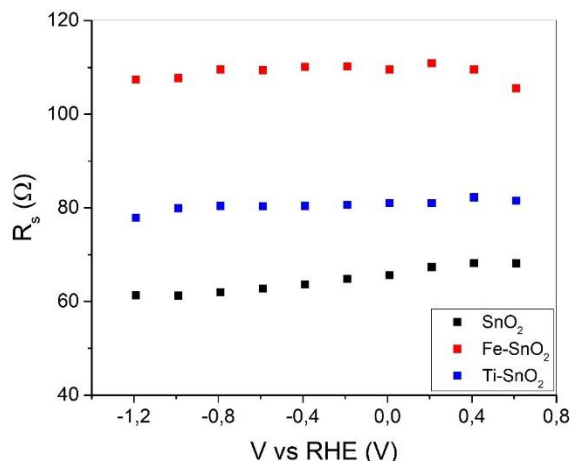


Figure 28. Series resistance ( $R_s$ ) plotted as function of the applied voltage.

- $R_{tr}$ : interestingly, the resistance of the electrons transfer inside the catalyst is not so different between the two doped- $\text{SnO}_2$ , while a consistent reduction, about a half, is observed for the un-doped sample.

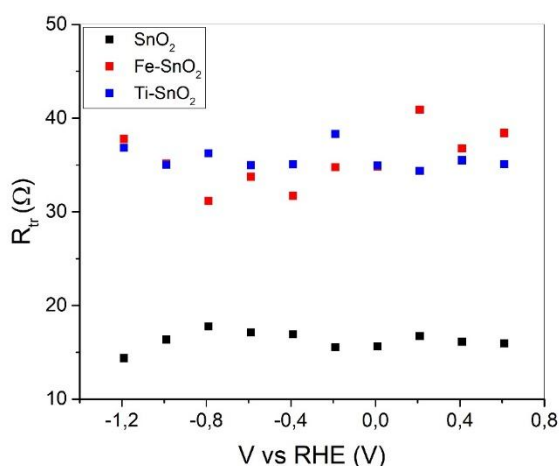


Figure 29. Transport resistance ( $R_{tr}$ ) plotted as function of the applied voltage.

- $Q_{cat}$ : the constant phase element, related to the bulk-material capacitance, has a trend similar to the  $R_{tr}$ , with no differences between the doped samples and a reduction, this time lighter, of the  $Q_{cat}$  of  $\text{SnO}_2$ . It is interesting to notice that the capacity value is quite high, around 1 mF, meaning the material does not favour the charge diffusion in the bulk.

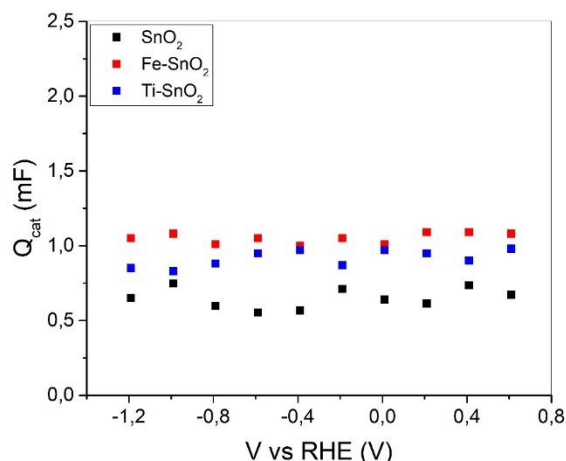


Figure 30. Quasi-capacity of the catalyst ( $Q_{cat}$ ) plotted as function of the applied voltage.

- $R_{ct}$ : by looking at the charge transfer resistance of the surface/electrolyte interface, a low variability is found among the samples. Fe-SnO<sub>2</sub> exhibits the smaller resistance to charge transfer, followed by SnO<sub>2</sub> and Ti-SnO<sub>2</sub>. This trend is in good agreement with the one obtained from the current densities measured during the electrochemical test. It is interesting to notice that at 0.21 V vs RHE there is a slight variation in  $R_{ct}$ . According with the group of Bejtka, [36] this potential is associated with Sn reduction, thus a change on the oxidation state of Sn is expected. This would lead to a different contribution in the conductivity of the sample.

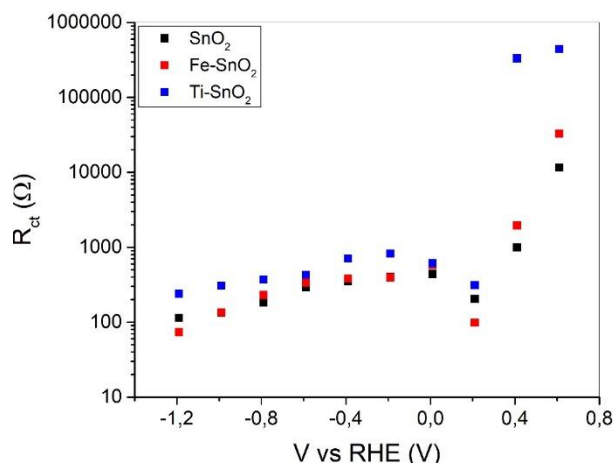


Figure 31. Catalyst resistance ( $R_{ct}$ ) plotted as function of the applied voltage.

- $Q_{dl}$ : the constant phase element of the surface/electrolyte interface is in good agreement with the outcomes presented for  $R_{ct}$ . If we consider the charge transfer time, by multiplying  $Q_{dl}$  per  $R_{ct}$ , it is evident that the presence of Fe plays a key role in doped-SnO<sub>2</sub>, especially through

CO<sub>2</sub> valorisation, by reducing the transfer time about two and eight times with respect to SnO<sub>2</sub> and Ti-SnO<sub>2</sub> respectively.

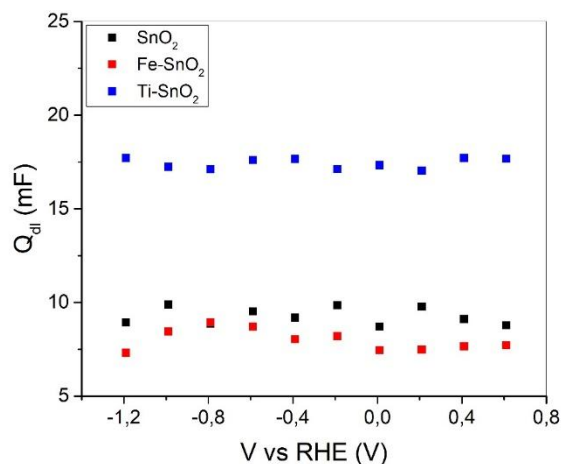


Figure 32. Quasi-capacity of the double layer ( $Q_{dl}$ ) plotted as function of the applied voltage.

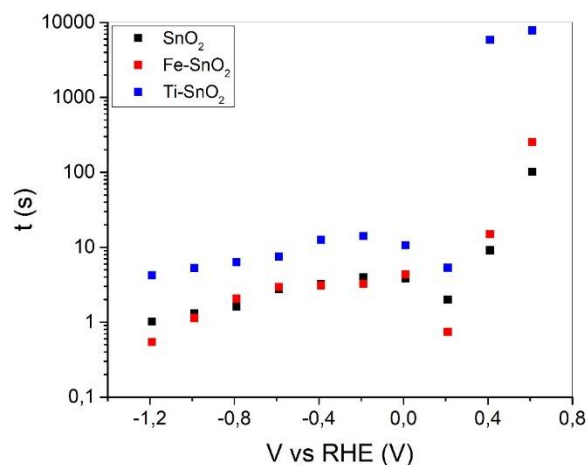


Figure 33. Transfer time ( $t$ ) plotted as function of the applied voltage.

A detailed description of the samples/electrolyte junction comes from the Mott-Schottky measurements. The analysis of the Mott-Schottky plots (Figure 34) displayed a slope variation of one order of magnitude between the doped and undoped samples. In fact, while the slope of SnO<sub>2</sub> is  $(3.5 \pm 0.3) \cdot 10^{-8} \text{ VF}^2$ , Fe-SnO<sub>2</sub> and Ti-SnO<sub>2</sub> have a slope of  $(6.5 \pm 0.2) \cdot 10^{-9} \text{ VF}^2$  and  $(3.0 \pm 0.1) \cdot 10^{-9} \text{ VF}^2$  respectively.

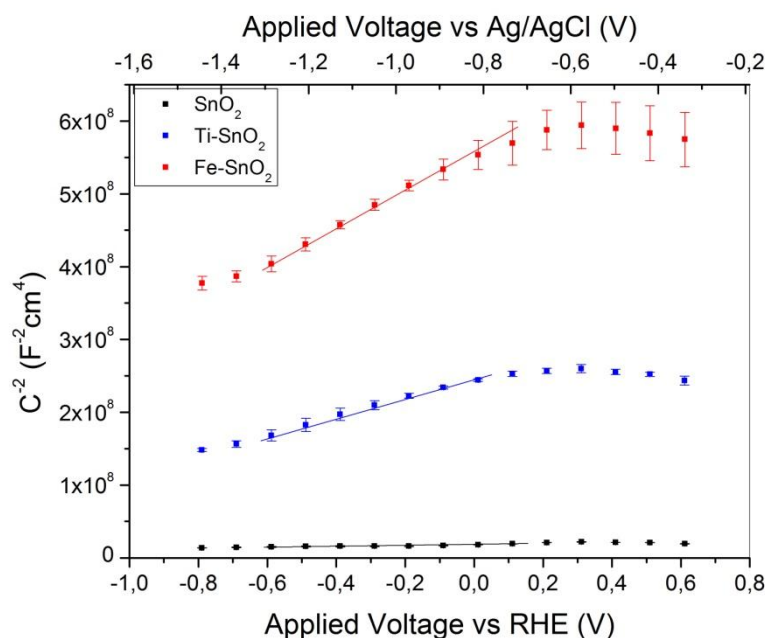


Figure 34. Mott-Schottky plots related to  $SnO_2$  samples. The fitting range is underlined with the continuous line.

A quantitative analysis on the density of states variation is not trivial; however, some qualitative considerations can be done by looking at the results presented until now.

The results coming from HR-XPS of Fe 2p peak (Figure 20 a) demonstrate Fe (III) has been introduced in the  $SnO_2$  matrix, thus inducing a p-doping. For this reason, a decrease of the density of electron-donor would be expected. This would correspond to the enhancement of the slope value of an order of magnitude. However, according with the morphological changes occurred during the doping, and since the slope is inversely proportional to the square of the area, it is possible to argue that the area variation is influencing for the most the slope discrepancy. In fact, as demonstrated by FESEM characterization, the porous structure is strongly modified in doped samples, in particular for  $Fe-SnO_2$ , thus leading to the decrease on the surface area, and so in an increase of the slope value.

### 3.6 Band model reconstruction and interpretation

A schematic representation of the band model can be given by merging the information coming from:

- UV-Vis spectroscopy. Diffuse reflectance measurements have been treated with the modify Kubelka-Munk equation to obtain information on the minimal energy required for electron excitation, as reported in Chapter 2. This gives the distance, in terms of energy, between the VB-top and the CB-bottom;
- VB-top from XPS. Since the major contribution of the DOS of the VB comes from the O 2p orbital, it has been analysed;

- Mott-Schottky EC measurements give information on the flat band potential at the surface/electrolyte interface, and so, on the doping type. Moreover, some considerations on the relative position of the RedOx potential of the electrolyte can be argued.

The solid/electrolyte behaviour has been unravelled by modelling it as a Schottky junction.

When a semiconductor, like the presented catalysts, is immersed in an electrolyte, the electrochemical potential (Fermi level) need to reach the equilibrium with the surrounding environment. Thus, the flow of charge from one phase to the other occurs and a band bending arises within the semiconductor phase.

So, after contact, the net result of equilibration is that  $E_F = E_{F,RedOx}$  and a built in voltage develops in the semiconductor.

As a simple case, if the catalyst is a metal, almost all the potential drop occurs in the Helmholtz region in the electrolyte. If we extend the reasoning to a semiconductor/electrolyte interface, the potential drop is splitted between the semiconductor and the Helmholtz region. In this way, the junction can be simply described by two capacitors in series.

### 3.6.1 Band gap calculation

Diffuse reflectance measurements have been carried on the powder samples, and the data have been treated with the modified Kubelka-Munk equation considering a direct band gap for SnO<sub>2</sub> (Figure 35), in agreement with the findings of Yousif group.[53] The band gap values obtained are  $(3.87 \pm 0.05)$  eV for SnO<sub>2</sub>,  $(3.90 \pm 0.04)$  eV for Fe-SnO<sub>2</sub> and  $(3.96 \pm 0.04)$  eV for Ti-SnO<sub>2</sub>.

The presented values are compatible among each other, thus revealing the doping is not changing the band gap width.

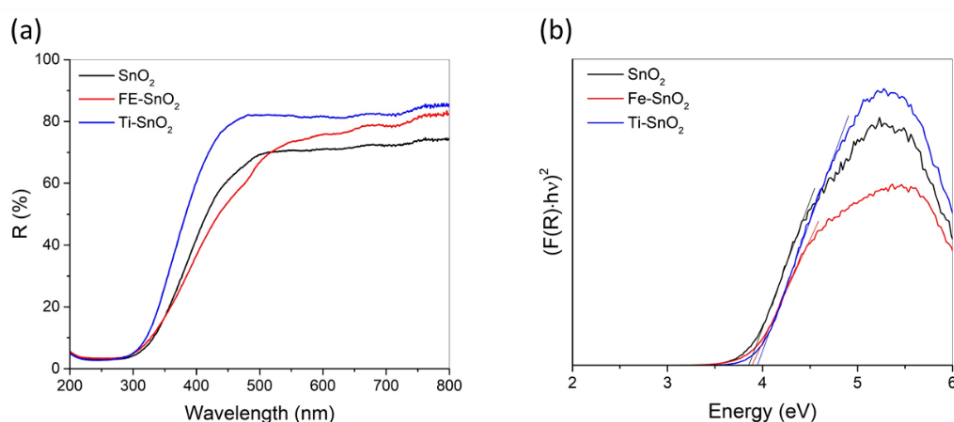


Figure 35. (a) Diffuse reflectance spectra of SnO<sub>2</sub> samples and (b) the function derived from the modified Kubelka-Munk relation.

### 3.6.2 Valence band top definition

By looking at the HR-XPS spectra of the valence band (Figure 36), values of  $(2.40 \pm 0.05)$  eV for  $\text{SnO}_2$ ,  $(2.44 \pm 0.14)$  eV for  $\text{Fe-SnO}_2$  and  $(2.43 \pm 0.03)$  eV for  $\text{Ti-SnO}_2$  have been found. Since the presented values are higher than the half of the band gap, the three samples result to behave as n-type semiconductors, in good agreement with the results coming from the Mott-Schottky measurements.

As expected, Ti-doping does influence the EF position, since  $\text{Sn}^{4+}$  is substituted by the ion  $\text{Ti}^{4+}$ , carrying the same number of valence electrons. A shift would be expected for  $\text{Fe-SnO}_2$  since Fe (III) has been observed in the HR-XPS. Sure enough, the VBtop position of  $\text{Fe-SnO}_2$  is compatible with the presence of a p-dopant, within the associated uncertainty range.

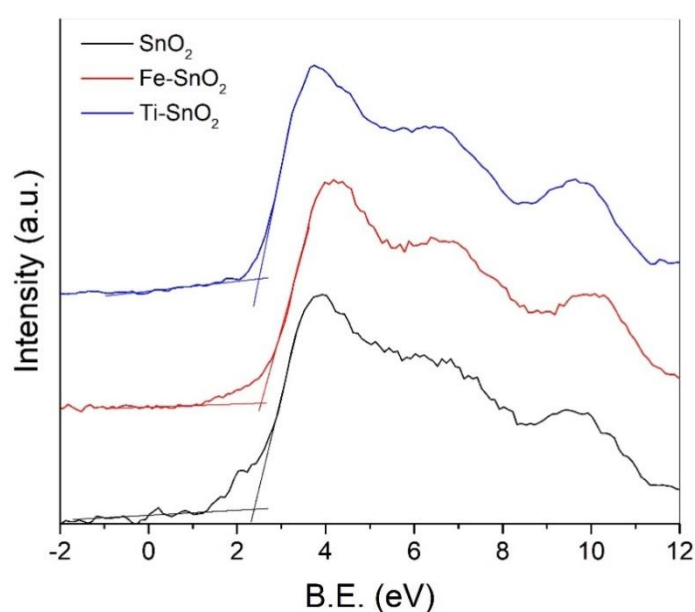


Figure 36. HR-XPS spectra of O 2p orbitals representative of the valence band of  $\text{SnO}_2$  samples.

### 3.6.3 Semiconductor/electrolyte built-in potential

According with the Mott-Schottky measurements, the semiconductive behaviour of  $\text{SnO}_2$  is n-type for both doped and un-doped samples. The flat band potentials, calculated from the fitting parameters, are  $(1.30 \pm 0.10)$  V for  $\text{SnO}_2$ ,  $(2.19 \pm 0.06)$  V for  $\text{Fe-SnO}_2$  and  $(2.04 \pm 0.07)$  V for  $\text{Ti-SnO}_2$ , as shown in Figure 37.

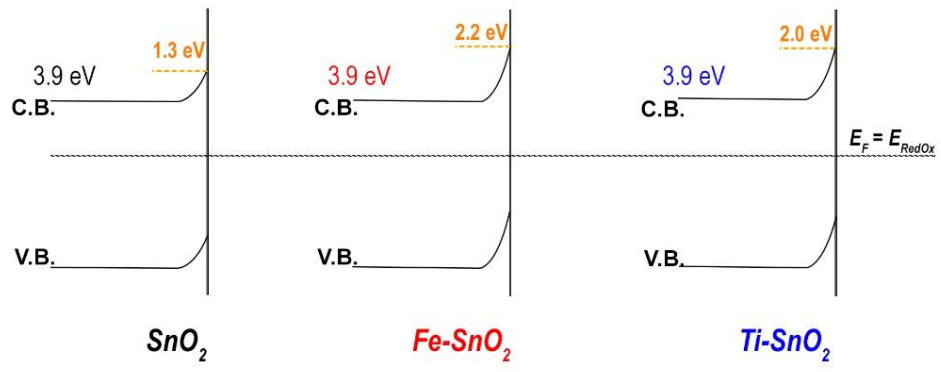


Figure 37. Band scheme of  $\text{SnO}_2$  samples showing the semiconductor/electrolyte interface in equilibrium condition ( $E_F = E_{\text{RedOx}}$ ). In orange the built-in potential values.

# Chapter 4

## Self-doped titanium dioxide

### 4.1 Introduction

Metal oxides have been widely studied and employed in catalysis because they are commonly cheap, easy to produce and scalable. Their properties, together with their natural availability, made them widespread materials both for industrial application and in everyday life.

Titanium dioxide ( $\text{TiO}_2$ ) has become an attractive, sustainable catalyst because of its earth abundance, low toxicity, chemical and thermal stability, and high resistance to photocorrosion.[54] It has been the most widely investigated photocatalyst for various applications since the work on water splitting of Fujishima and Honda.[55] It is present in three allotropic forms: anatase, rutile and brookite. Anatase  $\text{TiO}_2$  has a tetragonal crystal ( $a = 3.7845 \text{ \AA}$ ,  $c = 9.5143 \text{ \AA}$ ) like rutile ( $a = 4.5937 \text{ \AA}$ ,  $c = 2.9587 \text{ \AA}$ ), while brookite has an orthorhombic crystal ( $a = 5.4558 \text{ \AA}$ ,  $b = 9.1819 \text{ \AA}$ ,  $c = 5.1429 \text{ \AA}$ ). They all exhibit a semiconductive behaviour with indirect energy band gap of 3.20 eV (anatase), and direct energy band gap of 2.98 eV (rutile) and 3.26 eV (brookite).[56,57]

The wide band gap limits  $\text{TiO}_2$  employment in visible-light driven photocatalysis, since the intensity of the photons in the UV range of the solar spectrum is lower. The modification of  $\text{TiO}_2$ , through the management of defects, led to the discovery of different structures, such as self doped  $\text{TiO}_2$ ,[54] a form of  $\text{TiO}_2$  with light absorption centred in the visible range. The self-doping can be reached by modifying the oxygen content, thus having two possible stoichiometries:

- sub-stoichiometric  $\text{TiO}_2$ , also known with the name of black  $\text{TiO}_2$ . The synthetic process is based on the removal of surface oxygen atoms by the reductant, the oxygen is released in form of water molecule (for hydrogen reductant) or oxygen molecule (for non-hydrogen reductant). This process results in the formation of surface oxygen

vacancies ( $V_O$ ), thus resulting in the excess electrons that are filling into the empty states of the Ti ions, forming  $Ti^{3+}$  species. This process around one  $V_O$  involves the three nearest-neighbour Ti atoms, which move away from the vacancy toward its five remaining O neighbours. The next-nearest neighbour O atoms move slightly inward due to the absence of electrostatic repulsion by the missing O atom. If the concentration of  $V_O$  is high enough, the excessive reconstruction causes lattice disorder. Thus, the loss of an O atom in a  $TiO_2$  matrix leaves a pair of electrons that could either be both trapped in the cavity to form a neutral  $V_O$ , or interact with adjacent  $Ti^{4+}$  ions to give  $Ti^{3+}$  centres and charged  $V_O^+$  or  $V_O^{2+}$ . These surface  $Ti^{3+}$  centres can interact with absorbed  $O_2$  and  $H_2O$  molecule to give  $O_2^-$  centres and hydroxyl groups.[58–61]

- super oxidized  $TiO_2$ , in which  $O^-$  species, linked to the surface, carry an extra electron that can reduce  $Ti^{4+}$  to  $Ti^{3+}$ , thus inducing a modification on the density of states (DOS). In presence of surface  $-OH$  groups,  $Ti^{4+}$  can act as trapping centre for the electrons, resulting in the formation of  $Ti^{3+}-OH$  species. Moreover, the adsorbed molecular oxygen can perform as electron scavenger to accept an electron becoming the superoxide ion. And the surface  $O_2^-$  or  $O^-$ , resulted from the adsorbed molecular oxygen on the oxygen-defective site in  $TiO_2$ , can serve as the hole trapping centre.[62–64]

The possibility of tuning the energy band gap opened the way to the application of self-doped  $TiO_2$  in various fields of photocatalysis. The major investigated are:

- pollutants degradation,[65,66] like methylene blue removal from industrial waste water. For instance, black  $TiO_2$  nanoparticles demonstrated excellent photocatalytic activities through methylene blue degradation. Within a short time (8 min) [67] they have been able to completely purify water, exploiting a long-term stability too. This performance is much superior to that of white  $TiO_2$ ;
- hydrogen production, [68–70] as sustainable fuel for the future technologies. In this framework, black titania demonstrated the capability to activate hydrogen production without the presence of a co-catalyst (commonly Pt) [71] thus reducing the fabrication costs;
- photo-electrochemical sensors to quantify the organics in an aqueous phase (like glucose, malonic acid and potassium hydrogen phthalate) by measuring the photocurrents originated from the degradation process;[72,73]
- heterostructures for photocatalysis.[74,75] The synergic effect of different structure can improve the  $Ti^{3+}$  stability, extend the visible-light absorption range, increase the adsorption ability for  $O_2$  and pollutants, together with their photodegradation rate;

- photovoltaic, [76,77] like in dye sensitized solar cells, in which defective TiO<sub>2</sub> is used as photoanode, achieving an energy conversion efficiency even 1.5 times higher than stoichiometric TiO<sub>2</sub>:[78]
- fuel generation from CO<sub>2</sub> [54,79] with the selective formation of CO and CH<sub>4</sub> as main products.

Commonly, the synthesis of defective TiO<sub>2</sub> involves the reduction of stoichiometric TiO<sub>2</sub> in different, most of the time extreme, conditions:

- hydrogen treatment [68] at high pressure (up to 40 bar);[80]
- argon annealing;[81,82]
- reduction mediated by metals (like Al, Mg or Zn), organic reductants (like imidazole or ascorbic acid), or with hydrides;[71,83–88]
- hydrogen plasma treatment. [89]

These approaches are based on partial reduction of TiO<sub>2</sub>, incomplete oxidation of low-valence-state Ti species or H-doping, occurring when H<sub>2</sub> is used as reducing agent.

The major drawbacks of the presented processes are the use of toxic chemicals and the need of high temperature and/or pressure. Despite the potentialities as material for environmentally sustainable devices, the synthetic routes up-to-now proposed could not be considered completely sustainable.

First attempts aiming to produce TiO<sub>2</sub> without toxic chemicals, like hydrogen peroxide (H<sub>2</sub>O<sub>2</sub>) [90,91] were proposed by Ayers et al. [92] Titanium oxidation reaction was obtained with water and O<sub>2</sub> as by products, thus with no impacts on the environment. However, the proposed synthesis still requires high-energy conditions:

- long pre-treatments [92] (19 days long);
- high post-annealing temperatures [93] (up to 630 °C);

both leading to multi-step synthesis with high energy consumption and duration;

- high temperature and/or high pressure reaction conditions [79,94–96] run in hydrothermal reactors;
- long time synthesis (up to three days).[97–99]

These processes need to be optimized aiming to minimize the energetic costs impact.

Few attempts to produce super-oxidized TiO<sub>2</sub> with H<sub>2</sub>O<sub>2</sub> demonstrated the possibility to tune the energy gap following this path, however, no one ever tried to merge the synthesis of TiO<sub>2</sub> through H<sub>2</sub>O<sub>2</sub> oxidation with its surface treatment. The main idea is to follow the path:

1. oxidize a titanium foil until a well ordered nanostructure is formed, in order to maximize the exposed surface area, to improve the catalytic performances;
2. interrupt the oxidation process before the  $\text{H}_2\text{O}_2$  is completely consumed, so that it can react with the surface of  $\text{TiO}_2$  creating super-oxidized states, which will change the donor density of the material inducing band modification, and so, the energy gap thickening, as previously described.

Since the formation of a uniform and well-defined nanostructure was the aim of this synthetic path, FESEM has been considered a fundamental technique to select the best synthetic parameters. In this way, it was possible to minimize the duration of the process without wasting heat, and so energy.

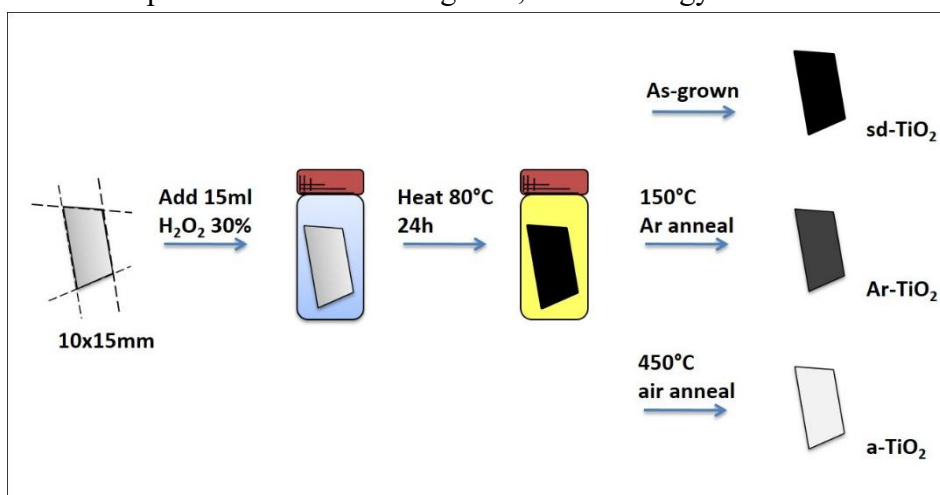


Figure 38. Schematic of the thermal oxidation of Ti foils (on the left) in hydrogen peroxide and their subsequent treatments.

## 4.2 Material synthesis

Commercial Titanium foils (99.7% purity, Sigma-Aldrich, 0.25 mm thickness) were cut into 10x15 mm plates. Prior to the synthesis, the Ti plates were ultrasonically cleaned in acetone (99% purity, Sigma-Aldrich) and, subsequently, in ethanol (99% purity, Sigma-Aldrich) to remove surface contaminations.

Then, the plates were immersed vertically into a vial filled with hydrogen peroxide ( $\text{H}_2\text{O}_2$ , 30%wt, Sigma-Aldrich) and then heated in ambient atmosphere in an oven. Different temperatures (80°C, 65°C, 50°C) and different oxidation times (72 h, 48 h, 24 h) were explored to optimize the synthesis, aiming to obtain a uniform porous structure (Figure 39) stuck on top of the metal foil. Afterwards, the samples were gently washed in deionized water to remove the excess of  $\text{H}_2\text{O}_2$  and dried in ambient air.

The synthetic path has been first proposed by Wu [97], it was meant to consume all  $\text{H}_2\text{O}_2$  to have anatase  $\text{TiO}_2$  as final product, so the parameters were set at 80 °C for 72 h.

At first, we reduced the time to 48 h, and then we scanned three different temperatures: 80 °C, 65 °C and 50 °C, trying to find the minimal heat requirements.

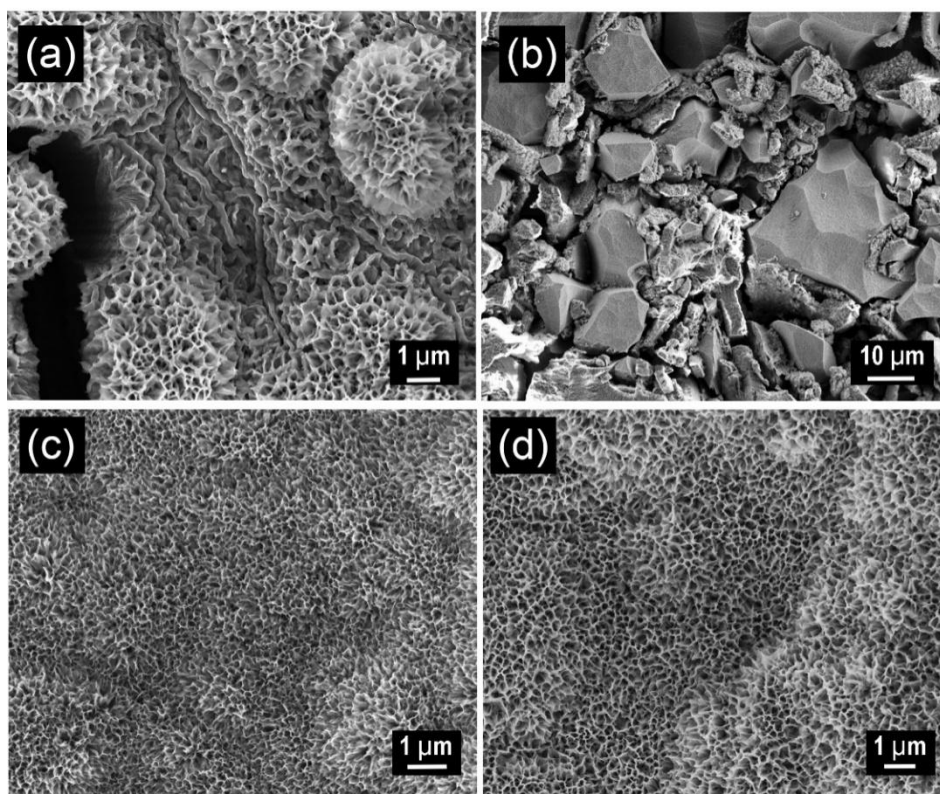


Figure 39. FESEM imaging summarizing the results of the synthesis optimization. The synthesis parameters here adopted are (a) 65 °C for 48 h, (b) 50 °C for 48 h, (c) 80 °C for 72 h and (d) 80 °C for 48 h.

Since 80 °C has been found to be the minimal temperature needed to oxidize the samples in a reasonable amount of time, the synthesis duration was further reduced to 24 h.

The final parameter selected for an extensive sample characterization are 80°C for 24 h.

In order to gain information on the effect of super-oxidized states on the electrical properties of the material, the as-realized samples (sd-TiO<sub>2</sub>) were lastly annealed in Argon atmosphere at 150°C for 2 hours at ambient pressure (Ar-TiO<sub>2</sub>) to completely remove residual H<sub>2</sub>O<sub>2</sub>.

Stoichiometric anatase TiO<sub>2</sub> was also prepared for sake of comparison by alternatively calcinating the as-realized samples in air at 450°C for 1 hour (a-TiO<sub>2</sub>).

All reagents were used as received without any further purification.

### 4.3 Morphological characterization

After annealing in Ar atmosphere, the morphology of the as-synthesized sd-TiO<sub>2</sub> (Figure 40 (a)) retains its honeycomb-like structure (Figure 40 (c)).

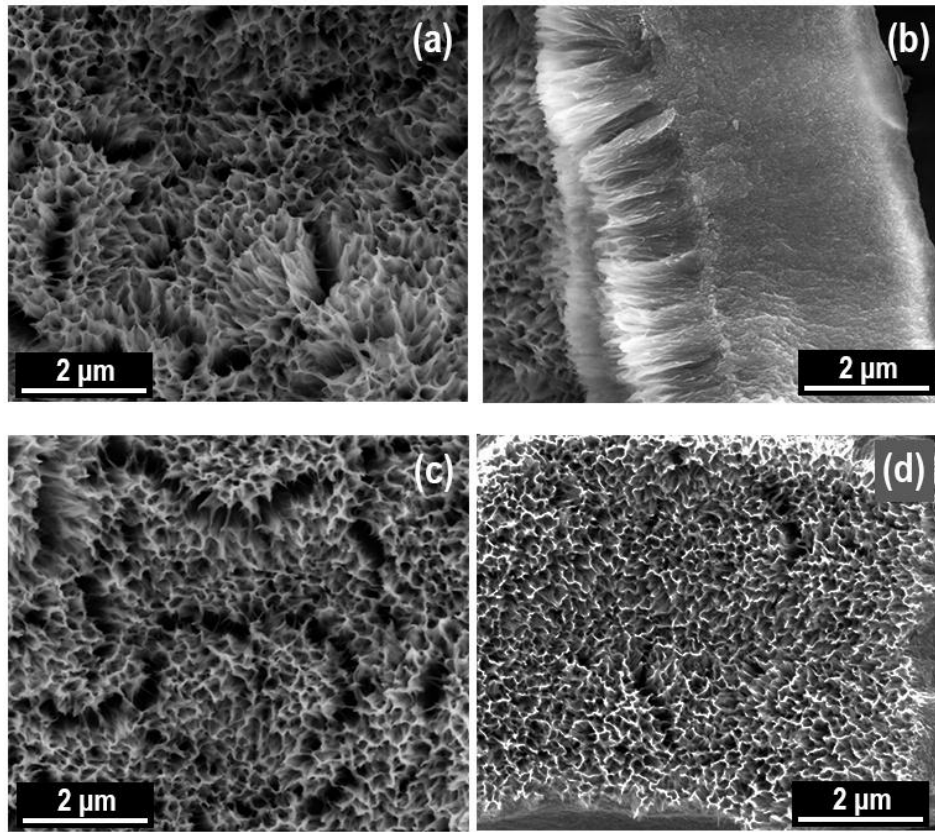
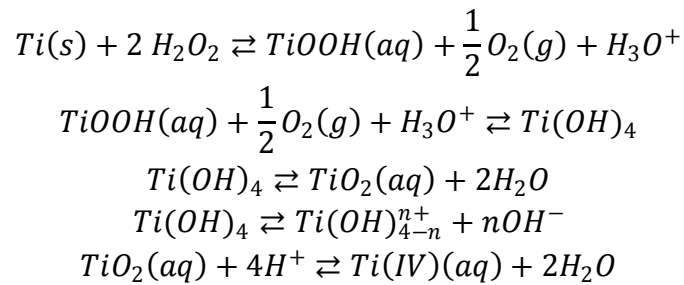


Figure 40. FESEM imaging of the top surface of (a) sd-TiO<sub>2</sub>, (c) Ar-TiO<sub>2</sub>, (d) a-TiO<sub>2</sub> and (b) cross-section of Ar-TiO<sub>2</sub>.

Cross-sectional scanning electron microscopy reveals that this honeycomb-like structure is organized in vertically aligned tubes (Figure 40 (b)). The tubes' length is about 1.7 μm with a pore size around 200–300 nm.

According to Wen et al. [100], we hypothesize that, during the synthesis, titanium is dissolved by H<sub>2</sub>O<sub>2</sub>, which decomposes to molecular oxygen and water while inducing the formation of a titania gel. While evolving, O<sub>2</sub> acts as a templating agent, and aids the growth of a honeycomb-like nanostructure.



The oxidation reaction follows three steps:

1. the oxidation of titanium, preferentially occurring at high density surface defects (like dislocations, vacancies and a large volume fraction of grain boundaries);
2. there, the decomposition of H<sub>2</sub>O<sub>2</sub> generates oxygen molecules (eq. 1st), which can diffuse to form titania gel;

3. the decomposition of  $\text{H}_2\text{O}_2$  to  $\text{O}_2$  and  $\text{H}_2\text{O}$  leads to Ti ion dissolution, which forms more and more pits while the decomposition reaction goes on. The pits then begin to aggregate, thus starting the formation of the previously described nanoporous structure. At the same time, in situ crystallization of the amorphous titania gel occurs.

## 4.4 Structure and surface chemistry

In agreement with the proposed reaction path, the crystalline structure of the final oxide would depend on the duration of the overall process:[98]

- a short time treatment (few minutes long) is expected to create an amorphous oxide;
- a long time treatment (several days) will lead to the crystallization of the amorphous titania gel to the anatase phase of  $\text{TiO}_2$ .

Despite the results presented in literature, the as-grown material does not exhibit a defined crystalline phase. According to GI-XRD patterns and to the TEM results, the material is highly disordered with the evidence of the starting crystallization. This phenomenon becomes more and more evident with the rising of the annealing temperature.

Since the catalysis depends on surface properties, the surface chemistry was investigated with XPS. The in-deep defects study was carried on aiming to discuss the presence and role of:

- oxygen vacancies, which act as hole traps to promote the charge transfer and suppress the recombination of electron–hole pairs, thus enhancing the catalytic activity;[63]
- adsorbed water and the hydroxyl groups. At the surface they can potentially trap holes to form oxidative hydroxyl radicals  $\bullet\text{OH}$  for the photodegradation of organic molecules.[101]

A particular attention has been devoted to the study of the orbital that contributes to the VB-top shape. It has been analysed to gain a direct information about the influence of surface defects on the DOS, and so, on the band gap.

As extensively demonstrated in literature,[54,102] the chemical and structural modification induced on  $\text{TiO}_2$  can reduce the band gap by modifying the VB-top (dominated by O 2p orbital) and CB-bottom (dominated by Ti 3d orbital) introducing a tailing in the DOS. The interpretation of this tailing is still under debates, but the authors converge in two main interpretations:

- surface disordered structures cause both VB and CB tails, especially in hydrogenated  $\text{TiO}_2$ . Density Functional Theory (DFT) and Perdew–Burke–Ernzerhof (PBE) calculations support this interpretation,[103] suggesting that the O-sublattice distortion is responsible of VB-top blue-shift (not changing the CB-bottom), while

Ti-sublattice distortion introduces both VB-top blue-shift and CB-bottom redshift;

- the introduction of hydroxyls groups in amorphous  $\text{TiO}_2$  induces band gap narrowing by tailing both VB and CB.[65]

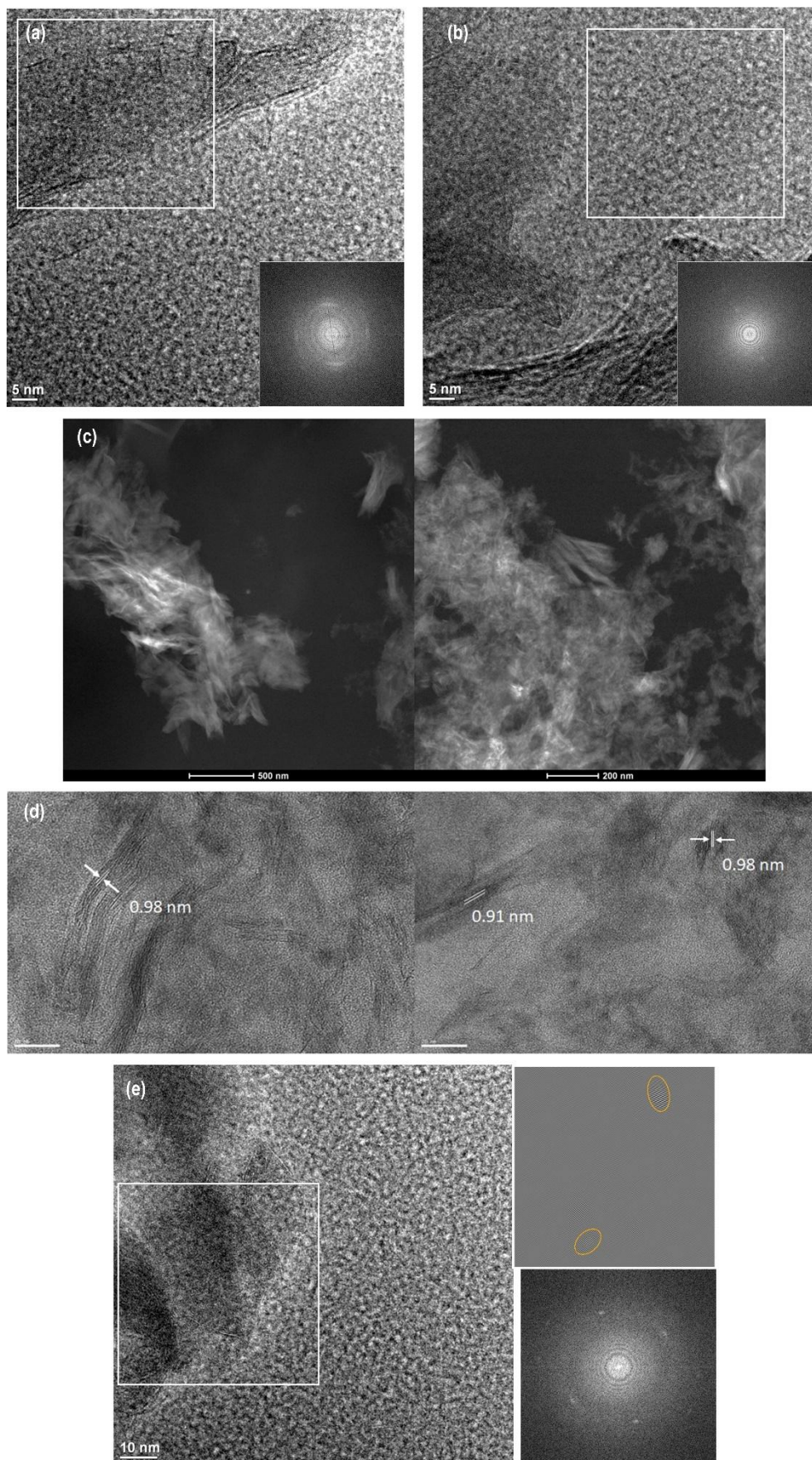


**Figure 41. (a, b) TEM imaging of sd-TiO<sub>2</sub>, with FFT in the inset, (c, d) STEM and TEM imaging of Ar-TiO<sub>2</sub>, (e) TEM imaging of Ar-TiO<sub>2</sub> with FFT (bottom-right) and inverse FFT (top-right) associated to the white-squared region.**

From the TEM characterization (Figure 41), sd-TiO<sub>2</sub> shows a disordered, amorphous-like, structure with some layered clusters with spacing between 0.9 and 1.1 nm. They do not correspond to any graphitic-like or titanium-based compound. In the insets of Figure 41 (a) and (b) the Fast Fourier Transform (FFT) shows some small crystalline domains are present with a structure compatible with (101) of anatase ( $d = 0.355$  nm – JCPDS 21-1272).

The crystalline structure was further investigated by GI-XRD (Figure 42).

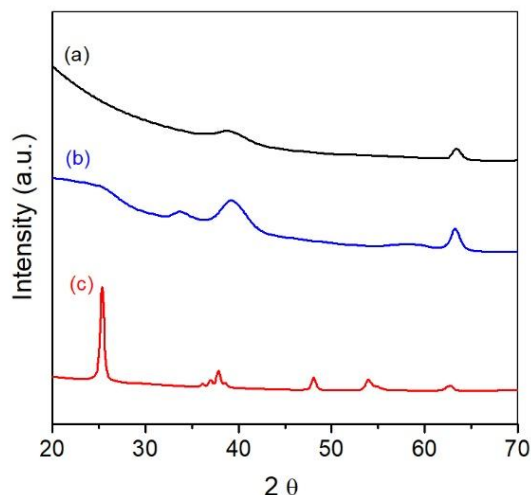


Figure 42. GI-XRD carried on (a) sd-TiO<sub>2</sub>, (b) Ar-TiO<sub>2</sub> and (c) a-TiO<sub>2</sub>.

The GI mode indicated the presence of a large shoulder at low  $2\theta$  angles, thus suggesting that the sd-TiO<sub>2</sub> is amorphous, with no evidence of any crystalline phase of TiO<sub>2</sub> (anatase, rutile, brookite).

The samples annealed at 150 °C in Ar (Ar-TiO<sub>2</sub>) exhibit a flake-like behaviour, as shown in the STEM image of Figure 41 (c) and as already pointed out in the FESEM characterization (Figure 40). In Figure 41 (d) these layered clusters appear more evident, with the spacing ranging between 0.9 and 1.0 nm. The FFT (Figure 41 (e)) of the white squared region shows some spots. In the same picture, the FFT inverse of the spots (DigitalMicrograph tool) shows three reconstructed crystals whose spacing is in the range 0.33–0.36 nm, compatible with (101) of anatase.

From FESEM and TEM, it turns out that this material does not exhibit a morphological or structural characteristics of any other self-doped TiO<sub>2</sub> obtained through the reduction of the crystalline starting material.

On the other hand, the diffraction pattern obtained from GI-XRD investigation (Figure 42) on a-TiO<sub>2</sub> is in good agreement with the anatase pattern (JCPDS 21-1272).

The surface chemical composition of TiO<sub>2</sub> samples was investigated with XPS, using C 1s peak (284.8 eV) to calibrate the spectra.

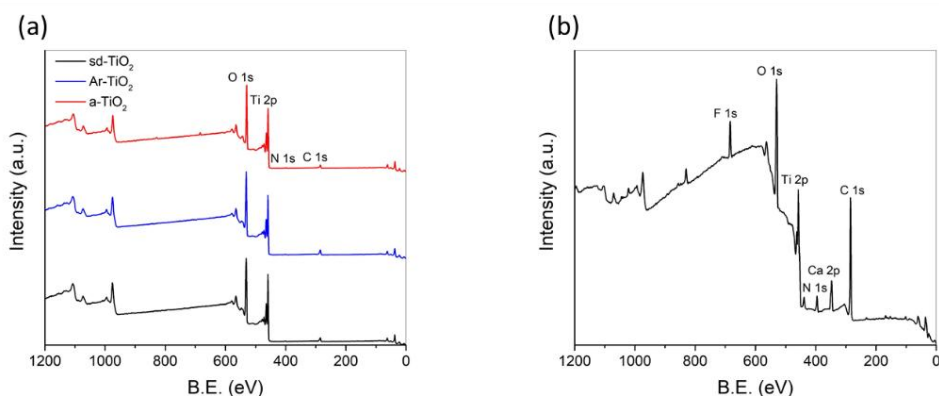


**Figure 43.** XPS survey spectra of (a) self-doped TiO<sub>2</sub> samples and (b) pristine Ti foil. The peaks are labeled with the corresponding orbital name.

The related survey spectra are reported in Figure 43, where Ti and O are observed, with small traces of adventitious carbon, nitrogen and fluorine coming from the pristine Ti foil. As confirmed by a previous study,[104] N and F are not incorporated during the synthesis process. However, their traces amounts could still impact the properties of the synthesized material. For example, fluorination of TiO<sub>2</sub> can lead to binding energy shift towards lower energies in the Ti 2p and O 1s spectrum compared to unmodified TiO<sub>2</sub>,[105] not observed in our samples. Furthermore, the presence of F can increase hydroxyl adsorption, which can be beneficial for surface defect engineering, as previously explained. On the other side, N-doping, may lead to changes in the electron paramagnetic resonance spectra.[106] They are characterized by two resonance peaks related to O<sub>2</sub><sup>-</sup> and NO<sub>2</sub><sup>-</sup>, with reduced intensity indicating reduced Ti<sup>3+</sup> concentration.

The high resolution O 1s and Ti 2p spectra are shown in Figure 44 (a) and (b) respectively.

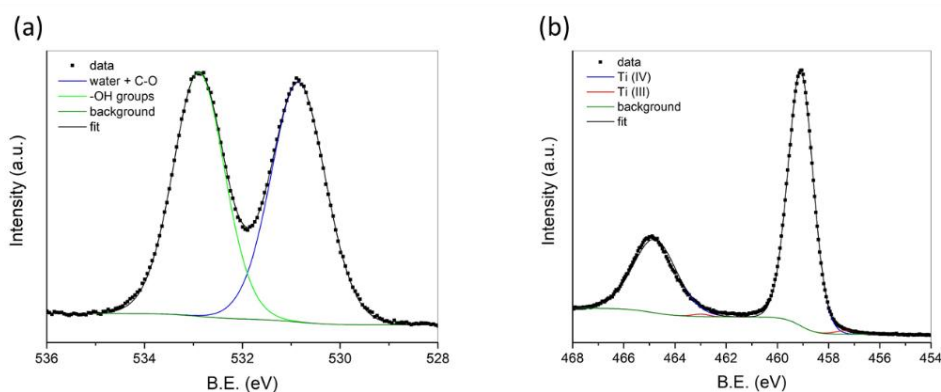


**Figure 44.** HR-XPS of (a) O 1s and (b) Ti 2p peaks of sd-TiO<sub>2</sub>.

The Ti 2p spectrum of the as-grown films reveals a characteristic doublet peak with binding energies of 459.1 eV and 464.8 eV arising from Ti 2p<sub>3/2</sub> and Ti 2p<sub>1/2</sub> states, respectively. The spin-orbit split between Ti 2p<sub>3/2</sub> and Ti 2p<sub>1/2</sub> has a binding energy difference of 5.7 eV, characteristic of Ti (IV). The observed doublet is characteristic of the presence of Ti<sup>4+</sup> states which is in agreement with studies on hydrogen peroxide treated TiO<sub>2</sub>. [107,108] Additionally, indications of

the presence of a small doublet at 457.3 eV and 463.0 eV are discernible in the Ti 2p spectrum pointing towards the formation of lower oxidation states. The corresponding binding energies are in agreement with literature assigning the peak e.g. to either  $\text{Ti}^{3+}$  [109] states or  $\text{TiOH}$ . [110,111]

Additional information on the surface composition can be gained from the O 1s spectrum. The O 1s spectrum of the as-grown material (black line) exhibits a peak with two components centered at binding energies: 531.0 eV and 532.9 eV. The first peak at about 531.0 eV is located at the lower end of the binding energy range, and it is typically assigned to the presence of hydroxyl group such as physisorbed  $\text{H}_2\text{O}$ . The binding energy of the second peak at 532.9 eV could support the presence of chemisorbed  $\text{H}_2\text{O}$  on the surface i.e.  $\text{Ti-OH}$  [112], as well as of the generation of peroxide on the surface due to the  $\text{H}_2\text{O}_2$  treatment. [107,113] Notably, the presence of residuals  $\text{H}_2\text{O}_2$  and hydroxyl groups on the surface of as-grown samples is in agreement with the absence of a crystalline structure revealed by GI-XRD.

According with these results, the electron coming from the  $\text{O}^-$  species is the responsible of surface reduction, and so on the change in the donor density.

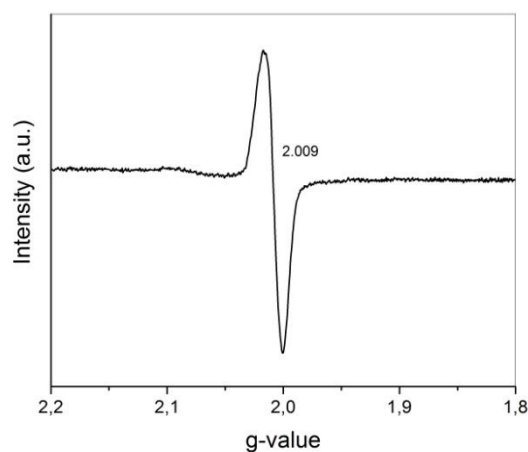


**Figure 45.** EPR spectrum of  $\text{sd-TiO}_2$ .

In order to provide insights into the nature of defects present in the as-grown samples, we carried out electron paramagnetic resonance spectroscopy at room temperature to examine the paramagnetic species. The corresponding EPR spectrum (Figure 45) of the as-grown sample shows a sharp, dominant signal at a g-value of 2.009. This feature is assigned to surface oxygen radical species, in fact the oxygen interaction with  $\text{Ti}^{3+}$  is believed to form  $\text{O}^-$  species at the surface. This hypothesis is in good agreement with literature, in which surface  $\text{O}^-$  species are believed to be generated from the interaction of  $\text{O}_2$  with the surface  $\text{Ti}^{3+}$  species, associated with surface oxygen vacancies. [114–116]

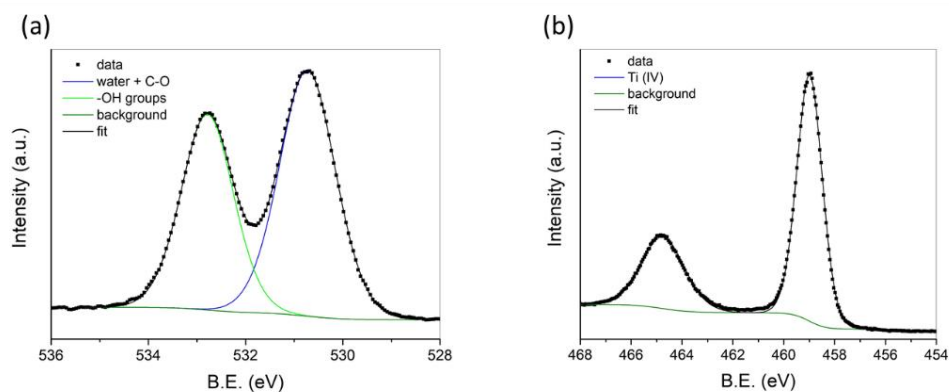


**Figure 46. HR-XPS of (a) O 1s and (b) Ti 2p peaks of Ar-TiO<sub>2</sub>.**

As regard the Ar-TiO<sub>2</sub> (Figure 46), the annealing process suppressed the component of O1s located at 532.8 eV, thus demonstrating the removal of H<sub>2</sub>O<sub>2</sub> moves the equilibrium of the reaction toward the formation of more oxidized species. In other words, chemisorbed H<sub>2</sub>O<sub>2</sub> reacts forming H<sub>2</sub>O that is retained on the surface (as shown in the oxidation mechanism) through physical interaction (Van der Waals), as demonstrated by the strong peak present at 530.7 eV. Interestingly, the O 1s shifts at lower binding energy with the reduction of the H<sub>2</sub>O<sub>2</sub> contribution.

A similar behaviour was observed in Ti 2p peaks. The doublet maintain a gap of 5.7 eV among the components of the spin-orbit peaks, which is again characteristic of Ti (IV) presence. Even though, the shift at lower binding energy is less pronounced.

The Ti (III) component was no more observed, leading to the conclusion that the peroxide treatment is dominating the formation of these reduced species at the surface.

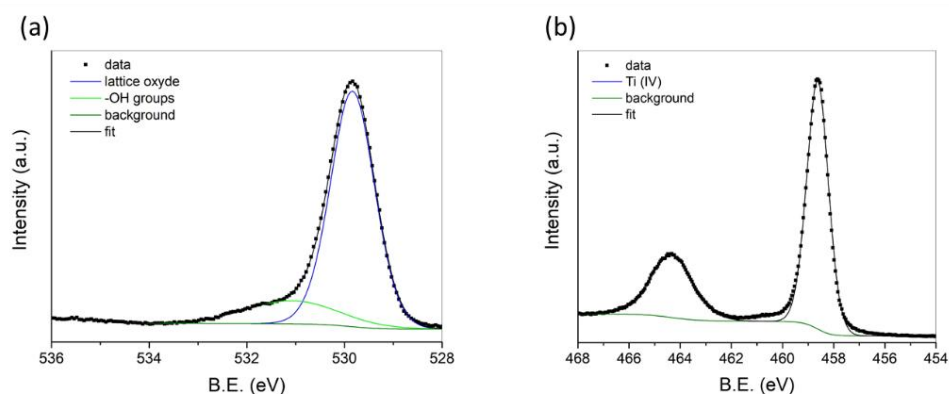


**Figure 47. HR-XPS of (a) O 1s and (b) Ti 2p peaks of a-TiO<sub>2</sub>.**

As a final result, it has been observed that the peaks in the Ti 2p and O 1s spectrum (Figure 47) of the air annealed samples are shifted towards lower binding energies relative to the as-grown material, which could arise from changes in the chemical environment during annealing. Specifically, annealing at 450 °C in ambient air could lead to changes in the surface composition caused by removing residual H<sub>2</sub>O<sub>2</sub> from the surface. This hypothesis is confirmed by the

absence of the O 1s peak at around 533 eV after annealing. Furthermore, the peak at 529.8 eV starts appearing, indicating the formation of  $\text{Ti}^{4+}\text{-O}$  during annealing. This demonstrates that a strong oxidizing environment, together with  $\text{H}_2\text{O}$  removal at high temperature, can push the formation of stoichiometric  $\text{TiO}_2$ . Overall, the O/Ti ratio can be determined from the Ti 2p and the O 1s spectrum to 0.5, which is in agreement with the stoichiometric composition of  $\text{TiO}_2$ . In agreement with XRD measurements discussed above, we can assign the air annealed sample at 450 °C to anatase  $\text{TiO}_2$ .

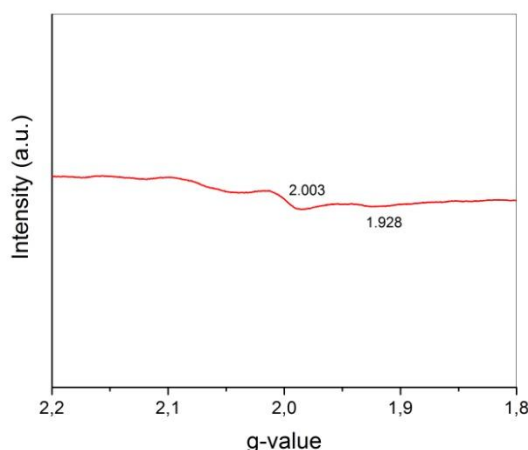


**Figure 48.** EPR spectrum of a- $\text{TiO}_2$ .

As regard the EPR characterization (Figure 48), while the component at  $g = 2.009$  is significantly reduced in the air annealed sample, with respect to the as grown, it is possible to observe two weak features at  $g = 2.003$ , which can be attributed to the presence of oxygen vacancies, and at  $g = 1.928$ , which is usually attributed to  $\text{Ti}^{3+}$ . More specifically,  $g$ -values between 2.001 and 2.004 are typically assigned to electrons trapped in oxygen vacancies, whereas  $\text{Ti}^{3+}$  states are attributed to  $g$ -values of around 1.94.[117–120]

## 4.5 $\text{CO}_2$ valorisation tests

Several works demonstrated the capability of oxygen vacancies to reduce  $\text{CO}_2$ . [79,121–130]

Thanks to its electronic properties and geometry,  $\text{CO}_2$  molecule is highly stable. The C=O double bond has the highest dissociation energy ( $750 \text{ kJ mol}^{-1}$ ) if compared with other types of C-bond, like C–H and C–C bonds. [131] Therefore, the acceptance of a photo-generated electron by  $\text{CO}_2$  (so-called activation process) has to occur before the reduction takes place. Interestingly,  $\text{CO}_2$  adsorption on  $\text{TiO}_2$  surface defects is considered itself as an activating process.

According with literature, oxygen vacancies demonstrated to be effective adsorption sites for  $\text{CO}_2$ . Some studies unveiled that the dissociation of  $\text{H}_2\text{O}$  into OH groups also participate to the adsorption process. Theoretical calculations also

demonstrated that point defects help to stabilize surface  $\text{CO}_2^-$ , which is believed to be the intermediate for CO formation.[130]

$\text{CO}_2$  photoreduction, in presence of water, is described in the two following steps [132]:

1. at first,  $\text{CO}_2$  and  $\text{H}_2\text{O}$  molecules are adsorbed at the surface. For this purpose, high surface area and low physical and chemical energy barriers are required;
2. then, the absorption of a photon starts the photocatalytic process. In detail:
  - a. photon absorption at the surface generates electron-holes pairs;
  - b. the excited electrons in the conduction band start migrating to the surface where the reduction of  $\text{CO}_2$  can take place. Since the reaction begin from a photon generated by the Sun, the products of  $\text{CO}_2$  valorisation are called solar fuels (e.g., CO,  $\text{CH}_4$ ,  $\text{CH}_3\text{OH}$ ,  $\text{HCOOH}$ );

the holes left in the valence band can participate to the catalytic process oxidizing water into oxygen.

According with the previous statements, presence of surface defects increases the productivity of  $\text{CO}_2$  photocatalytic conversion thanks to:

- the enhanced adsorption of  $\text{CO}_2$  at the defect sites;
- the enhanced light absorption, resulted from the defect-assisted band structure modification (discussed in the Introduction section of this Chapter);
- the enhanced charge separation.

Moreover, the presence of defects alters the band position, respect to a standard material (defect-free), leading to a different selectivity through products.

The local electron-density plays an important role too, since the selectivity depends also on the number of electrons required for a specific reduction process, e.g. two electrons are needed to form CO, while  $\text{CH}_4$  formation requires eight electrons.

The materials were tested in the photo-electrochemical reactor described in the previous chapter (Chap. 2). The PEC tests on the as-grown sample were not carried on because the nanostructure started detaching when biased with a potential more negative than -0.44 V vs RHE, therefore we consider the sample was not able to drive any cathodic reduction reaction.

We assumed the electrons coming from the cathode may reduce the  $\text{H}_2\text{O}_2$  left on the surface, causing a second, faster, oxidation process that increased the strain between the metal substrate and the existing surface-oxide, thus causing the detachment.

On the other hand, the PEC tests on Ar- $\text{TiO}_2$  displayed that the reduction of  $\text{CO}_2$  to CO started at -0.54 V vs RHE. By moving to more negative potentials, the

mass diffusion limits led to the formation of H<sub>2</sub> as main product, with a mean Faradaic efficiency of 96.5%.

Sharp and well defined peaks, corresponding to CO and CH<sub>4</sub>, were detected too. The Faradaic efficiency for CO and CH<sub>4</sub> were calculated: 0.17 % (12.2 ppm) and 0.05 % (0.87 ppm) respectively.

Even if the quantity of CH<sub>4</sub> monitored by the GC is close to its detection limit, after 30 minutes of gas-sampling, the corresponding peak remained constant in area and position. Therefore, the results are considered reliable and will be presented in the following comparison with the performance of a-TiO<sub>2</sub>.

No significant differences have been found in the current density values between light and dark condition. This result was expected for a-TiO<sub>2</sub>, since its wide band gap does not fit with the emission spectrum of the sun-simulator lamp (Figure 49).

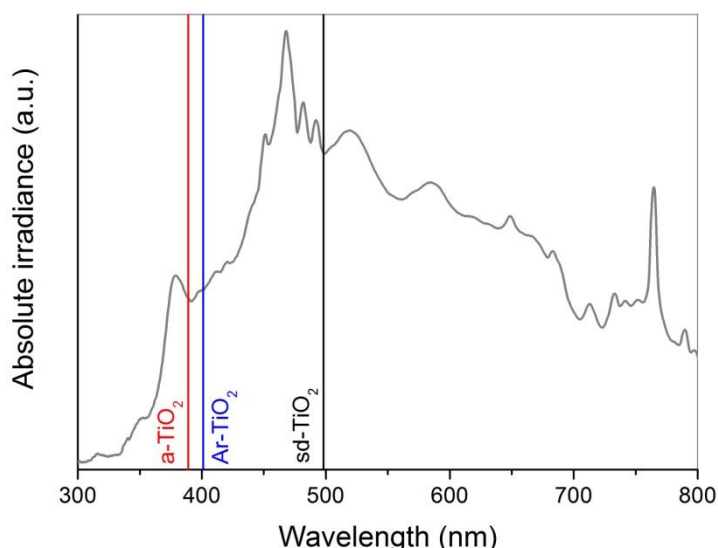


Figure 49. Emission spectrum of the solar-simulator lamp with TiO<sub>2</sub> samples absorption position indicated with colored vertical lines.

On the other hand, the lack of a measurable photocurrent in Ar-TiO<sub>2</sub> was associated with the absence of Ti(III) states, as observed from Ti 2p components in HR-XPS. A deeper investigation will be presented and discussed in the next section.

The recombination of the photo-generated charges has been considered as a possible reason of the absence of a photocurrent. While surface oxygen vacancies serve as electron traps, which can facilitate the reduction reaction, depending on the energy levels and spatial distributions they could play the role of charge recombination centres.[133,134]

Table 2. Photo-electrochemical results of CO<sub>2</sub> valorisation tests on Ar-TiO<sub>2</sub> and a-TiO<sub>2</sub>.

		<i>Ar-TiO<sub>2</sub></i>		<i>a-TiO<sub>2</sub></i>	
		<b>Dark</b>	<b>Light</b>	<b>Dark</b>	<b>Light</b>
<i>Average</i>	<i>current</i>	4.77 ± 0.04	4.8 ± 0.1	24.5 ± 0.7	20 ± 1

density ( $\text{mA}/\text{cm}^2$ )				
<b>Faradaic Efficiency results</b>				
Total (%)	$96 \pm 1$	$97.4 \pm 0.4$	$97 \pm 1$	$96 \pm 1$
CO (%)	$0.170 \pm 0.003$	$0.163 \pm 0.004$	$0.016 \pm 0.001$	$0.023 \pm 0.004$
CH <sub>4</sub> (%)	$0.050 \pm 0.003$	$0.044 \pm 0.006$	--	--
H <sub>2</sub> (%)	$96 \pm 1$	$97.2 \pm 0.4$	$97 \pm 1$	$96 \pm 1$

As regard a-TiO<sub>2</sub>, no CH<sub>4</sub> has been measured. Moreover, it has been observed that the quantity of CO (expressed in ppm) in a-TiO<sub>2</sub> is a half of the produced by Ar-TiO<sub>2</sub>, even if the current densities are about five times higher. This result highlights the fundamental role of surface defects in CO<sub>2</sub> valorisation.

The dominant H<sub>2</sub> production has been associated with the n-type behaviour of TiO<sub>2</sub>. Because of that, an upward band bending is expected at the catalyst/electrolyte interface at the equilibrium. Therefore, a high over-potential is required to compensate the surface bending, letting the electron diffuse to the surface to start the reduction reaction.

No liquid products have been found for any of the tested samples.

## 4.6 Charge carriers kinetics

The interpretation of the semiconductor/electrolyte interface has been studied with impedentiometric measurements.

The calculations are based on the consideration done for SnO<sub>2</sub>. Briefly, the semiconductor/electrolyte system has been modelled as a series of capacitance, dominated by the contribution coming from the material itself. In this way, the Mott-Schottky plot can be used to gain information on the charge density and on the built in potential established when the Fermi level of self-doped TiO<sub>2</sub> is aligned with the RedOx potential of the electrolyte.

Detailed information on the charge transfer kinetic have been extracted from the EIS measurements, using the equivalent circuit model shown in Figure 50. No normalization of the results was needed since the sample loading and the electrodes dimension were kept the same.

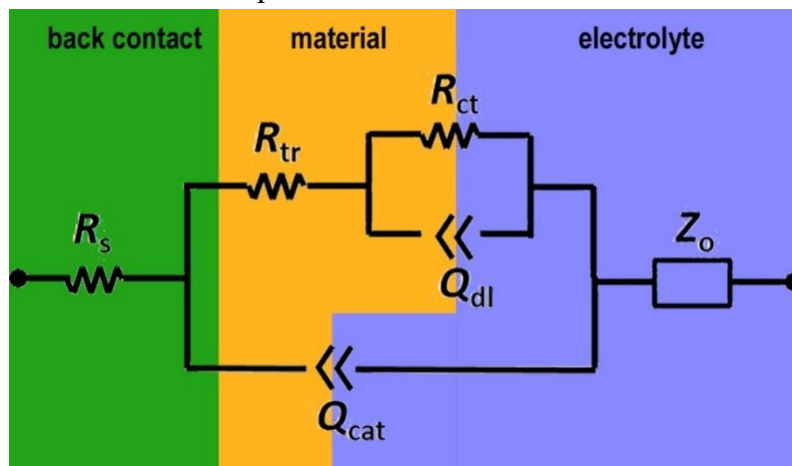


Figure 50. Equivalent circuit chosen to simulate the impedance measurements carried on TiO<sub>2</sub> samples.

The comprehensive description of the electrical elements was presented in the previous chapters.

By looking at the Mott-Schottky plots (Figure 51), it emerges that both a-TiO<sub>2</sub> and self-doped TiO<sub>2</sub> behave as n-type semiconductors, as expected, since the major charge carriers are electrons.

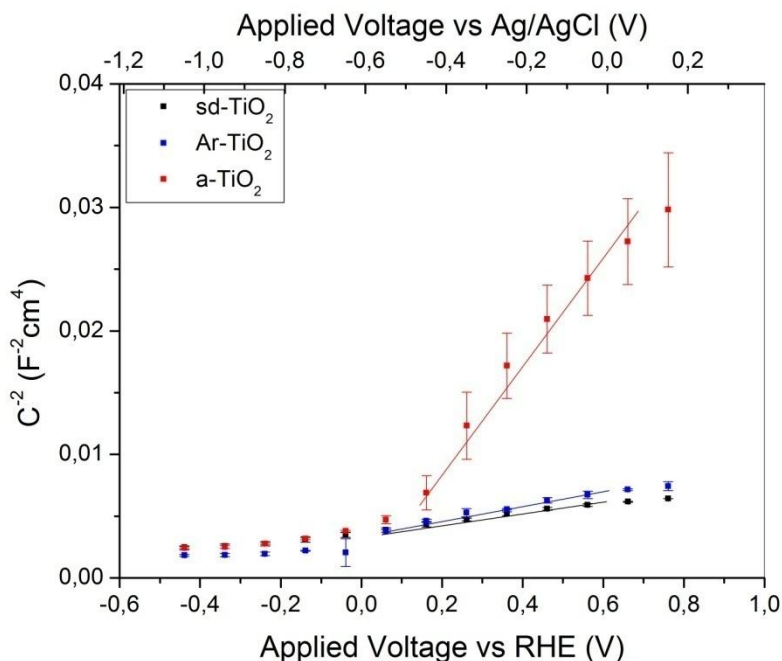


Figure 51. Mott-Schottky plots related to TiO<sub>2</sub> samples. The fitting range is underlined with the continuous line.

Some consideration on the donor density can be argued, by imposing a single constrain. Since the morphology of the different samples is the same, as observed in the FESEM imaging (Figure 40), we assume the surface area is the same among the all samples. From the analysis of the Mott-Schottky plots, a qualitative analysis of the slopes is proposed to obtain an indication of the donor density  $N_D$ . The slope values of sd-TiO<sub>2</sub> and Ar-TiO<sub>2</sub> are about ten times lower than the one of a-TiO<sub>2</sub>. As stated in the Mott-Schottky model (Chapter 2), the slope value depends only on the dielectric constants and on the donor densities. Indeed, the dielectric constant value of anatase TiO<sub>2</sub> and self-doped TiO<sub>2</sub> are in similar ranges: around 40 for anatase (48 for powders and 40 for thin films [135]) and from 86 to 170 [83,136] for self-doped TiO<sub>2</sub>. For this reason, we can conclude that the discrepancy of one order of magnitude among the slopes has to be attributed to the different values of  $N_D$ . The charge-carrier density enhancement observed in self-doped TiO<sub>2</sub> corresponds to improved electronic conductivity and thus a better electron-hole pair separation and transport within the electrode is expected. Moreover, the upward shift of Fermi level, caused by higher donor density, could further facilitate the charge-transfer kinetics at the electrode/electrolyte interface. These results are in good agreement with the findings of Mao et al. [87] related to B-TiO<sub>2</sub> films prepared via hydrothermal synthesis.

Major information was extracted from EIS measurements. By looking in detail at the elements of the equivalent circuit, extracted from the Nyquist plot fitting (Figure 64, 65 and 66 in Appendix A) with an estimated tolerance of 2 %, it turns out that:

- $R_s$ : the series resistance lays around 9 ohm. As expected, the value is not influenced neither by the nature of sample under test, nor by the applied potential, since it depends just on the conductive properties of the electrolyte and the wiring.

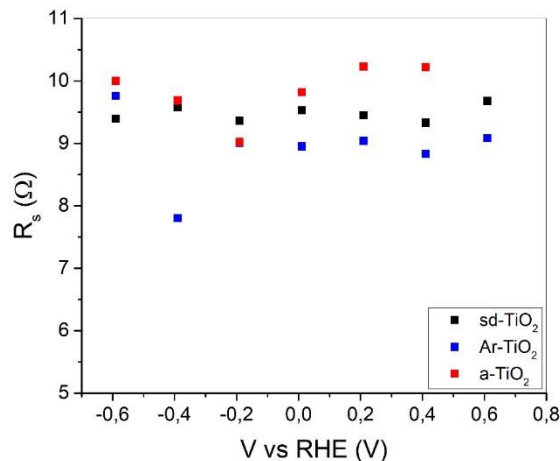


Figure 52. Series resistance ( $R_s$ ) plotted as function of the applied voltage.

- $R_{tr}$ : interestingly, the resistance to the electrons transfer inside the catalyst is not so different between Ar-TiO<sub>2</sub> and a-TiO<sub>2</sub>, while a slight reduction is observed for sd-TiO<sub>2</sub>. This observation is consistent with the findings of Li's and Cui's groups [72,137] who attributed the excellent electric conductivity of self-doped TiO<sub>2</sub> to the high concentration of Ti<sup>3+</sup>.

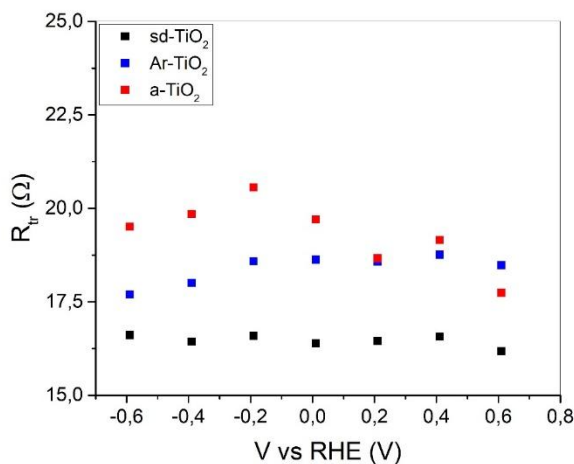


Figure 53. Transport resistance ( $R_{tr}$ ) plotted as function of the applied voltage.

- $Q_{cat}$ : also the constant phase element related to the bulk-material capacitance does not display significant changes among the samples, thus making us consider the defect engineering affects the surface capacitive properties at the most.

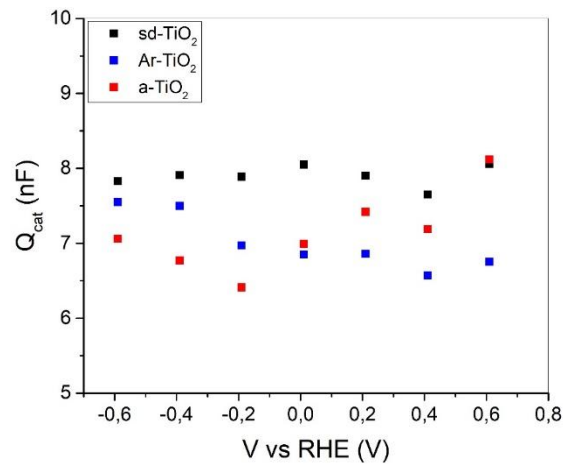


Figure 54. Quasi-capacity of the catalyst ( $Q_{cat}$ ) plotted as function of the applied voltage.

- $R_{ct}$ : the charge transfer resistance at the surface/electrolyte interface is the most informative to establish which material exhibits the best catalytic properties. While no significant differences have been observed between Ar-TiO<sub>2</sub> and sd-TiO<sub>2</sub>, the annealing at 450 °C reduces the conductivity of TiO<sub>2</sub>, thus increasing the resistance to electron transfer to the adsorbed species at the surface. These results are in agreement with the outcomes of the CO<sub>2</sub> valorisation tests, in fact, defective structures demonstrates to be more active for CO<sub>2</sub> reduction.

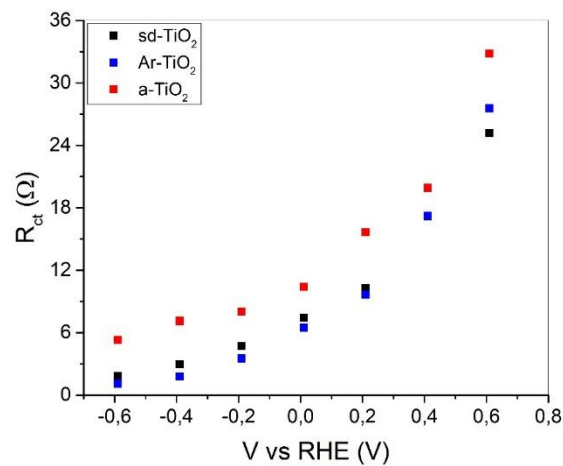


Figure 55. Catalyst resistance ( $R_{ct}$ ) plotted as function of the applied voltage.

- $Q_{dl}$ : the trend found for the constant phase element of the surface/electrolyte interface is in good agreement with the results shown for  $R_{ct}$ . If we consider the charge transfer time, by multiplying

$Q_{dl}$  by  $R_{ct}$ , it is evident that the presence of defects plays a key role in  $TiO_2$  catalysis, especially toward  $CO_2$  valorisation, by reducing the transfer time about ten times respect to a- $TiO_2$ .

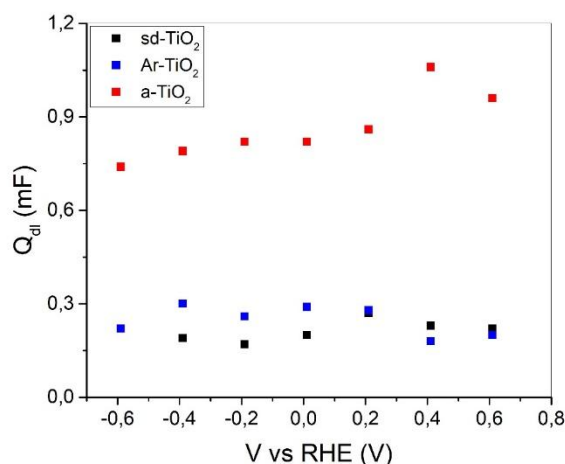


Figure 56. Quasi-capacity of the double layer ( $Q_{dl}$ ) plotted as function of the applied voltage.

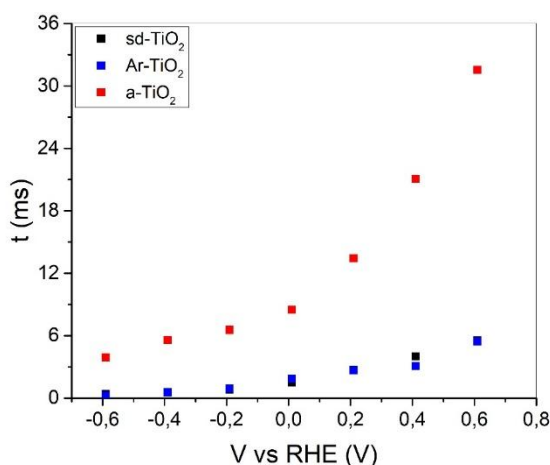


Figure 57. Transfer time (t) plotted as function of the applied voltage.

As a result, self-doped  $TiO_2$  demonstrated to have better catalytic properties than a- $TiO_2$ , with a small transfer time. However, the n-doping can cause an upward band bending at the surface of the catalyst, which will favour hole transfer to the solution more than electrons one, thus oxidative reactions will dominate. These results explain why a high over-potential was required to transfer electrons on  $CO_2$ , and so to reduce it to  $CO$  and  $CH_4$ , with the consequent increase of  $H_2$  evolution.

## 4.7 Band model and interpretation

The schematic representation of the band model of self-doped  $TiO_2$  has been carried on following the same procedure previously shown for  $SnO_2$ . The information on  $E_{gap}$ , taken from UV-Vis spectroscopy, valence band shape, from

HR-XPS, and doping type, from the Mott-Schottky plots, have been merged in order to better describe the semiconductive behaviour of the presented oxide material.

#### 4.7.1 Band gap calculation

The investigation of the optical properties of self-doped TiO<sub>2</sub> has been carried on through UV-Vis spectroscopy. The diffuse reflectance and the Kubelka Munk analysis (Chapter 2) are reported in Figure 58 (a) and (b) respectively.

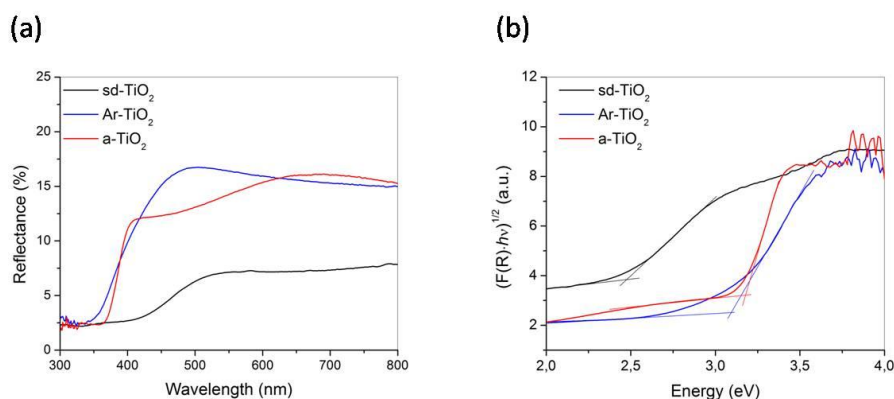


**Figure 58. (a) Diffuse reflectance spectra of TiO<sub>2</sub> samples and (b) the function derived from the modified Kubelka-Munk relation.**

In agreement with literature, we considered an indirect band gap for TiO<sub>2</sub> [56,57]. The calculated values are (2.49±0.01) eV for sd-TiO<sub>2</sub>, (3.09±0.04) eV for Ar-TiO<sub>2</sub>, and (3.19±0.01) eV for a-TiO<sub>2</sub>. While the E<sub>gap</sub> of a-TiO<sub>2</sub> corresponds to anatase TiO<sub>2</sub>, as expected from the XRD and XPS analysis, the E<sub>gap</sub> of self-doped TiO<sub>2</sub> is significantly reduced. The difference between sd-TiO<sub>2</sub> and Ar-TiO<sub>2</sub> samples can be attributed to the desorption of H<sub>2</sub>O<sub>2</sub>, due to the thermal treatment. The lack of the super-oxidized state is widening the band gap, thus moving its value closer to the anatase TiO<sub>2</sub>. These results confirm the possibility to tune the energy gap, thus moving the light absorption to the visible range, by treating the surface with H<sub>2</sub>O<sub>2</sub> in mild conditions while the synthesis is still occurring.

#### 4.7.2 Valence band shape characterization

Since some studies demonstrates that surface defects can affect the DOS of self-doped TiO<sub>2</sub>[54], we investigated the VB DOS distribution by observing the O 2p orbital (Figure 59) with XPS. All the reported energy values are referred to the 0 eV of B.E., if not stated differently. We found VB-top values of (3.3±0.1) eV, (3.3±0.1) eV for sd-TiO<sub>2</sub> and Ar-TiO<sub>2</sub> respectively, and (2.7±0.1) eV for a-TiO<sub>2</sub>.

The results obtained for the self-doped TiO<sub>2</sub> make us consider the Fermi level can not be set at 0 eV for these materials, otherwise the E<sub>F</sub> would sit inside the CB. Since the information on the DOS are not sufficient to explain this result, we will use the XPS outcomes to give a comment on the VB-shape modification caused by the defect sites, leaving the question open.

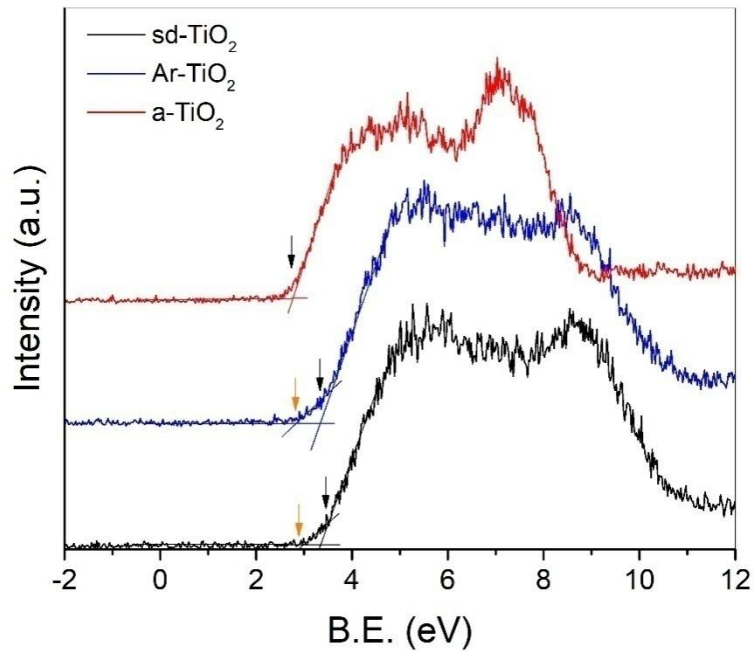


Figure 59. HR-XPS spectra of O 2p orbitals representative of the valence band of TiO<sub>2</sub> samples. The black arrows indicate the VB-top value without tailing, while the orange ones indicate the shift occurred with the band-tailing. The lines represent the curves used for the fitting.

The tailing of the VB was observed only in sd-TiO<sub>2</sub> and Ar-TiO<sub>2</sub> samples, causing its top-shift at  $(3.0 \pm 0.4)$  eV and  $(2.9 \pm 0.4)$  eV for sd-TiO<sub>2</sub> and Ar-TiO<sub>2</sub> respectively. The high uncertainty is associated to the low signal/noise ratio in that energy range.

Surface disorder is considered as a critical factor causing VB-top tailing. Fan et al. [65] demonstrated that the VB-top tailing could be tuned by introducing hydroxyls groups. We considered this interpretation matching our results since it has been demonstrated from XPS (Fig. 44 (a)) that the surface of sd-TiO<sub>2</sub> samples is rich in -OH groups. The observed VB-top tailing has the effect to shrink the energy gap, shifting the absorption from the UV to the visible range of the electromagnetic spectrum.

### 4.7.3 Built in potential evaluation

By looking at the electrolyte interface, the measured built-in potential are  $(0.93 \pm 0.02)$  V,  $(0.64 \pm 0.04)$  V and  $(0.02 \pm 0.02)$  V for sd-TiO<sub>2</sub>, Ar-TiO<sub>2</sub> and a-TiO<sub>2</sub> respectively (Figure 60).

The presented results are in good agreement with our expectation. In fact, the high donor density calculated for sd-TiO<sub>2</sub> and Ar-TiO<sub>2</sub> is expected to move the Fermi level closer to the CB, enhancing the n-doping. This variation in the  $E_F$  position gives the rise to an higher band bending, than the one observed for a-TiO<sub>2</sub>.

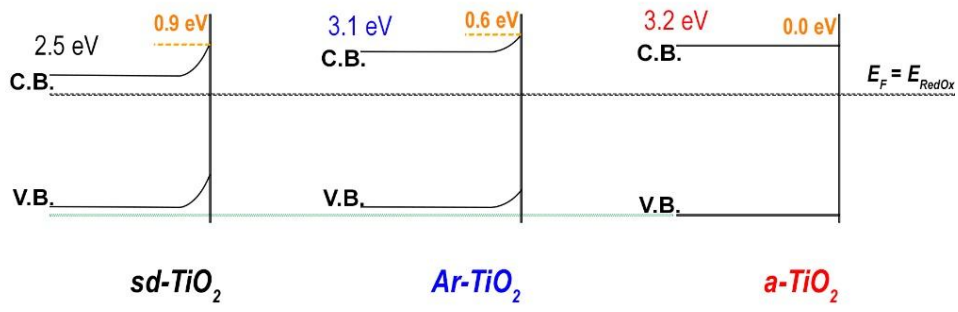


Figure 60. Band scheme of TiO<sub>2</sub> samples showing the semiconductor/electrolyte interface in equilibrium condition ( $E_F = E_{RedOx}$ ). In orange the built-in potential values.

# Chapter 5

## Conclusions

An in deep analysis on surface properties of semiconductor metal oxides has been presented.

The main purpose of the presented work is the modification of the physical properties of semiconductors aiming to realize a performing material that can be employed for CO<sub>2</sub> valorisation.

For these reasons, surface decoration, defects engineering and doping have been investigated on two cheap, earth abundant and widespread metal oxides: SnO<sub>2</sub> and TiO<sub>2</sub>.

The use of different spectroscopies, such as x-ray photoelectron and electron paramagnetic spectroscopies, coupled with impedance measurements is the key factor that drove the characterization of the selected metal-oxides through the right interpretation of the catalytic performances.

In line with these principles, since the catalytic tests are carried on an electrochemical solution, electrochemical impedance spectroscopy has been employed to unravel the electrical properties of the materials, pointing out the issues leading to limitations charge-transfer. Thanks to an in-deep investigation, the bulk transfer limitation, associated to the intrinsic properties of the investigated oxides, could be separated to the one of surface, which depends on defect engineering. Moreover, the graphical representation of the electronical levels of the semiconductor/electrolyte junction helped to gain a deeper understanding on the potential raised by the Schottky junction, thus guiding to a comprehensive interpretation of the collected results.

### 5.1 Tin Oxide

Preliminary studies conducted on SnO<sub>2</sub> with Bejtka's group allowed to gain the fundamentals on the realization of a high surface area, porous structure realized via anodic oxidation, a cheap and easily scalable synthesis. Moreover, the work helped to establish the protocols for CO<sub>2</sub> valorisation tests and guided the choice toward doping to overcome the material intrinsic limits.

In fact, doped-SnO<sub>2</sub> resulted to be more robust and active metal oxide for CO<sub>2</sub> valorisation. This outcome made us consider the doping as the optimal strategy to improve both bulk and surface properties of metal oxides.

From CO<sub>2</sub> valorisation tests resulted that Ti substitution would not help the production of HCOOH, thus contrasting the DFT results presented in literature. The doping gave as results the retention of the n-type behaviour of SnO<sub>2</sub>, and a major selectivity toward H<sub>2</sub> evolution.

A better result was obtained with a change in the doping behaviour. The major charge carriers variation was obtained through Fe<sup>3+</sup> insertion. This allowed to gain the best results in terms of selectivity and current densities toward CO<sub>2</sub> valorisation, about three times higher than bare SnO<sub>2</sub>.

The results have been explained looking at the charge transfer kinetics. Impedance spectroscopy was used giving as a result a faster electron transfer to the CO<sub>2</sub>-saturated electrolyte for Fe-doped SnO<sub>2</sub>.

## 5.2 Self-doped titanium dioxide

A single step synthesis and decoration mediated by hydrogen peroxide demonstrated to be an efficient, sustainable and novel way to tune the band gap width and the surface capability to adsorb and react in a CO<sub>2</sub>-reach environment.

As a result, H<sub>2</sub>O<sub>2</sub> lead to the formation of a hydroxyl-rich surface, where the electrons carried by –OH species changed the oxidation state of Ti<sup>4+</sup> to Ti<sup>3+</sup>. The decoration introduces trapping states localized close to the valence band top, thus resulting in the formation of a tail in the density of states. It causes a reduction of the band gap, as demonstrated from the HR-XPS of the O 2p orbital and the UV-vis spectroscopy.

The electrochemical test for CO<sub>2</sub> valorisation demonstrated that even after the peroxide removal at 150 °C in argon atmosphere, TiO<sub>2</sub> defective surface retained its enhanced catalytic properties, respect to anatase TiO<sub>2</sub>, as expected from literature outcomes.

Through the impedentiometric analysis, it has been found out that the major advantage of the surface defects lays in fast charge transfer of electrons from the surface to adsorbed species, in this case CO<sub>2</sub>. The study of the electron transfer kinetics led to the evidence that in self-doped TiO<sub>2</sub> the transfer results to be fastest among all the investigated materials (few milliseconds).

The donor density variation, as well as the current density measured during the CO<sub>2</sub> valorisation tests have been explained by looking at the junction model. It summarized the results on the engineering of the E<sub>gap</sub>, together with the effects of the E<sub>F</sub> alignment with the RedOx potential of the electrolyte on the built-in potential raised at the metal-oxide surface.

## 5.3 Future perspectives

Based on the presented results, it is possible to gather the receipt for the creation of a highly performing catalyst based on metal oxides semiconductors.

The focus has to be put on p-doped semiconductors to guarantee a proper band structure, whose built-in potential favours the electron displacement at the surface. The doping has to be coupled with surface engineering through defects decoration induced via the introduction of super oxide states. This would help CO<sub>2</sub> adsorption and open the possibility to visible-light-driven electrocatalysis.

# References

1. General Assembly, United Nations The 2030 Agenda for Sustainable Development. In Proceedings of the Resolution adopted by the General Assembly on 25 September 2015; 2015.
2. Pauli, A.G. *Blue economy. Rapporto al Club di Roma. 10 anni, 100 innovazioni, 100 milioni di posti di lavoro*; Edizioni Ambiente, 2014, Ed.; Gianfranco, Bologna, 2014; ISBN 8866271241, 9788866271246.
3. Ciamician, G.L. The Photochemistry of the Future. *Science (80-. )*. **1912**, *36*, 385–394.
4. IPCC Proposed outline of the special report in 2018 on the impacts of global warming of 1.5 °C above pre-industrial levels and related global greenhouse gas emission pathways , in the context of strengthening the global response to the threat of climate change. *Ippc - Sr15* **2018**, *2*, 17–20.
5. Roy, N.; Suzuki, N.; Terashima, C.; Fujishima, A. Recent improvements in the production of solar fuels: From CO<sub>2</sub> reduction to water splitting and artificial photosynthesis. *Bull. Chem. Soc. Jpn.* **2019**, *92*, 178–192.
6. Kalamaras, E.; Maroto-Valer, M.M.; Shao, M.; Xuan, J.; Wang, H. Solar carbon fuel via photoelectrochemistry. *Catal. Today* **2018**, *317*, 56–75.
7. Taiz, L.; Zeiger, E. *Plant Physiology*; 4th ed.; Piccinin-Nuova Libraria, 2012; ISBN 8829921572.
8. Enderle, J.D. *Compartmental Modeling*; 3rd ed.; Elsevier Inc., 2011; ISBN 9780123749796.
9. Daomin Zhou, D. Microelectrodes for in-vivo determination of pH. *Electrochem. Sensors, Biosens. their Biomed. Appl.* **2008**, 261–305.
10. Gibson, D.H. The organometallic chemistry of carbon dioxide. *Chem. Rev.* **1996**, *96*, 2063–2095.
11. Apaydin, D.H.; Schlager, S.; Portenkirchner, E.; Sariciftci, N.S. Organic, Organometallic and Bioorganic Catalysts for Electrochemical Reduction of CO<sub>2</sub>. *ChemPhysChem* **2017**, *18*, 3094–3116.
12. Jia, C.; Dastafkan, K.; Ren, W.; Yang, W.; Zhao, C. Carbon-based catalysts for electrochemical CO<sub>2</sub> reduction. *Sustain. Energy Fuels* **2019**, *3*, 2890–2906.
13. Hou, L.; Yan, J.; Takele, L.; Wang, Y.; Yan, X.; Gao, Y. Current progress of metallic and carbon-based nanostructure catalysts towards the electrochemical reduction of CO<sub>2</sub>. *Inorg. Chem. Front.* **2019**, *6*.
14. Wu, J.; Sharifi, T.; Gao, Y.; Zhang, T.; Ajayan, P.M. Emerging Carbon-Based Heterogeneous Catalysts for Electrochemical Reduction of Carbon Dioxide into Value-Added Chemicals. *Adv. Mater.* **2019**, *31*, 1–24.
15. Zhao, S.; Jin, R.; Jin, R. Opportunities and Challenges in CO<sub>2</sub> Reduction by Gold- and Silver-Based Electrocatalysts: From Bulk Metals to Nanoparticles and Atomically Precise Nanoclusters. *ACS Energy Lett.* **2018**, *3*, 452–462.
16. Tayyebi, E.; Hussain, J.; Abghoui, Y.; Skúlason, E. Trends of Electrochemical CO<sub>2</sub> Reduction Reaction on Transition Metal Oxide Catalysts. *J. Phys. Chem. C* **2018**, *122*, 10078–10087.
17. Shi, R.; Waterhouse, G.I.N.; Zhang, T. Recent Progress in Photocatalytic CO<sub>2</sub> Reduction Over Perovskite Oxides . *Sol. RRL* **2017**, *1*, 1700126.

18. Saravanan, K.; Basdogan, Y.; Dean, J.; Keith, J.A. Computational investigation of CO<sub>2</sub> electroreduction on tin oxide and predictions of Ti, V, Nb and Zr dopants for improved catalysis. *J. Mater. Chem. A* **2017**, *5*, 11756–11763.
19. Fochs, P.D. The measurement of the energy gap of semiconductors from their diffuse reflection spectra. *Proc. Phys. Soc. Sect. B* **1956**, *69*, 70–75.
20. Tandon, S.P.; Gupta, J.P. Measurement of Forbidden Energy Gap of Semiconductors by Diffuse Reflectance Technique. *Phys. Status Solidi* **1970**, *38*, 363–367.
21. López, R.; Gómez, R. Band-gap energy estimation from diffuse reflectance measurements on sol-gel and commercial TiO<sub>2</sub>: A comparative study. *J. Sol-Gel Sci. Technol.* **2012**, *61*, 1–7.
22. Corson, E.R.; Creel, E.B.; Kim, Y.; Urban, J.J.; Kostecki, R.; McCloskey, B.D. A temperature-controlled photoelectrochemical cell for quantitative product analysis. *Rev. Sci. Instrum.* **2018**, *89*.
23. Sacco, A.; Zeng, J.; Bejtka, K.; Chiodoni, A. Modeling of gas bubble-induced mass transport in the electrochemical reduction of carbon dioxide on nanostructured electrodes. *J. Catal.* **2019**, *372*, 39–48.
24. Das, S.; Jayaraman, V. SnO<sub>2</sub>: A comprehensive review on structures and gas sensors. *Prog. Mater. Sci.* **2014**, *66*, 112–255.
25. Xiong, L.; Guo, Y.; Wen, J.; Liu, H.; Yang, G.; Qin, P.; Fang, G. Review on the Application of SnO<sub>2</sub> in Perovskite Solar Cells. *Adv. Funct. Mater.* **2018**, *28*, 1–18.
26. Zhao, S.; Li, S.; Guo, T.; Zhang, S.; Wang, J.; Wu, Y.; Chen, Y. Advances in Sn-Based Catalysts for Electrochemical CO<sub>2</sub> Reduction. *Nano-Micro Lett.* **2019**, *11*.
27. Batzill, M.; Diebold, U. The surface and materials science of tin oxide. *Prog. Surf. Sci.* **2005**, *79*, 47–154.
28. Li, F.; Chen, L.; Knowles, G.P.; MacFarlane, D.R.; Zhang, J. Hierarchical Mesoporous SnO<sub>2</sub> Nanosheets on Carbon Cloth: A Robust and Flexible Electrocatalyst for CO<sub>2</sub> Reduction with High Efficiency and Selectivity. *Angew. Chemie - Int. Ed.* **2017**, *56*, 505–509.
29. Li, Y.; Qiao, J.; Zhang, X.; Lei, T.; Girma, A.; Liu, Y.; Zhang, J. Rational Design and Synthesis of SnO<sub>x</sub> Electrocatalysts with Coralline Structure for Highly Improved Aqueous CO<sub>2</sub> Reduction to Formate. *ChemElectroChem* **2016**, *3*, 1618–1628.
30. Yu, J.; Liu, H.; Song, S.; Wang, Y.; Tsiakaras, P. Electrochemical reduction of carbon dioxide at nanostructured SnO<sub>2</sub>/carbon aerogels: The effect of tin oxide content on the catalytic activity and formate selectivity. *Appl. Catal. A Gen.* **2017**, *545*, 159–166.
31. Kumar, B.; Atla, V.; Brian, J.P.; Kumari, S.; Nguyen, T.Q.; Sunkara, M.; Spurgeon, J.M. Reduced SnO<sub>2</sub> Porous Nanowires with a High Density of Grain Boundaries as Catalysts for Efficient Electrochemical CO<sub>2</sub>-into-HCOOH Conversion. *Angew. Chemie - Int. Ed.* **2017**, *56*, 3645–3649.
32. Won, D.H.; Choi, C.H.; Chung, J.; Chung, M.W.; Kim, E.H.; Woo, S.I. Rational Design of a Hierarchical Tin Dendrite Electrode for Efficient Electrochemical Reduction of CO<sub>2</sub>. *ChemSusChem* **2015**, *8*, 3092–3098.
33. Hu, H.; Gui, L.; Zhou, W.; Sun, J.; Xu, J.; Wang, Q.; He, B.; Zhao, L. Partially reduced Sn/SnO<sub>2</sub> porous hollow fiber: A highly selective, efficient and robust electrocatalyst towards carbon dioxide reduction. *Electrochim. Acta* **2018**, *285*, 70–77.

34. Wang, M.; Liu, Y.; Xue, D.; Zhang, D.; Yang, H. Preparation of nanoporous tin oxide by electrochemical anodization in alkaline electrolytes. *Electrochim. Acta* **2011**, *56*, 8797–8801.
35. Dutta, A.; Kuzume, A.; Rahaman, M.; Vesztergom, S.; Broekmann, P. Monitoring the Chemical State of Catalysts for CO<sub>2</sub> Electroreduction: An In Operando Study. *ACS Catal.* **2015**, *5*, 7498–7502.
36. Bejtka, K.; Zeng, J.; Sacco, A.; Castellino, M.; Hernández, S.; Farkhondehfar, M.A.; Savino, U.; Ansaloni, S.; Pirri, C.F.; Chiodoni, A. Chainlike Mesoporous SnO<sub>2</sub> as a Well-Performing Catalyst for Electrochemical CO<sub>2</sub> Reduction. *ACS Appl. Energy Mater.* **2019**, *2*, 3081–3091.
37. Ge, H.; Gu, Z.; Han, P.; Shen, H.; Al-Enizi, A.M.; Zhang, L.; Zheng, G. Mesoporous tin oxide for electrocatalytic CO<sub>2</sub> reduction. *J. Colloid Interface Sci.* **2018**, *531*, 564–569.
38. Kim, K.S.; Kim, W.J.; Lim, H.K.; Lee, E.K.; Kim, H. Tuned Chemical Bonding Ability of Au at Grain Boundaries for Enhanced Electrochemical CO<sub>2</sub> Reduction. *ACS Catal.* **2016**, *6*, 4443–4448.
39. Feng, X.; Jiang, K.; Fan, S.; Kanan, M.W. A direct grain-boundary-activity correlation for CO electroreduction on Cu nanoparticles. *ACS Cent. Sci.* **2016**, *2*, 169–174.
40. Jain, K.; Pant, R.P.; Lakshmikumar, S.T. Effect of Ni doping on thick film SnO<sub>2</sub> gas sensor. *Sensors Actuators, B Chem.* **2006**, *113*, 823–829.
41. Palacios-Padrós, A.; Altomare, M.; Tighineanu, A.; Kirchgeorg, R.; Shrestha, N.K.; Díez-Pérez, I.; Caballero-Briones, F.; Sanz, F.; Schmuki, P. Growth of ordered anodic SnO<sub>2</sub> nanochannel layers and their use for H<sub>2</sub> gas sensing. *J. Mater. Chem. A* **2014**, *2*, 915–920.
42. Bhagwat, A.D.; Sawant, S.S.; Ankamwar, B.G.; Mahajan, C.M. Synthesis of nanostructured tin oxide (SnO<sub>2</sub>) powders and thin films by sol-gel method. *J. Nano- Electron. Phys.* **2015**, *7*, 7–10.
43. Rao, G.T.; Babu, B.; Ravikumar, R.V.S.S.N.; Shim, J.; Reddy, C.V. Structural and optical properties of Fe-doped SnO<sub>2</sub> quantum dots. *Mater. Res. Express* **2017**, *4*.
44. Chen, Z.; Fan, T.; Zhang, Y.Q.; Xiao, J.; Gao, M.; Duan, N.; Zhang, J.; Li, J.; Liu, Q.; Yi, X.; et al. Wavy SnO<sub>2</sub> catalyzed simultaneous reinforcement of carbon dioxide adsorption and activation towards electrochemical conversion of CO<sub>2</sub> to HCOOH. *Appl. Catal. B Environ.* **2020**, *261*, 118243.
45. Ran, L.; Zhao, D.; Gao, X.; Yin, L. Highly crystalline Ti-doped SnO<sub>2</sub> hollow structured photocatalyst with enhanced photocatalytic activity for degradation of organic dyes. *CrystEngComm* **2015**, *17*, 4225–4237.
46. Xing, H.; Liu, Z.; Lin, L.; Wang, L.; Tan, D.; Gan, Y.; Ji, X.; Xu, G. Excellent microwave absorption properties of Fe ion-doped SnO<sub>2</sub>/multi-walled carbon nanotube composites. *RSC Adv.* **2016**, *6*, 41656–41664.
47. Lee, S.; Ocon, J.D.; Son, Y. Il; Lee, J. Alkaline CO<sub>2</sub> electrolysis toward selective and continuous HCOO<sup>-</sup> production over SnO<sub>2</sub> nanocatalysts. *J. Phys. Chem. C* **2015**, *119*, 4884–4890.
48. Dutta, A.; Kuzume, A.; Kaliginedi, V.; Rahaman, M.; Sinev, I.; Ahmadi, M.; Roldán Cuenya, B.; Vesztergom, S.; Broekmann, P. Probing the chemical state of tin oxide NP catalysts during CO<sub>2</sub> electroreduction: A complementary operando approach. *Nano Energy* **2018**, *53*, 828–840.
49. Deng, W.; Zhang, L.; Li, L.; Chen, S.; Hu, C.; Zhao, Z.J.; Wang, T.; Gong, J. Crucial Role of Surface Hydroxyls on the Activity and Stability in

- Electrochemical CO<sub>2</sub> Reduction. *J. Am. Chem. Soc.* **2019**, *141*, 2911–2915.
50. Baruch, M.F.; Pander, J.E.; White, J.L.; Bocarsly, A.B. Mechanistic Insights into the Reduction of CO<sub>2</sub> on Tin Electrodes using in Situ ATR-IR Spectroscopy. *ACS Catal.* **2015**, *5*, 3148–3156.
  51. Usman, M.S.; Ibrahim, N.A.; Shamel, K.; Zainuddin, N.; Yunus, W.M.Z.W. Copper nanoparticles mediated by chitosan: Synthesis and characterization via chemical methods. *Molecules* **2012**, *17*, 14928–14936.
  52. Zhang, D.; Bai, F.; Sun, L.; Wang, Y.; Wang, J. Compression properties and electrical conductivity of in-situ 20 vol.% nano-sized TiC<sub>x</sub>/Cu composites with different particle size and morphology. *Materials (Basel)*. **2017**, *10*, 1–10.
  53. Yousif, A.A.; Reeman, M.H. The Influence of Antimony-doping Contents on the Structure and Optical Properties of Tin Oxide Thin Films Prepared by Spray Pyrolysis Technique. **2017**, *3*, 2229–2233.
  54. Liu, X.; Zhu, G.; Wang, X.; Yuan, X.; Lin, T.; Huang, F. Progress in Black Titania: A New Material for Advanced Photocatalysis. *Adv. Energy Mater.* **2016**, *6*.
  55. Fujishima, A., & Honda, K. Electrochemical Photolysis of Water One and Two-dimensional Structure of Poly ( L-Alanine ) shown by Specific Heat Measurements at Low Temperatures (1.5-20 K). *Nature* **1972**, *238*, 37–38.
  56. Di Paola, A.; Bellardita, M.; Palmisano, L. Brookite, the least known TiO<sub>2</sub> photocatalyst; **2013**; Vol. 3; ISBN 3909170250.
  57. Zhang, J.; Zhou, P.; Liu, J.; Yu, J. New understanding of the difference of photocatalytic activity among anatase, rutile and brookite TiO<sub>2</sub>. *Phys. Chem. Chem. Phys.* **2014**, *16*, 20382–20386.
  58. Sekiya, T.; Yagisawa, T.; Kamiya, N.; Mulmi, D. Das; Kurita, S.; Murakami, Y.; Kodaira, T. Defects in anatase TiO<sub>2</sub> single crystal controlled by heat treatments. *J. Phys. Soc. Japan* **2004**, *73*, 703–710.
  59. Na-Phattalung, S.; Smith, M.F.; Kim, K.; Du, M.H.; Wei, S.H.; Zhang, S.B.; Limpijumnong, S. First-principles study of native defects in anatase TiO<sub>2</sub>. *Phys. Rev. B - Condens. Matter Mater. Phys.* **2006**, *73*, 1–6.
  60. Berger, T.; Sterrer, M.; Diwald, O.; Knözinger, E.; Panayotov, D.; Thompson, T.L.; Yates, J.T. Light-induced charge separation in anatase TiO<sub>2</sub> particles. *J. Phys. Chem. B* **2005**, *109*, 6061–6068.
  61. Henderson, M.A.; Epling, W.S.; Peden, C.H.F.; Perkins, C.L. Insights into photoexcited electron scavenging processes on TiO<sub>2</sub> obtained from studies of the reaction of O<sub>2</sub> with OH groups adsorbed at electronic defects on TiO<sub>2</sub>(110). *J. Phys. Chem. B* **2003**, *107*, 534–545.
  62. Szczepankiewicz, S.H.; Colussi, A.J.; Hoffmann, M.R. Infrared Spectra of Photoinduced Species on Hydroxylated Titania Surfaces. *J. Phys. Chem. B* **2002**, *104*, 9842–9850.
  63. Szczepankiewicz, S.H.; Moss, J.A.; Hoffmann, M.R. Slow surface charge trapping kinetics on irradiated TiO<sub>2</sub>. *J. Phys. Chem. B* **2002**, *106*, 2922–2927.
  64. Anpo, M.; Che, M.; Fubini, B.; Garrone, E.; Giamello, E.; Paganini, M.C. ChemInform Abstract: Generation of Superoxide Ions at Oxide Surfaces. *ChemInform* **2010**, *30*, 42.
  65. Ren, Z.; Wang, J.; Wang, Z.; Fu, X.; Fan, C.; Qian, G.; Chen, C. Black Hydroxylated Titanium Dioxide Prepared via Ultrasonication with Enhanced Photocatalytic Activity. *Sci. Rep.* **2015**, *5*, 1–10.
  66. Panomsuwan, G.; Watthanaphanit, A.; Ishizaki, T.; Saito, N. Water-

- plasma-assisted synthesis of black titania spheres with efficient visible-light photocatalytic activity. *Phys. Chem. Chem. Phys.* **2015**, *17*, 13794–13799.
67. Mao, S.S.; Chen, X.B.; Liu, L.; Yu, P.Y. Increasing Solar Absorption for Photocatalysis with Black Hydrogenated Titanium Dioxide Nanocrystals. *Science (80-. )*. **2011**, *331*, 746–750.
  68. Elbanna, O.; Fujitsuka, M.; Kim, S.; Majima, T. Charge Carrier Dynamics in TiO<sub>2</sub> Mesocrystals with Oxygen Vacancies for Photocatalytic Hydrogen Generation under Solar Light Irradiation. *J. Phys. Chem. C* **2018**, *122*, 15163–15170.
  69. Pesci, F.M.; Wang, G.; Klug, D.R.; Li, Y.; Cowan, A.J. Efficient suppression of electron-hole recombination in oxygen-deficient hydrogen-treated TiO<sub>2</sub> nanowires for photoelectrochemical water splitting. *J. Phys. Chem. C* **2013**, *117*, 25837–25844.
  70. Naldoni, A.; Altomare, M.; Zoppellaro, G.; Liu, N.; Kment, Š.; Zbořil, R.; Schmuki, P. Photocatalysis with reduced TiO<sub>2</sub>: From Black TiO<sub>2</sub> to cocatalyst-free hydrogen production. *ACS Catal.* **2019**, *9*, 345–364.
  71. Sinhamahapatra, A.; Jeon, J.P.; Yu, J.S. A new approach to prepare highly active and stable black titania for visible light-assisted hydrogen production. *Energy Environ. Sci.* **2015**, *8*, 3539–3544.
  72. Li, S.; Qiu, J.; Ling, M.; Peng, F.; Wood, B.; Zhang, S. Photoelectrochemical characterization of hydrogenated TiO<sub>2</sub> nanotubes as photoanodes for sensing applications. *ACS Appl. Mater. Interfaces* **2013**, *5*, 11129–11135.
  73. Wang, X.; Zhang, S.; Wang, H.; Yu, H.; Wang, H.; Zhang, S.; Peng, F. Visible light photoelectrochemical properties of a hydrogenated TiO<sub>2</sub> nanorod film and its application in the detection of chemical oxygen demand. *RSC Adv.* **2015**, *5*, 76315–76320.
  74. Ji, Y.; Guo, W.; Chen, H.; Zhang, L.; Chen, S.; Hua, M.; Long, Y.; Chen, Z. Surface Ti<sup>3+</sup>/Ti<sup>4+</sup> Redox Shuttle Enhancing Photocatalytic H<sub>2</sub> Production in Ultrathin TiO<sub>2</sub> Nanosheets/CdSe Quantum Dots. *J. Phys. Chem. C* **2015**, *119*, 27053–27059.
  75. Jiang, B.; Tang, Y.; Qu, Y.; Wang, J.Q.; Xie, Y.; Tian, C.; Zhou, W.; Fu, H. Thin carbon layer coated Ti<sup>3+</sup>-TiO<sub>2</sub> nanocrystallites for visible-light driven photocatalysis. *Nanoscale* **2015**, *7*, 5035–5045.
  76. Su, T.; Yang, Y.; Na, Y.; Fan, R.; Li, L.; Wei, L.; Yang, B.; Cao, W. An insight into the role of oxygen vacancy in hydrogenated TiO<sub>2</sub> nanocrystals in the performance of dye-sensitized solar cells. *ACS Appl. Mater. Interfaces* **2015**, *7*, 3754–3763.
  77. Zhang, C.; Xie, Y.; Ma, J.; Hu, J.; Zhang, C. A composite catalyst of reduced black TiO<sub>2-x</sub>/CNT: A highly efficient counter electrode for ZnO-based dye-sensitized solar cells. *Chem. Commun.* **2015**, *51*, 17459–17462.
  78. Chen, Y.; Tao, Q.; Fu, W.; Yang, H.; Zhou, X.; Su, S.; Ding, D.; Mu, Y.; Li, X.; Li, M. Enhanced photoelectric performance of PbS/CdS quantum dot co-sensitized solar cells via hydrogenated TiO<sub>2</sub> nanorod arrays. *Chem. Commun.* **2014**, *50*, 9509–9512.
  79. Qingli, W.; Zhaoguo, Z.; Xudong, C.; Zhengfeng, H.; Peimei, D.; Yi, C.; Xiwen, Z. Photoreduction of CO<sub>2</sub> using black TiO<sub>2</sub> films under solar light. *J. CO<sub>2</sub> Util.* **2015**, *12*, 7–11.
  80. Qiu, J.; Li, S.; Gray, E.; Liu, H.; Gu, Q.F.; Sun, C.; Lai, C.; Zhao, H.; Zhang, S. Hydrogenation synthesis of blue TiO<sub>2</sub> for high-performance lithium-ion batteries. *J. Phys. Chem. C* **2014**, *118*, 8824–8830.

81. Myung, S.T.; Kikuchi, M.; Yoon, C.S.; Yashiro, H.; Kim, S.J.; Sun, Y.K.; Scrosati, B. Black anatase titania enabling ultra high cycling rates for rechargeable lithium batteries. *Energy Environ. Sci.* **2013**, *6*, 2609–2614.
82. Tian, M.; Mahjouri-Samani, M.; Eres, G.; Sachan, R.; Yoon, M.; Chisholm, M.F.; Wang, K.; Paretzky, A.A.; Rouleau, C.M.; Geohegan, D.B.; et al. Structure and Formation Mechanism of Black TiO<sub>2</sub> Nanoparticles. *ACS Nano* **2015**, *9*, 10482–10488.
83. Wang, Z.; Yang, C.; Lin, T.; Yin, H.; Chen, P.; Wan, D.; Xu, F.; Huang, F.; Lin, J.; Xie, X.; et al. Visible-light photocatalytic, solar thermal and photoelectrochemical properties of aluminium-reduced black titania. *Energy Environ. Sci.* **2013**, *6*, 3007–3014.
84. Zheng, Z.; Huang, B.; Meng, X.; Wang, J.; Wang, S.; Lou, Z.; Wang, Z.; Qin, X.; Zhang, X.; Dai, Y. Metallic zinc- assisted synthesis of Ti<sup>3+</sup> self-doped TiO<sub>2</sub> with tunable phase composition and visible-light photocatalytic activity. *Chem. Commun.* **2013**, *49*, 868–870.
85. Wu, T.; Zuo, F.; Zhang, Z.; Borchardt, D.; Feng, P.; Wang, L. Self-Doped Ti<sup>3+</sup> Enhanced Photocatalyst for Hydrogen Production under Visible Light . *J. Am. Chem. Soc.* **2010**, *132*, 11856–11857.
86. Tan, H.; Zhao, Z.; Niu, M.; Mao, C.; Cao, D.; Cheng, D.; Feng, P.; Sun, Z. A facile and versatile method for preparation of colored TiO<sub>2</sub> with enhanced solar-driven photocatalytic activity. *Nanoscale* **2014**, *6*, 10216–10223.
87. Mao, C.; Zuo, F.; Hou, Y.; Bu, X.; Feng, P. In Situ Preparation of a Ti<sup>3+</sup> Self-Doped TiO<sub>2</sub> Film with Enhanced Activity as Photoanode by N<sub>2</sub>H<sub>4</sub> Reduction. *Angew. Chemie - Int. Ed.* **2014**, *53*, 10485–10489.
88. Zhu, G.; Yin, H.; Yang, C.; Cui, H.; Wang, Z.; Xu, J.; Lin, T.; Huang, F. Black Titania for Superior Photocatalytic Hydrogen Production and Photoelectrochemical Water Splitting. *ChemCatChem* **2015**, *7*, 2614–2619.
89. Lepcha, A.; Maccato, C.; Mettenbörger, A.; Andreu, T.; Mayrhofer, L.; Walter, M.; Olthof, S.; Ruoko, T.P.; Klein, A.; Moseler, M.; et al. Electrospun Black Titania Nanofibers: Influence of Hydrogen Plasma-Induced Disorder on the Electronic Structure and Photoelectrochemical Performance. *J. Phys. Chem. C* **2015**, *119*, 18835–18842.
90. Ciriminna, R.; Albanese, L.; Meneguzzo, F.; Pagliaro, M. Hydrogen Peroxide: A Key Chemical for Today's Sustainable Development. *ChemSusChem* **2016**, *9*, 3374–3381.
91. Reactions, G.C. *Green Chemical Reactions*; **2009**; ISBN 9781402084560.
92. Ayers, M.R.; Hunt, A.J. Titanium oxide aerogels prepared from titanium metal and hydrogen peroxide. *Mater. Lett.* **1998**, *34*, 290–293.
93. Grabstanowicz, L.R.; Gao, S.; Li, T.; Rickard, R.M.; Rajh, T.; Liu, D.J.; Xu, T. Facile oxidative conversion of TiH<sub>2</sub> to high-concentration Ti<sup>3+</sup>-self-doped rutile TiO<sub>2</sub> with visible-light photoactivity. *Inorg. Chem.* **2013**, *52*, 3884–3890.
94. Huang, X.; Liu, Z. Synthesis and Growth Mechanism of Net-like Titanate Nanowire Films via Low-temperature and Low-alkali-concentration Route. *Nano-Micro Lett.* **2014**, *5*, 93–100.
95. Liu, X.; Gao, S.; Xu, H.; Lou, Z.; Wang, W.; Huang, B.; Dai, Y. Green synthetic approach for Ti<sup>3+</sup> self-doped TiO<sub>2-x</sub> nanoparticles with efficient visible light photocatalytic activity. *Nanoscale* **2013**, *5*, 1870–1875.
96. Zheng, Y.; Cai, J.; Lv, K.; Sun, J.; Ye, H.; Li, M. Hydrogen peroxide assisted rapid synthesis of TiO<sub>2</sub> hollow microspheres with enhanced

- photocatalytic activity. *Appl. Catal. B Environ.* **2014**, *147*, 789–795.
97. Wu, J.M. Low-temperature preparation of titania nanorods through direct oxidation of titanium with hydrogen peroxide. *J. Cryst. Growth* **2004**, *269*, 347–355.
  98. Wu, J.M.; Zhang, T.W.; Zeng, Y.W.; Hayakawa, S.; Tsuru, K.; Osaka, A. Large-scale preparation of ordered titania nanorods with enhanced photocatalytic activity. *Langmuir* **2005**, *21*, 6995–7002.
  99. Wu, J.M.; Tsuru, K.; Osaka, A.; Hayakawa, S.; Wang, M. In Vitro Bioactivity of Hydrogen Peroxide Modified Titanium: Effects of Surface Morphology and Film Thickness. *Key Eng. Mater.* **2009**, *309–311*, 407–410.
  100. Wen, M.; Gu, J.F.; Liu, G.; Wang, Z.B.; Lu, J. Surface evolution of a gradient structured Ti in hydrogen peroxide solution. *Appl. Surf. Sci.* **2008**, *254*, 2905–2910.
  101. Wang, X.; Wang, L.; Lu, G.Q.; Cheng, H.-M.; Chen, Z.; Yan, X.; Liu, G. Synthesis of rutile–anatase core–shell structured TiO<sub>2</sub> for photocatalysis. *J. Mater. Chem.* **2009**, *19*, 6590.
  102. Ullattil, S.G.; Narendranath, S.B.; Pillai, S.C.; Periyat, P. Black TiO<sub>2</sub> Nanomaterials: A Review of Recent Advances. *Chem. Eng. J.* **2018**, *343*, 708–736.
  103. Liu, L.; Yu, P.Y.; Chen, X.; Mao, S.S.; Shen, D.Z. Hydrogenation and disorder in engineered black TiO<sub>2</sub>. *Phys. Rev. Lett.* **2013**, *111*, 1–5.
  104. Aronsson, B.-O.; Krozer, A.; Lausmaa, J.; Kasemo, B. Commercially Pure Titanium and Ti<sub>6</sub>Al<sub>4</sub>V: XPS Comparison Between Different Commercial Ti Dental Implants and Foils Prepared by Various Oxidation Procedures. *Surf. Sci. Spectra* **1996**, *4*, 42–89.
  105. Devi, L.G.; Nithya, P.M.; Abraham, C.; Kavitha, R. Influence of surface metallic silver deposit and surface fluorination on the photocatalytic activity of rutile TiO<sub>2</sub> for the degradation of crystal violet a cationic dye under UV light irradiation. *Mater. Today Commun.* **2017**, *10*, 1–13.
  106. Lin, T.; Yang, C.; Wang, Z.; Yin, H.; Lü, X.; Huang, F.; Lin, J.; Xie, X.; Jiang, M. Effective nonmetal incorporation in black titania with enhanced solar energy utilization. *Energy Environ. Sci.* **2014**, *7*, 967–972.
  107. Zou, J.; Gao, J.; Wang, Y. Synthesis of highly active H<sub>2</sub>O<sub>2</sub>-sensitized sulfated titania nanoparticles with a response to visible light. *J. Photochem. Photobiol. A Chem.* **2009**, *202*, 128–135.
  108. Radtke, A.; Piszczek, P.; Topolski, A.; Lewandowska, Z.; Talik, E.; Andersen, I.H.; Nielsen, L.P.; Heikkilä, M.; Leskelä, M. The structure and the photocatalytic activity of titania based nanotube and nanofiber coatings. *Appl. Surf. Sci.* **2016**, *368*, 165–172.
  109. Chen, X.; Liu, L.; Liu, Z.; Marcus, M.A.; Wang, W.C.; Oyler, N.A.; Grass, M.E.; Mao, B.; Glans, P.A.; Yu, P.Y.; et al. Properties of disorder-engineered black titanium dioxide nanoparticles through hydrogenation. *Sci. Rep.* **2013**, *3*, 1–7.
  110. Sham, T.K.; Lazarus, M.S. X-ray photoelectron spectroscopy (XPS) studies of clean and hydrated TiO<sub>2</sub> (rutile) surfaces. *Chem. Phys. Lett.* **1979**, *68*, 426–432.
  111. Healy, K.E.; Ducheyne, P. Hydration and preferential molecular adsorption on titanium in vitro. *Biomaterials* **1992**, *13*, 553–561.
  112. Xing, M.; Zhang, J.; Chen, F. New approaches to prepare nitrogen-doped TiO<sub>2</sub> photocatalysts and study on their photocatalytic activities in visible

- light. *Appl. Catal. B Environ.* **2009**, *89*, 563–569.
113. Ohno, T.; Masaki, Y.; Hirayama, S.; Matsumura, M. TiO<sub>2</sub>-photocatalyzed epoxidation of 1-decene by H<sub>2</sub>O<sub>2</sub> under visible light. *J. Catal.* **2001**, *204*, 163–168.
  114. Strunk, J.; Vining, W.C.; Bell, A.T. A study of oxygen vacancy formation and annihilation in submonolayer coverages of TiO<sub>2</sub> dispersed on MCM-48. *J. Phys. Chem. C* **2010**, *114*, 16937–16945.
  115. Yu, X.; Kim, B.; Kim, Y.K. Highly enhanced photoactivity of anatase TiO<sub>2</sub> nanocrystals by controlled hydrogenation-induced surface defects. *ACS Catal.* **2013**, *3*, 2479–2486.
  116. Wang, W.; Lu, C.; Ni, Y.; Su, M.; Xu, Z. A new sight on hydrogenation of F and N-F doped {001} facets dominated anatase TiO<sub>2</sub> for efficient visible light photocatalyst. *Appl. Catal. B Environ.* **2012**, *127*, 28–35.
  117. Chong, S. V.; Kadowaki, K.; Xia, J.; Idriss, H. Interesting magnetic behavior from reduced titanium dioxide nanobelts. *Appl. Phys. Lett.* **2008**, *92*, 1–4.
  118. Livraghi, S.; Maurelli, S.; Paganini, M.C.; Chiesa, M.; Giamello, E. Probing the local environment of Ti<sup>3+</sup> ions in TiO<sub>2</sub> (rutile) by 17O HYSCORE. *Angew. Chemie - Int. Ed.* **2011**, *50*, 8038–8040.
  119. Polliotto, V.; Morra, S.; Livraghi, S.; Valetti, F.; Gilardi, G.; Giamello, E. Electron transfer and H<sub>2</sub> evolution in hybrid systems based on [FeFe]-hydrogenase anchored on modified TiO<sub>2</sub>. *Int. J. Hydrogen Energy* **2016**, *41*, 10547–10556.
  120. Serwicka, E. ESR study on the interaction of water vapour with polycrystalline TiO<sub>2</sub> under illumination. *Colloids and Surfaces* **1985**, *13*, 287–293.
  121. Indrakanti, V.P.; Kubicki, J.D.; Schobert, H.H. Photoinduced activation of CO<sub>2</sub> on Ti-based heterogeneous catalysts: Current state, chemical physics-based insights and outlook. *Energy Environ. Sci.* **2009**, *2*, 745–758.
  122. Xin, X.; Xu, T.; Wang, L.; Wang, C. Ti<sup>3+</sup>-self doped brookite TiO<sub>2</sub> single-crystalline nanosheets with high solar absorption and excellent photocatalytic CO<sub>2</sub> reduction. *Sci. Rep.* **2016**, *6*, 1–8.
  123. Lee, J.; Sorescu, D.C.; Deng, X. Electron-induced dissociation of CO<sub>2</sub> on TiO<sub>2</sub>(110). *J. Am. Chem. Soc.* **2011**, *133*, 10066–10069.
  124. Liu, L.; Zhao, C.; Li, Y. Spontaneous dissociation of CO<sub>2</sub> to CO on defective surface of Cu(I)/TiO<sub>2-x</sub> nanoparticles at room temperature. *J. Phys. Chem. C* **2012**, *116*, 7904–7912.
  125. Ji, Y.; Luo, Y. New Mechanism for Photocatalytic Reduction of CO<sub>2</sub> on the Anatase TiO<sub>2</sub>(101) Surface: The Essential Role of Oxygen Vacancy. *J. Am. Chem. Soc.* **2016**, *138*, 15896–15902.
  126. Tu, W.; Zhou, Y.; Zou, Z. Photocatalytic conversion of CO<sub>2</sub> into renewable hydrocarbon fuels: State-of-the-art accomplishment, challenges, and prospects. *Adv. Mater.* **2014**, *26*, 4607–4626.
  127. Ji, Y.; Luo, Y. Theoretical Study on the Mechanism of Photoreduction of CO<sub>2</sub> to CH<sub>4</sub> on the Anatase TiO<sub>2</sub>(101) Surface. *ACS Catal.* **2016**, *6*, 2018–2025.
  128. Li, Y.; Yang, K.; Chen, J.; Cheng, J.; Jiang, Y.; Zhao, H.; Liu, L. Engineering Coexposed {001} and {101} Facets in Oxygen-Deficient TiO<sub>2</sub> Nanocrystals for Enhanced CO<sub>2</sub> Photoreduction under Visible Light. *ACS Catal.* **2015**, *6*, 1097–1108.
  129. Huygh, S.; Bogaerts, A.; Neyts, E.C. How Oxygen Vacancies Activate CO<sub>2</sub>

- Dissociation on TiO<sub>2</sub> Anatase (001). *J. Phys. Chem. C* **2016**, *120*, 21659–21669.
130. Zhao, H.; Pan, F.; Li, Y. A review on the effects of TiO<sub>2</sub> surface point defects on CO<sub>2</sub> photoreduction with H<sub>2</sub>O. *J. Mater.* **2017**, *3*, 17–32.
  131. Chang, X.; Wang, T.; Gong, J. CO<sub>2</sub> photo-reduction: Insights into CO<sub>2</sub> activation and reaction on surfaces of photocatalysts. *Energy Environ. Sci.* **2016**, *9*, 2177–2196.
  132. Liu, L.; Li, Y. Understanding the reaction mechanism of photocatalytic reduction of CO<sub>2</sub> with H<sub>2</sub>O on TiO<sub>2</sub>-based photocatalysts: A review. *Aerosol Air Qual. Res.* **2014**, *14*, 453–469.
  133. Henderson, M.A. A surface science perspective on TiO<sub>2</sub> photocatalysis. *Surf. Sci. Rep.* **2011**, *66*, 185–297.
  134. Liu, X.; Zhu, G.; Wang, X.; Yuan, X.; Lin, T.; Huang, F. Progress in Black Titania: A New Material for Advanced Photocatalysis. *Adv. Energy Mater.* **2016**, *6*.
  135. Kim, J.Y.; Jung, H.S.; No, J.H.; Kim, J.R.; Hong, K.S. Influence of anatase-rutile phase transformation on dielectric properties of sol-gel derived TiO<sub>2</sub> thin films. *J. Electroceramics* **2006**, *16*, 447–451.
  136. Catlow, C.R.A.; James, R. Disorder in TiO<sub>2-x</sub>. *Proc. R. Soc. A Math. Phys. Eng. Sci.* **2006**, *384*, 157–173.
  137. Cui, H.; Zhao, W.; Yang, C.; Yin, H.; Lin, T.; Shan, Y.; Xie, Y.; Gu, H.; Huang, F. Black TiO<sub>2</sub> nanotube arrays for high-efficiency photoelectrochemical water-splitting. *J. Mater. Chem. A* **2014**, *2*, 8612–8616.

## Appendix A

### Nyquist plots fitting

The Nyquist plots here presented show the measured data (dots) and the fitting (straight lines) obtained for each applied potential, here indicated by the labels (a, b, c and so on). The plots are realized in order to keep the same step on the ReZ as well as on the -ImZ axes.

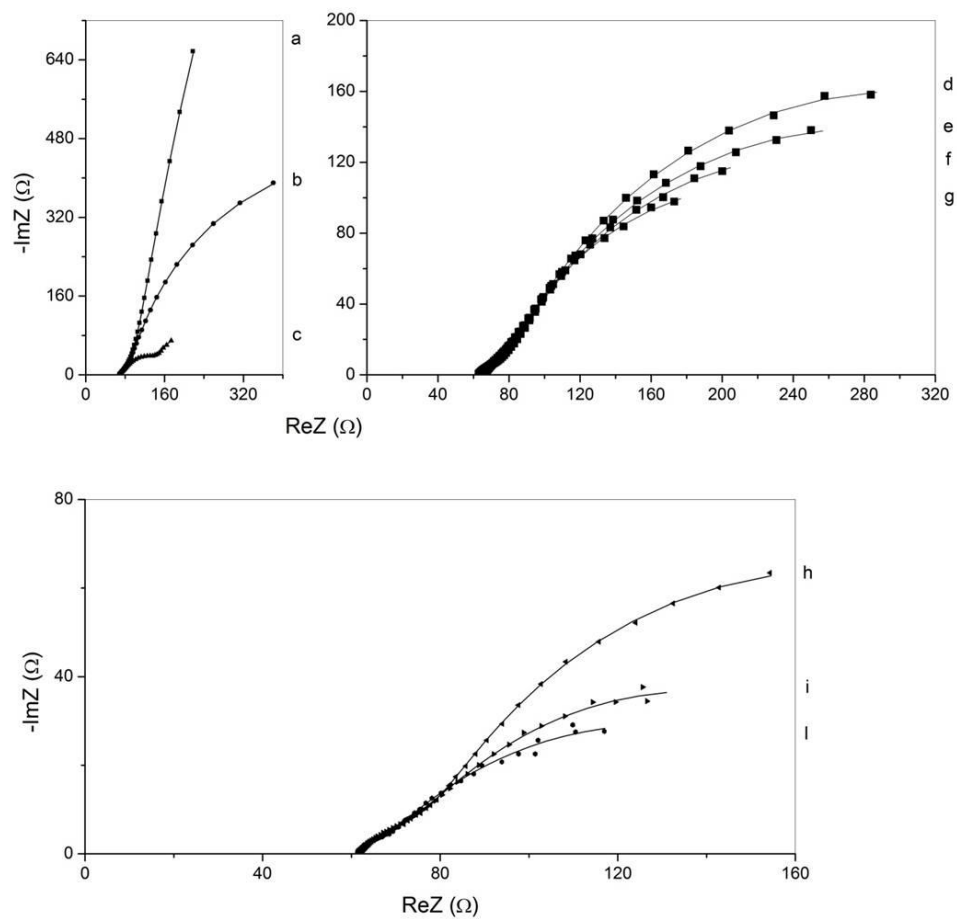
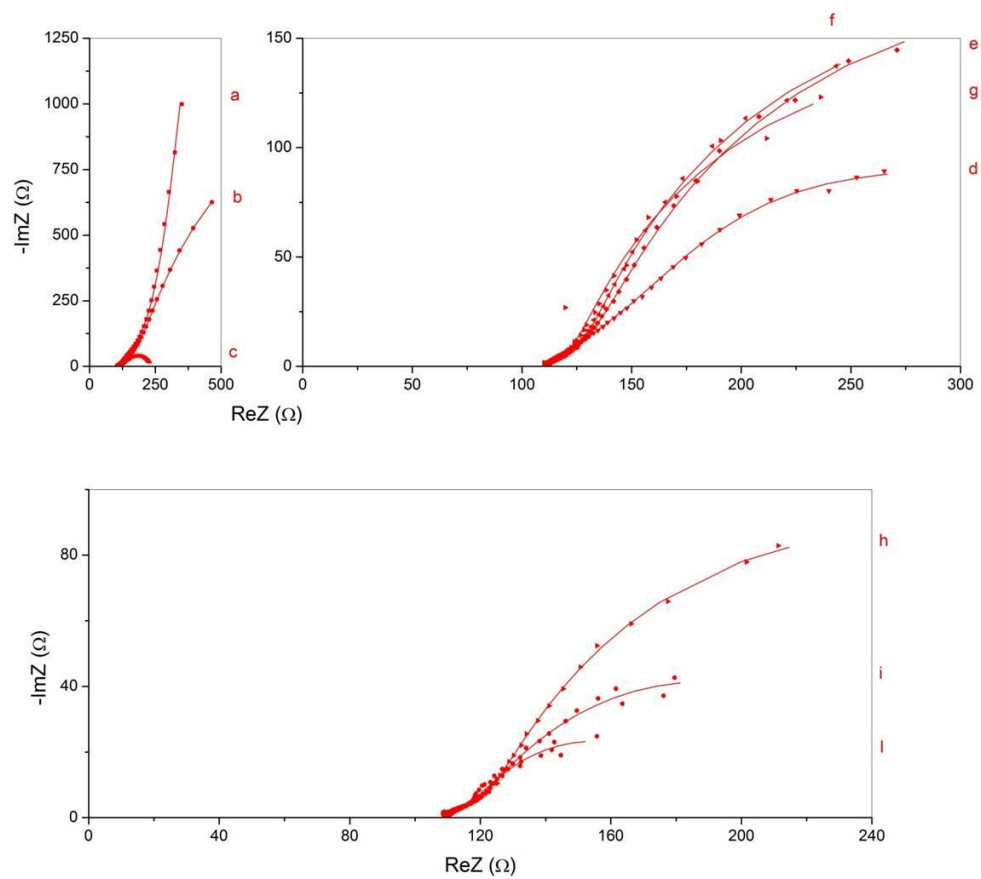


Figure 61. SnO<sub>2</sub> Nyquist plot datas (dots) with fitting (straight line). The labels are linked to the applied potentials (vs RHE): (a) 0.61 V, (b) 0.41 V, (c) 0.21 V, (d) 0.01 V, (e) -0.19 V, (f) -0.39 V, (g) -0.59 V, (h) -0.79 V, (i) -0.99 V and (l) -1.19 V.



**Figure 62.** Fe-SnO<sub>2</sub> Nyquist plot datas (dots) with fitting (straight line). The labels are linked to the applied potentials (vs RHE): (a) 0.61 V, (b) 0.41 V, (c) 0.21 V, (d) 0.01 V, (e) -0.19 V, (f) -0.39 V, (g) -0.59 V, (h) -0.79 V, (i) -0.99 V and (l) -1.19 V.

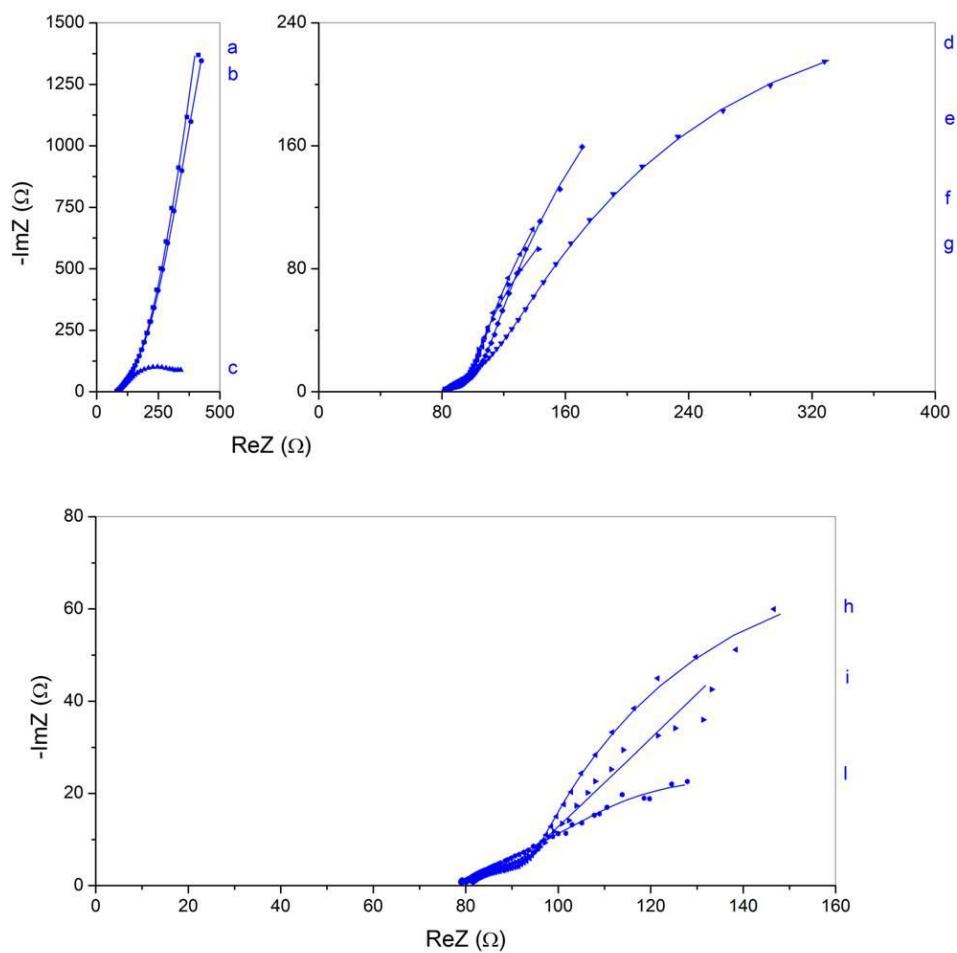
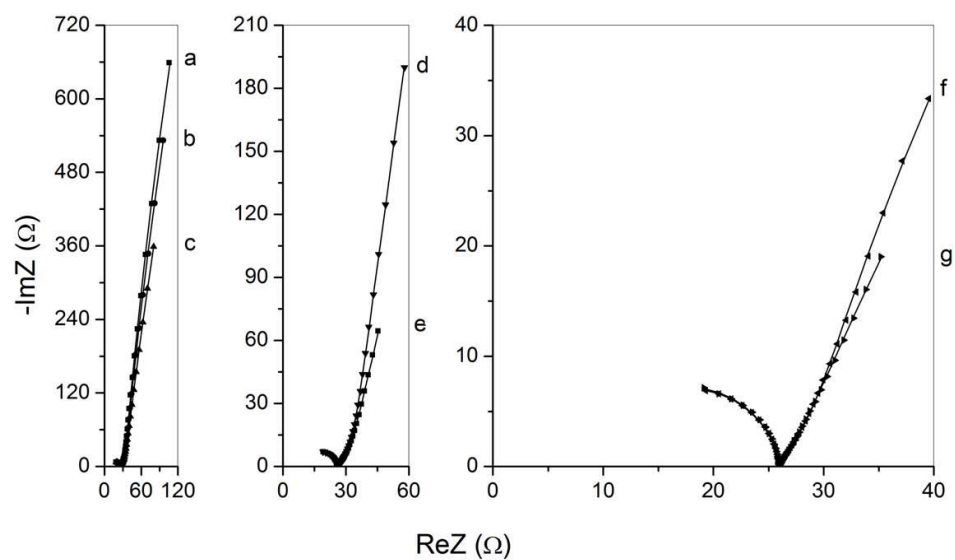
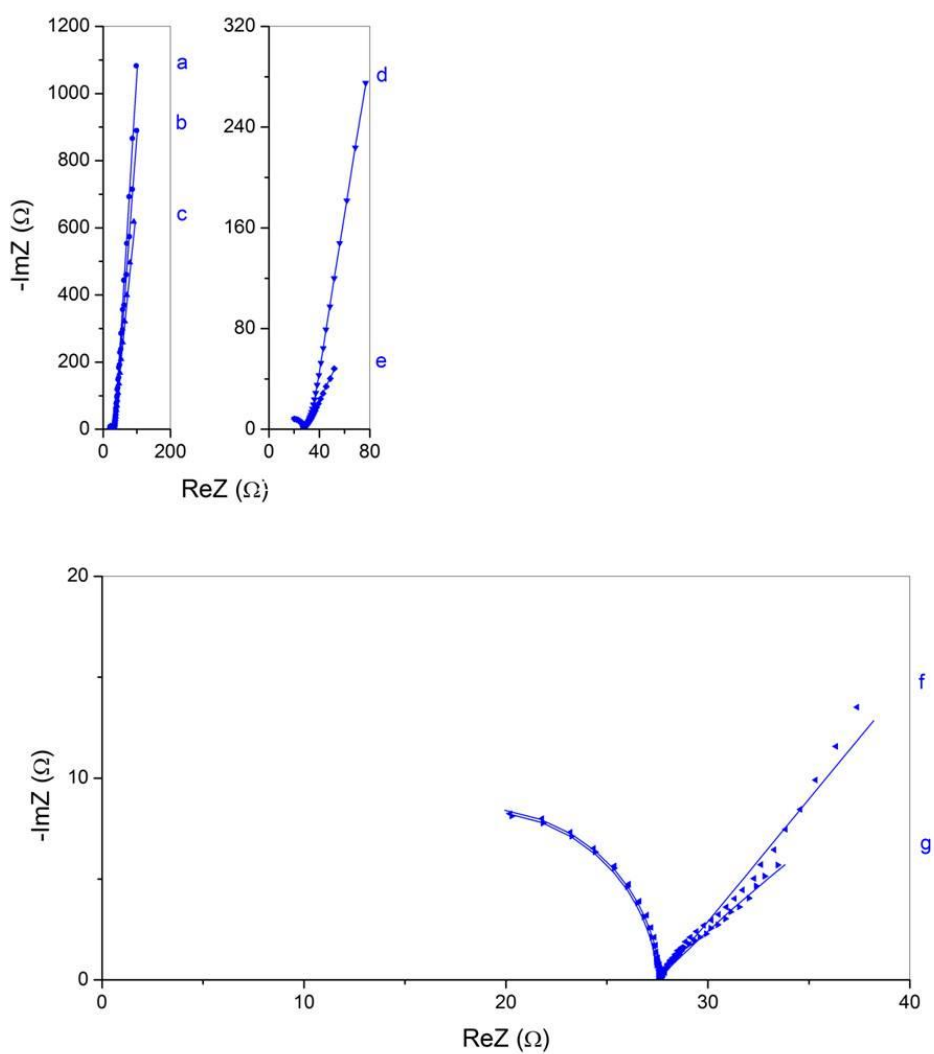


Figure 63. Ti-SnO<sub>2</sub> Nyquist plot data (dots) with fitting (straight line). The labels are linked to the applied potentials (vs RHE): (a) 0.61 V, (b) 0.41 V, (c) 0.21 V, (d) 0.01 V, (e) -0.19 V, (f) -0.39 V, (g) -0.59 V, (h) -0.79 V, (i) -0.99 V and (l) -1.19 V.



**Figure 64.** sd-TiO<sub>2</sub> Nyquist plot datas (dots) with fitting (straight line). The labels are linked to the applied potentials (vs RHE): (a) 0.61 V, (b) 0.41 V, (c) 0.21 V, (d) 0.01 V, (e) -0.19 V, (f) -0.39 V and (g) -0.59 V.



**Figure 65.** Ar-TiO<sub>2</sub> Nyquist plot datas (dots) with fitting (straight line). The labels are linked to the applied potentials (vs RHE): (a) 0.61 V, (b) 0.41 V, (c) 0.21 V, (d) 0.01 V, (e) -0.19 V, (f) -0.39 V and (g) -0.59 V.

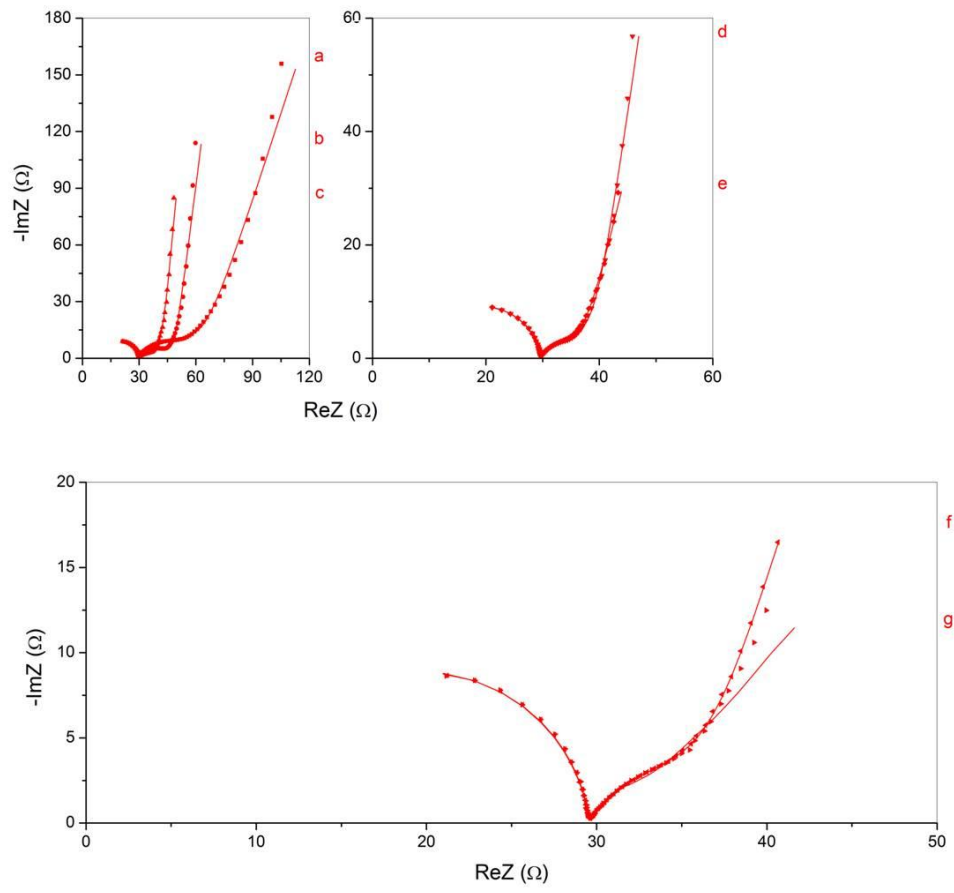


**Figure 66.** a-TiO<sub>2</sub> Nyquist plot datas (dots) with fitting (straight line). The labels are linked to the applied potentials (vs RHE): (a) 0.61 V, (b) 0.41 V, (c) 0.21 V, (d) 0.01 V, (e) -0.19 V, (f) -0.39 V, (g) -0.59 V, (h) -0.79 V, (i) -0.99 V, (l) -1.19 V.